FINITE ELEMENT AND FATIGUE ANALYSIS OF WELDED JOINTS WITH APPLICATION TO DISC FILTER CORE PIPES

by

KERRY LEE PENNER

B.Eng. (Mechanical Engineering), The University of Victoria, 1994

A THESIS SUBMITTED IN PARTIAL FULFILLMENT OF

THE REQUIREMENTS FOR THE DEGREE OF

MASTER OF APPLIED SCIENCE

in

THE FACULTY OF GRADUATE STUDIES

(Department of Mechanical Engineering)

,

We accept this thesis as conforming
to the required standard

THE UNIVERSITY OF BRITISH COLUMBIA

December 1997

In presenting this thesis in partial fulfilment of the requirements for an advanced degree at the University of British Columbia, I agree that the Library shall make it freely available for reference and study. I further agree that permission for extensive copying of this thesis for scholarly purposes may be granted by the head of my department or by his or her representatives. It is understood that copying or publication of this thesis for financial gain shall not be allowed without my written permission.

Department of Mechanical Engineering

The University of British Columbia
Vancouver, Canada

Date December 15, 1997

ABSTRACT

In the pulp and paper industry, rotary vacuum disc filters are commonly used as save-all devices to reclaim fine, reusable fibers from mill white water systems while simultaneously clarifying white water for the purpose of recycle. A complete failure analysis was performed on one of Ingersoll-Rand's type 316L stainless steel disc filters which suffered severe cracking in the outer shell of the center support frame or core pipe. Based on a thorough visual examination of the fracture surfaces, aided by low power and scanning electron microscopy, the cracking problem was found to be caused by corrosion fatigue emanating from lack of penetration root defects in the circumferential weld seams.

The ensuing research program was focused on the development of a numerical procedure (i.e. finite elements) to evaluate the crack propagation rate in a welded joint. A new finite element sub-modeling technique was first developed to facilitate the transfer of boundary conditions from a coarse finite element model to a refined sub-model. The proposed technique resolves a number of frequently encountered boundary condition incompatibilities and provides an alternative approach to finite element sub-modeling or sub-structuring.

Various concepts relevant to the study of fracture and fatigue in welded joints were then considered. A method for predicting the fatigue crack growth rate in a welded joint with residual stress was used in conjunction with the proposed sub-modeling technique to predict the fatigue life for a new core pipe design. The original Ingersoll-Rand design was also

modeled to assess the accuracy of the procedure since the actual equipment service life was known. The fatigue lives were determined in both air and simulated white water (i.e. NaCl) environments. The calculated fatigue life of the original design in air was much longer than the actual equipment service life; therefore, it was concluded that pure mechanical fatigue does not accurately describe the failure mechanism. Moreover, the calculated fatigue life in NaCl is much closer to the actual service life of the equipment. The new design's superiority is also evident since its fatigue life in NaCl is more than eight times that of the original design.

TABLE OF CONTENTS

LIST OF FIGURES

LIST OF TABLES

ACKNOWLEDGEMENT

CHAPTER 1

INTRODUCTION

1.1   Methods of Pulping

Pulping refers to any process which reduces wood (or other fibrous raw material) to a fibrous mass and may be accomplished mechanically, thermally, chemically, or by combinations of these treatments. Existing commercial processes are broadly classified as mechanical, chemical or semichemical [1, 2]. A brief description of each process is now given as an introduction to the common methods of pulp and paper production. A greater emphasis is placed on chemical pulping processes due to their relevance later in the thesis.

1.1.1 Mechanical Pulping

Mechanical pulping processes, which account for approximately 20% of North American pulp production, have the advantage of converting up to 90% of the dry weight of the wood into pulp, but require prodigious amounts of energy to accomplish this objective [1]. The oldest and still a common method of mechanical pulping is the groundwood process, where a block (or bolt) of wood is pressed lengthwise against a wetted, roughened grinding stone revolving at peripheral speeds of 1000-1200 m/min. The fibers are removed from the wood, abraded and washed away from the stone surface with water. The dilute slurry of fiber and fiber fragments is screened to remove slivers and oversized particles and is subsequently thickened (by removal of water) to form a pulp stock suitable for papermaking. More recently, the utilization of refiners involves shredding and defibering the chips of wood

1

between rotating discs; the product is known as refiner mechanical pulping (RMP). RMP typically retains more long fibers than stone ground wood and therefore yields stronger paper.

The conventional RMP process has undergone extensive development during the past two decades. Most new installations now employ thermal and/or chemical presoftening of the wood chips to reduce the energy requirement and improve the resultant fiber properties. For example, when the chips are given a pressurized steam pretreatment, the resultant product, called thermomechanical pulp (TMP), is significantly stronger than RMP and contains very little screen reject material [1].

1.1.2 Chemical Pulping

In chemical pulping, the wood chips are cooked with appropriate chemicals in an aqueous solution at elevated temperatures and pressures. The intention is to degrade and dissolve away the lignin and leave behind most of the cellulose and hemicelluloses in the form of intact fibers. In practice, chemical pulping methods are successful in removing most of the lignin; however, they also degrade and dissolve a certain amount of fibrous material so that the yield of pulp is low (usually between 40% and 50% of the original wood substance) relative to mechanical pulping methods. In terms of current annual pulp production, chemical pulping accounts for approximately 70% of North American production, of which 90% is produced by the dominant (alkaline) kraft process and the remaining 10% is produced by the (acidic) sulfite process [1]. A brief description of the kraft and sulfite pulping processes is now given, primarily in terms of their respective chemistries. This background information will be beneficial when corrosion-related problems in chemical pulping operations are discussed in the subsequent section.

The Kraft Process

In the kraft process, paper is produced by digesting wood chips in white liquor, which contains a mixture of sodium sulfide (Na_2S) and sodium hydroxide (NaOH) as the active pulping constituents and carbonate, sulfate, chlorides and other sulfoxy compounds as minor constituents [1-3]. Lignin is dissolved from wood chips exposed to white liquor at temperatures on the order of 350°F. The product is transferred to brown stock washers to remove the weak black liquor from the brown pulp. After screening, the pulp may go directly to the paper mill to produce unbleached paper, or it may be directed first to the bleach plant to produce white paper. The digestor vapors are condensed, and the condensate is pumped to the brown stock washers. The black liquor from these washers is concentrated and burned with sodium sulfate (Na_2SO_4) to recover Na_2CO_3 and Na_2S. After dissolution in water, this green liquor is treated with calcium hydroxide ($Ca(OH)_2$) to produce NaOH to replenish the white liquor. Pulp bleaching involves treating with various chemicals, including chlorine, chlorine dioxide (ClO_2), NaClO, $Ca(ClO)_2$, peroxide, caustic soda, quicklime, or oxygen.

The Sulfite Process

The sulfite process uses a liquor in the digestor that is different from that used in the kraft process. A mixture of sulfurous acid (H_2SO_3) and bisulfite ion (HSO_3^-) is used to attack and solubilize the lignin [1-3]. The sulfites combine with the lignin to form salts of lignosulfonic acid which are soluble in the cooking liquor, and the chemical structure of the lignin is left largely intact. The chemical base for the bisulfite can be ionic calcium, magnesium, sodium or ammonium. Sulfite pulping may be carried out over a wide range of pH. *Acid sulfite* denotes pulping with an excess of free sulfurous acid (pH 1-2) while *bisulfite* cooks are

carried out under less acidic conditions (pH 3-5) [1]. The pulp is then washed and separated from the spent sulfite liquor (known as red liquor). Difficulties in reclaiming pulping chemicals from red liquor present economic and environmental obstacles to the use of the sulfite pulping process although several sulfite mills remain in operation [2].

1.1.3 Semichemical Pulping

Semichemical pulping accounts for only about 6% of production and combines chemical and mechanical methods of pulping [1]. Chemi-mechanical pulps (CMP) and chemi-thermomechanical pulps (CTMP) are cleaner, brighter and have improved strength properties compared to other mechanical pulps. Essentially, the wood chips are partially softened or digested with chemicals and subsequently abraded mechanically, most often in disc refiners. Accordingly, semichemical methods encompass the intermediate range of pulp yields between mechanical and chemical pulping (i.e. 55% to 85% of the dry wood). Included under the classification of semichemical pulping are the high-yield kraft and high-yield sulfite processes. In both instances, cooking is limited to partial delignification and the actual defibering is accomplished mechanically.

1.2 Corrosion in Chemical Pulp and Paper Mills

Chemical pulp mills tend to be associated with objectionable odors which originate from the sulfur employed in the pulping operation. However, emissions from modern mills are usually less than 10% the level of typical operations 25 years ago [1]. Unfortunately, some of the organic sulfide gases are still offensive at concentrations as low as 1 ppb (part per billion). Obviously, it would be highly desirable to eliminate sulfur as a pulping chemical,

and a number of non-sulfur processes are currently under development. However, some form of kraft pulping will certainly remain the dominant (chemical) pulping process for both softwood and hardwood raw materials, at least in the foreseeable future.

Few industrial plants can match the diversity of severely corrosive environments found in the typical pulp and paper mill [2]. Equipment used in the production of pulp and paper products is routinely exposed to corrosive conditions ranging from hot alkaline sulfide cooking liquors to acidic, highly oxidizing bleach solutions. As one might expect, chemical pulp and paper mills are routinely challenged by virtually every known type of corrosion-related damage. As a result, the investigation of corrosion-related failures of mechanical equipment continues to be of significant importance to the pulp and paper industry. Although pulp is produced by many different processes (as previously outlined), the most severe corrosion problems arise in chemical pulping where fibers are released from wood chips and other fibrous raw materials by chemical digestion at high temperatures and pressures.

The objective of the following discussion is to summarize some of the primary concerns regarding corrosion-related failures of pulp and paper mill equipment. This begins with a discussion of current trends in the pulp and paper industry which are leading to increasingly aggressive environments, followed by a brief section on equipment material selection. The focus then shifts to a particular piece of rotating equipment (i.e. the rotary vacuum disc filter) used to recover fibers from spent chemicals and which has experienced a shortened service life due to extensive weld failures. A complete review of corrosion control in the pulp and paper industry is beyond the scope of this thesis. Additional corrosion-related information pertaining to various equipment used in pulp and paper mill environments is available in a technical paper by R.A. Yeske [2] and in the ASM Specialty Handbook: *Stainless Steels* [3].

1.2.1 White Water Systems

White water is the drainage from wet stock, regardless of color, in pulping, papermaking and bleaching operations. During the past 20 years, white waters have become increasingly more corrosive due to ongoing programs to close-up white-water systems due to increased recycle for environmental and energy reasons [2-4]. Closure is accomplished by increasing water reuse and countercurrent washing. This objective may be partly achieved by utilizing equipment that requires less fresh water and partly by reusing filtered white water.

Decreased fresh water usage and increased recycle of white water has raised temperatures of washing stage filtrates, increased suspended and dissolved solids, and increased the propensity for biological growth. The white waters in coastal mills also contain dissolved chlorides (from sea-borne logs and chlorine bleaching), sulfates (from kraft pulping and CTMP), and thiosulfate (from sodium hydrosulfite brightening) [4]. All of these factors have intensified the corrosivity of white waters which, in turn, have exacerbated corrosion-related damage in chemical pulp and paper mill equipment.

1.2.2 Material Selection in the Pulp and Paper Industry

Pulps are subjected to a wide range of processing steps, depending on their method of preparation (i.e. mechanical, chemical, semichemical, etc.) and their end use. Screening, thickening and storage operations are necessary for virtually all pulp grades while cleaning is usually required where appearance is important. Defibering is required for all semichemical and high-yield chemical grades. Deknotting is usually necessary in the production of clean bleachable chemical pulps. Blending operations are almost always desirable for achieving product uniformity but are often omitted from the pulp processing scheme because of cost

considerations. Pulp drying is required when pulp is stored for long periods (to prevent fungal or bacteriological activity) or shipped over long distances (to reduce freight costs) [1]. Pulp and paper mills therefore require the utilization of extensive ancillary equipment for stock preparation and paper machine operation.

Various alloys may be selected for the wide range of corrosion conditions encountered in chemical pulp and paper mills. Resistance to localized corrosion (pitting or crevice corrosion attack by aggressive anions such as chlorides and thiosulfate) is essential for the wetted components used in chemical pulping and paper-making equipment. Traditionally, austenitic stainless steels have been used because of their combination of satisfactory corrosion resistance and excellent weldability [3]. For many years, the standard materials of construction have been type 304L stainless steel for inland mills and type 316L stainless steel for coastal mills where sea transport of logs introduces chlorides that ultimately end up in mill white water systems [4]. Paper mill headboxes are usually fabricated from type 316L plate with superior surface finish and are sometimes electropolished to prevent scaling which may affect pulp flow. Type 317L stainless steel has been the typical bleach plant alloy for oxidizing acid chloride environments; however, type 317L may no longer be adequate for long-term service due to the increasingly aggressive nature of today's white water systems.

Some austenitic stainless steels may also be sensitized to intergranular corrosion by welding or by long-term thermal exposure which leads to the precipitation of chromium carbides in the grain boundaries and to the depletion of chromium in adjacent areas. Sensitization may be greatly delayed or even completely prevented by the use of lower-carbon grades (< 0.03% C), such as 304L and 316L, or stabilized grades, such as types 321 and 347 [3].

Many mills have recently turned to higher alloy stainless steels, nickel-based alloys, and titanium for better corrosion resistance. The 904L-type alloys with about 4.5% Mo provide somewhat better pitting resistance than types 316L and 317L, and the 6% Mo steels, such as 254SMO, are remarkably resistant. Duplex stainless steels, such as 2205 and Ferralium 255, are chromium-nickel-molybdenum alloys that are balanced to contain a mixture of austenite and ferrite. Their duplex structure results in improved stress-corrosion cracking resistance, compared with austenitic stainless steels, and improved toughness and ductility, compared with ferritic stainless steels. Unfortunately, the more corrosion-resistant alloys are more expensive, and the challenge is selecting an alloy with just enough resistance to avoid corrosion problems [3].

1.3   Rotary Vacuum Disc Filters

1.3.1 Pulp Stock Thickening

Following low-consistency operations such as cleaning and screening, it is necessary to thicken the stock (with or without washing) prior to the next process operation. A variety of equipment is available for this purpose depending on requirements. In many instances, a simple increase in stock consistency to the 4 - 8% range is required. For this service, a gravity thickener (usually called a decker) is commonly used, and for intermediate levels of thickening (10 - 12%), the so-called valveless washer may be used. To achieve consistencies of 12 - 16% and also wash the stock, it is necessary to use a vacuum washer. All equipment of this type functions by applying vacuum over the forming and washing zones, then cutting off the vacuum by means of an internal valving arrangement to allow the thickened sheet to

be released. The pulp mat is discharged from the washer mould by takeoff rolls or doctors. The mesh face is often shower-cleaned prior to re-submergence in the vat [1].

For simple thickening of very dilute stocks up to 12% consistency, multidisc thickeners (also commonly referred to as rotary vacuum disc filters) of the type illustrated in *Figure 1.1* may be employed. These high capacity rotary vacuum disc filters are machines having high filtration area resulting from the discs rotating in the vertical plane. These units are designed for applications where large flows or difficult to dewater slurries require slow filter rotating speeds [5]. Multidisc thickeners are most commonly used as save-all devices, namely, to reclaim fine, reusable fibers and fillers from white water systems while simultaneously clarifying white water for the purpose of recycle [1].
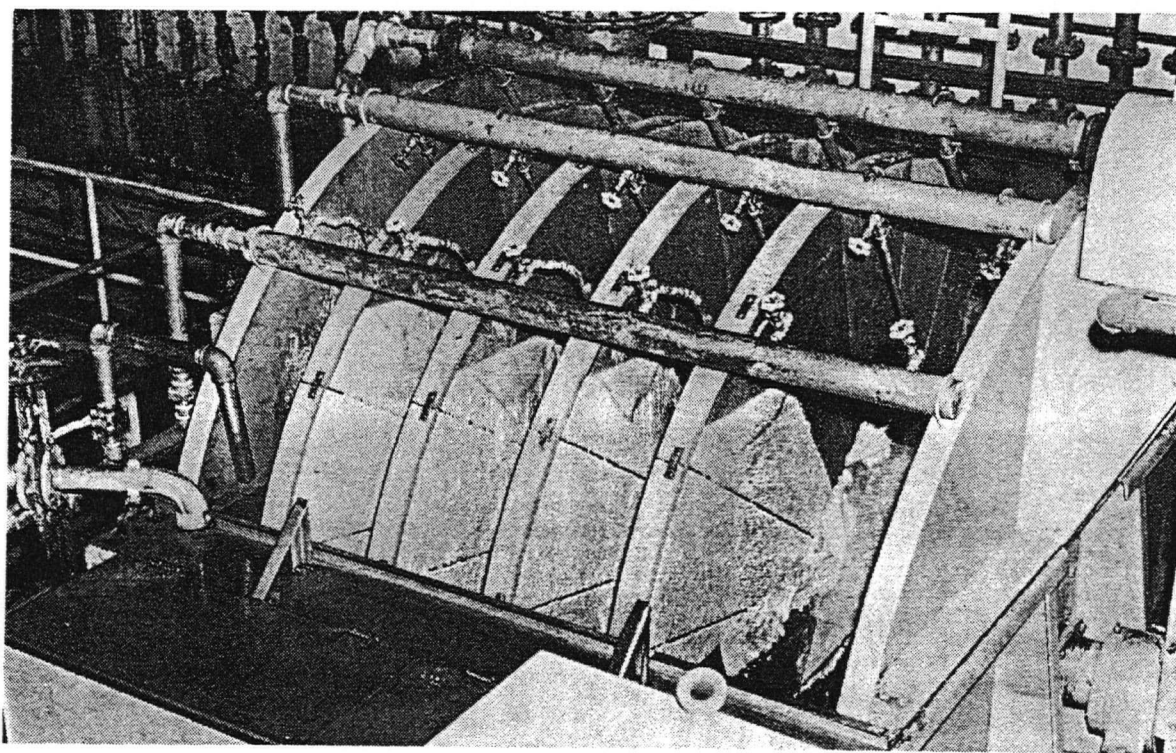
Figure 1.1 **Rotary Vacuum Disc Filter (Multidisc Thickener) [1]**

1.3.2 Save-all Operation

The disc filter consists of a series of discs mounted on a center shaft. White water flows

through the filtering medium into each sector and then through the core of the rotating shaft.

A representative rotary vacuum disc filter system is shown in *Figure 1.2*. The operating

sequence of a typical disc filter save-all is shown in *Figure 1.3*.

LEGEND

a White water
b High-consistency stock
c Clear filtrate
d Cloudy filtrate
e Sweetener stock

1 Inlet box
2 Filter vat
3 Filter discs
4 Suction and control head
5 Droplegs
6 Cloudy filtrate tank
7 Clear filtrate tank
8 Stock Dilution
9 Cake removal shower
10 Cleaning shower
11 Pulping screw
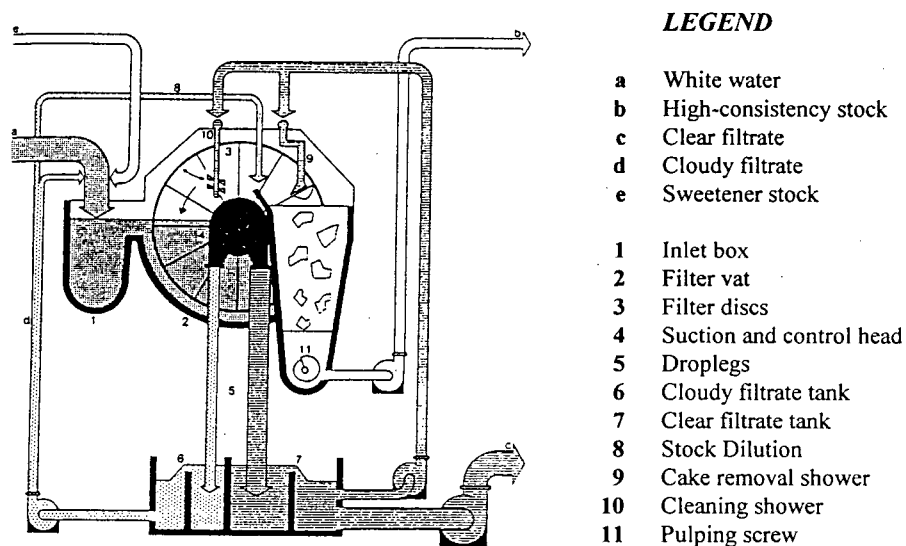
Figure 1.2 **Rotary Vacuum Disc Filter System [1]**
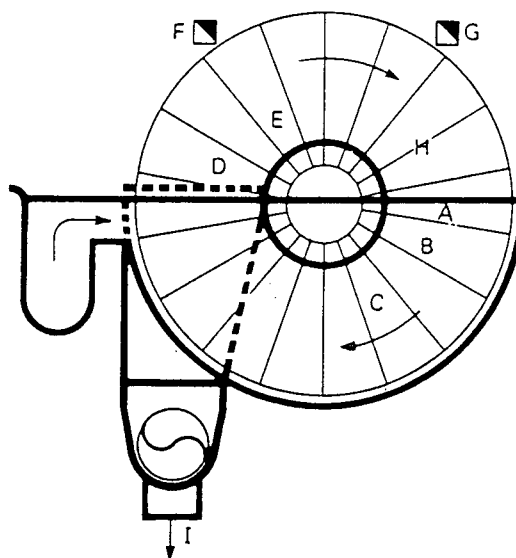
Figure 1.3 **Disc Filter Operating Sequence [1, 5]**

Pulp is fed into the vat from the inlet box. A fiber mat forms on the faces of each sector as it submerges in the vat of stock (**A**). After complete submergence of the sector, vacuum is applied and more pulp is deposited while filtrate is drawn through the mat (**B**). The filtrate obtained during the initial portion of the cycle contains fibers which pass through the filter during initial formation of the mat. The initial (cloudy) filtrate may be segregated (by action of the end valve) then recycled for reclarification or used for dilution purposes elsewhere. More fibers are deposited, resulting in increased filtrate clarity as the fiber mat thickens (**C**). This latter, progressively cleaner (clear) filtrate is sufficiently free of fiber to be used for shower water. The vacuum is cut off immediately upon emergence of the sector (**D**). The fiber mat is further dewatered by residual vacuum until the sector reaches a position, at which the atmospheric port opens (**E**), and the knock-off shower cuts the top of the mat loose from the filtration media (**F**). The mat then peels off and falls into the chute located between consecutive discs. Sluicing showers keep the chutes clean and may also be used to dilute the mat so that the recovered stock is nearer to process consistency. Complete and uniform cleaning of the filtration area is achieved by face cleaning showers (**G**). The atmospheric port then closes (**H**), and the thickened pulp is discharged (**I**). Consistency of the stock prior to discharge from the disc face is usually in the 16 - 20% range. After subsequent contact with the knock-off showers and sluicing showers, the final stock consistency to the repulper is reduced to the range of 6 - 8% [5].

1.4   Problem Statement and Objectives

The industrial function and operation of rotary vacuum disc filters were described in the preceding two sections. Ingersoll-Rand's Impco Division of Nashua, New Hampshire,

manufactures rotary vacuum disc filters for thickening or save-all applications. As a pulp and paper mill save-all, the disc filter recovers fiber and clarifies white water for reuse. As a thickener, the disc filter provides maximum filtration area in a minimum space. For maximum clarity of any filtrate, the large filter areas allow slower rotating speeds (1 - 2 rpm) and efficient separation of clear and cloudy filtrates [6].

Impco rotary vacuum disc filters may be equipped with 4 to 24 filtration discs. If desired, a large filter may be operated with less than the full number of discs; disc stations not used are sealed in this case. Each filtration disc is comprised of 18 sectors or leaves which are covered on both sides with fine mesh screen. The discs are 12′ in diameter and assembled to a cylindrical core that revolves in a vat containing the pulp slurry. Each disc is fastened to the core pipe with captive screws and aligned with a tongue-and-groove type joint at the periphery. The vacuum valve housing and worm drive assembly are also mounted on the end of the core pipe. White water flows through the filtering medium into each sector as it immerses into the pulp slurry. Each line of sectors along the core pipe empties into a tapered channel through which the filtrate is conducted to the vacuum valve [6].

One of Ingersoll-Rand's type 316L stainless steel disc filters suffered severe cracking of the center support frame (i.e. the core pipe). The core pipe which experienced the failure is approximately 30′ long and 36″ in diameter, as illustrated in the photos in *Figure 1.4*. The cracking developed in the circumferential weld seams in the outer shell of the core pipe. At numerous locations, the cracking was extensive, propagating through the division bars and into the inner shell as well. This typically occurred at locations were the circumferential weld seam coincides with a butt joint in a division bar between adjacent core pipe channels, as shown in *Figure 1.5*.
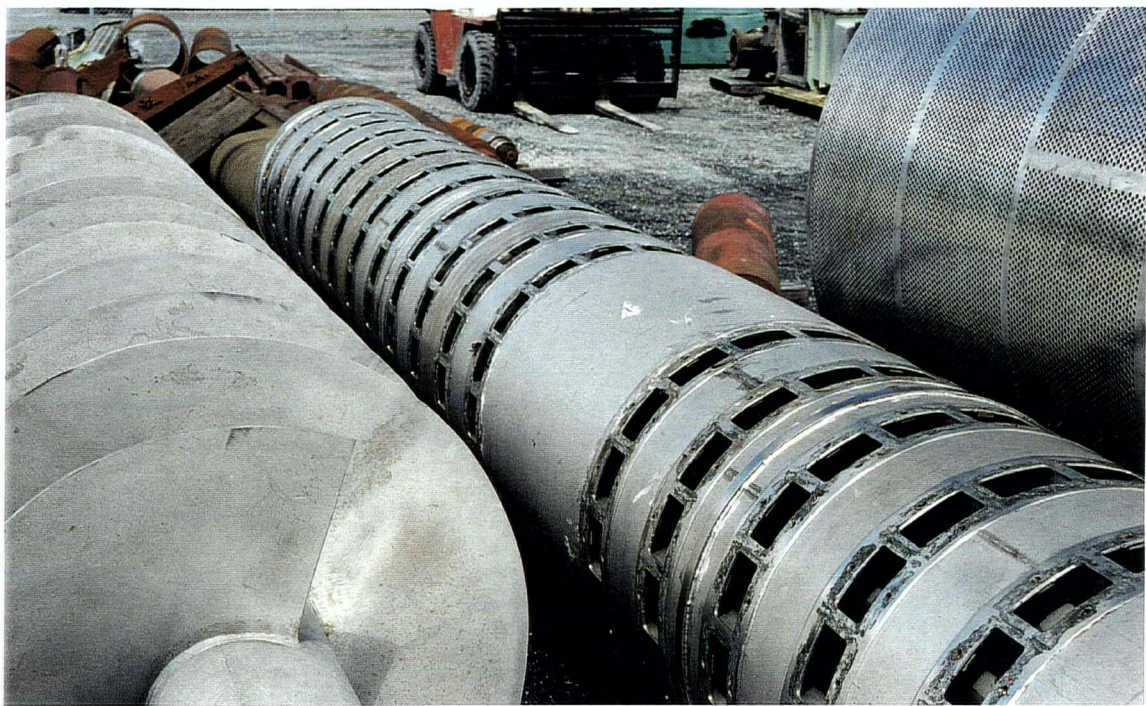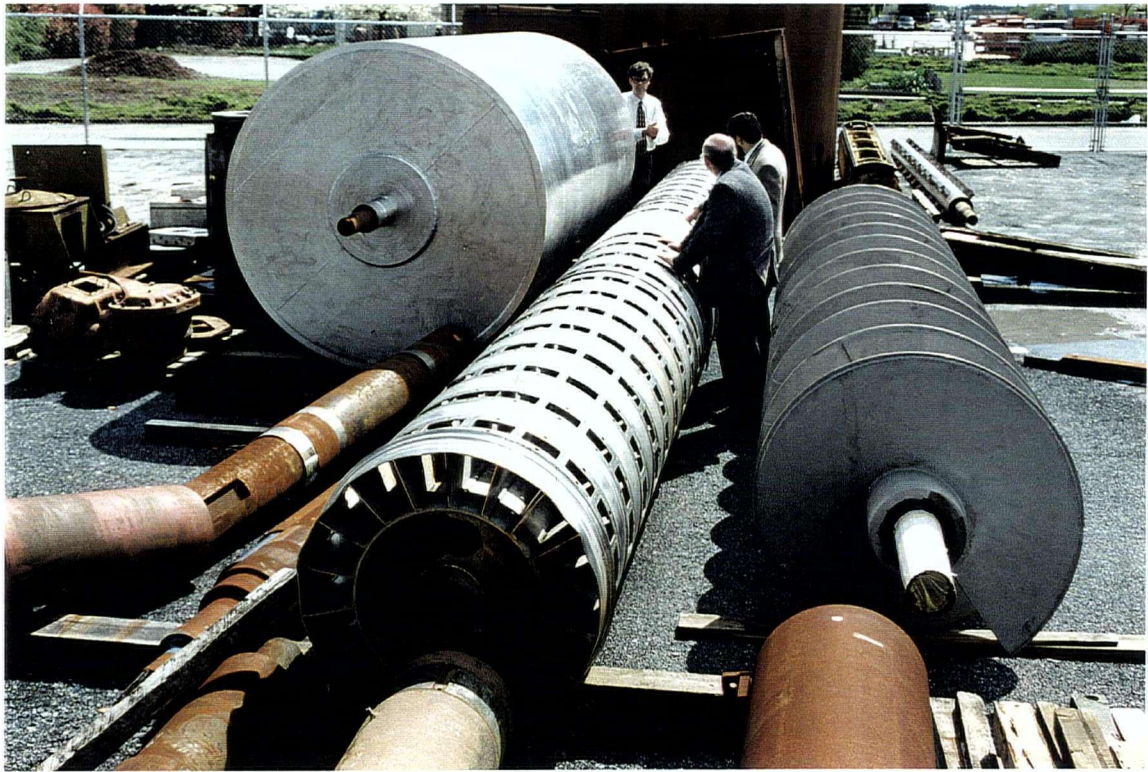
Figure 1.4 **Ingersoll-Rand's Rotary Vacuum Disc Filter Core Pipe**

Figure 1.5 **Severe Cracking through the Core Pipe Division Bar**

The remaining chapters of this thesis are devoted to various aspects associated with the failure of welded joints and, in particular, with Ingersoll-Rand's disc filter core pipe cracking problem. In Chapter 2, the subjects of environmentally induced cracking and problematic weld discontinuities are discussed. The main characteristics of stress corrosion cracking, corrosion fatigue cracking and hydrogen induced cracking are first outlined followed by a brief comparison of each mechanism. A basic overview of welding flaws or defects such as incomplete fusion, incomplete joint penetration (i.e. lack of penetration), cracks, undercut and porosity is then given. A thorough analysis (including visual and metallographic examination, photo microscopy and scanning electron microscopy) is also performed on the core pipe circumferential weld failures.

The application of finite element analysis (FEA) to the static design of mechanical equipment is the focus of Chapter 3. The discussion is mainly concerned with boundary condition incompatibilities which occur as a result of different modeling strategies. For example, the overall structure of a large component or piece of equipment may be comprised of shell elements with six degrees of freedom per node, whereas a small sub-region may be modeled with increased accuracy by employing solid (brick) elements which have only three degrees of freedom per node. The main difficulty arises when attempting to determine the appropriate boundary conditions for the sub-model. A novel finite element sub-modeling technique is presented which facilitates the transfer of boundary conditions from a shell element model to a solid element sub-model. Numerical examples are then presented to demonstrate the procedure and to provide an indication of the accuracy of this method.

In Chapter 4, topics pertaining to the fatigue of welded joints are reviewed. A thorough understanding of concepts such as welding induced residual stress, linear elastic fracture mechanics (LEFM) and fatigue crack propagation is necessary when evaluating the remaining service life of cracked components. This chapter concludes with a description of a recently published method for predicting fatigue crack growth rates in fields of residual stress.

In the final chapter of this thesis, a numerical study is performed which compares the original Ingersoll-Rand design of the core pipe to a new design recently developed through a cooperative project undertaken by Tristar Industries Ltd. and UBC's Finite Element Analysis and Research Lab. The objective of this research is to accurately determine the fatigue crack growth rate emanating from a weld root defect and thereafter predict the service life of the original and new core pipe designs. This study incorporates failure analysis, finite element sub-modeling and fatigue of welded joints as presented in Chapters 2, 3 and 4, respectively.

CHAPTER 2

FAILURE ANALYSIS OF WELDED JOINTS

2.1 Preliminaries

Analysis of failures in dynamically loaded stainless steel equipment as mechanical fatigue, corrosion fatigue, stress corrosion cracking, hydrogen induced cracking or a combination of two or more of these mechanisms may be necessary to determine the appropriate remedial measures to be taken to avoid reoccurring equipment failure. For example, if a failure is due purely to mechanical fatigue, then the solution may not involve a change of metallurgy. Re-evaluation of design stresses, residual stresses, and fabrication details may be sufficient to prolong the service life of the equipment.

When environmental interactions occur, however, the situation becomes significantly more complicated because environmentally induced cracking may involve more than one of the above cracking mechanisms. For example, a stress corrosion crack may initiate at pitting or crevice corrosion and grow to a size sufficient to propagate (perhaps more rapidly) by corrosion fatigue or even mechanical fatigue. If the root cause of the failure is not correctly identified, inappropriate measures may be taken in an attempt to resolve the problem. In such cases, reduction of nominal stress levels by increasing the section size or weld size might not prevent the failure from reoccurring. Particularly for welded equipment, where residual stresses are usually near the yield point, an upgrade in metallurgy or protection from the environment may be required. Conversely, it is not inconceivable that stress corrosion cracking might occur as secondary cracking associated with primary cracking caused by

mechanical fatigue or corrosion fatigue. The dilemma in such a case would be to decide if an upgrade in metallurgy alone might solve the problem.

When environmentally induced cracking may have played a role in a failure, it is therefore important to conduct a complete failure analysis. A reasonably complete failure analysis may include consideration of the following [7]:

- Nominal stress state (design considerations);
- Dynamic loading (frequency, vibration, load spectrum);
- Residual stress (from welding, forming, heat treating, etc.);
- Fabrication details (rough grinding, machining marks, poor weld profiles);
- Nominal and localized environments (temperature, pH, presence of deposits);
- Visual appearance of the fracture surface and associated process side surfaces;
- Scanning electron microscope (SEM) appearance of the fracture surface;
- Metallographic examination of secondary cracks and general microstructure.

Applications involving dynamic loading may be particularly complicated because the loading spectrum in service may not be the same as that assumed for the original design. Residual stresses from fabrication and cyclic stresses arising from vibration or service conditions may have been omitted from the original design considerations and post failure deliberations. Yet cyclic stresses imposed on a high bulk stress (whether residual or operating) may determine the mode of failure and influence the crack growth rates.

Before proceeding with a failure analysis of the disc filter core pipe, it will be beneficial to begin with a definition of the various failure mechanisms that may be classified as environmentally induced cracking. A brief description of each failure mechanism is then given; however, an exhaustive discussion of their characteristics and methods of prevention is beyond the scope of this chapter. In the next section, various welding defects are described with particular attention given to crack-like discontinuities that may occur at the root of the

weld. The circumferential weld failure in the outer shell of the disc filter core pipe is then analyzed in terms of the information presented in the preceding two sections.

2.2 Environmentally Induced Cracking

Environmentally Induced Cracking (EIC) is a general term for brittle mechanical failures that result from a synergism between tensile stress and a corrosive environment. EIC includes Stress Corrosion Cracking (SCC), Corrosion Fatigue Cracking (CFC), and Hydrogen Embrittlement or Hydrogen Induced Cracking (HIC) [8]. As already mentioned, more than one of the three mechanisms may be operative in any given situation, further complicating the analysis of failures and the determination of appropriate prevention methods. It is difficult to make unqualified statements regarding the characteristics of any of the forms of EIC because exceptions are not unusual. Nevertheless, some of the common characteristics of each mechanism are now presented for purposes of comparison.

2.2.1 Stress Corrosion Cracking

Stress corrosion cracking (SCC) is the brittle failure at relatively low constant tensile stress of an alloy exposed to a corrosive environment. Three conditions must be present simultaneously to produce SCC: a critical environment, a susceptible alloy, and some component of tensile stress. Tensile stresses even below yield are sufficient to cause SCC and may result from bolting or fastening parts that fit together imperfectly. Uneven thermal expansion and contraction may produce residual tensile stresses after welding and other heat treatments. SCC is also normally associated with 'static' tensile stresses.

SCC may be either transgranular or intergranular, but the crack follows a general macroscopic path that is always normal to the tensile component of stress. Stress corrosion cracks follow the grain boundaries in the intergranular mode whereas, in transgranular failures, the cracks propagate across the grains usually in specific crystallographic planes. Intergranular failures are typically more common than transgranular ones. Facing halves of recently failed specimens often exactly match one another, regardless of the failure mode, indicating that cracking is primarily by mechanical fracture, with little electrochemical dissolution or corrosion during the fracture process [8].

2.2.2 Corrosion Fatigue Cracking

Corrosion fatigue cracking (CFC) is the brittle failure of an alloy caused by the combined action of fluctuating stresses and a corrosive environment. Stainless steels are used in a wide range of severely aggressive environments because of their low corrosion rate, and the selection of stainless steels in such circumstances is often based on their ability to withstand different types of localized corrosion (i.e. pitting corrosion, crevice corrosion, etc.). However, localized corrosion resistance does not necessarily imply resistance to corrosion under fatigue loading.

Fracture surfaces from CFC, as well as from mechanical fatigue in air, sometimes show macroscopic beach marks where corrosion products have accumulated at discontinuous crack-advance fronts. On the microscopic scale, striations are often evident where each cycle produces a discontinuous advance of the crack front. The frequency of cyclic stress is an important factor. Lower frequencies lead to greater crack propagation per cycle whereas very high frequencies all but eliminate the effects of the corrosive environment. Increasing the

ratio of the minimum to the maximum stress in the cycle generally decreases the resistance to corrosion fatigue. Stress raisers such as notches or surface roughness increase the susceptibility to corrosion fatigue although severe notches have a greater effect on the fatigue life than does corrosion alone. Cracks have often been observed to initiate from corrosion pits which again serve as surface stress concentrations. In any alloy system, corrosion reduces the stress amplitude and shortens the time or number of stress cycles to failure [8].

2.2.3 Hydrogen Induced Cracking

Hydrogen induced cracking (HIC) is brittle mechanical failure caused by penetration and diffusion of atomic hydrogen into the crystal structure of an alloy. Hydrogen may be present from the reduction of water or acid by the following reactions:

$$H_2O + e^- \rightarrow H + OH^- \tag{2.1}$$

$$H^+ + e^- \rightarrow H \tag{2.2}$$
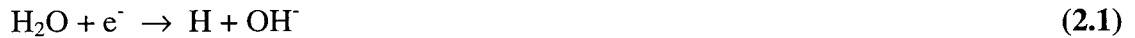
in neutral and acidic solutions, respectively. Before the H_2 molecule can be formed, there is a significant residence time of the nascent H atom on the surface. Because of its small size, atomic hydrogen may then enter the lattice to produce HIC. Aqueous hydrogen sulfide, H_2S, also commonly referred to as sour gas, dramatically accelerates hydrogen entry and subsequent damage in most alloys. The S^{2-} anion slows (poisons) the recombination reaction:

$$H + H \rightarrow H_2 \tag{2.3}$$

and provides a greater activity of nascent atomic H on the surface. The result is sometimes called sulfide stress corrosion cracking although it is really a form of HIC.

HIC is most prevalent in iron alloys because of the restricted slip capabilities in the predominantly body-centered cubic (BCC) crystal structure, and HIC is generally limited to

steels having a hardness of 22 or greater on the Rockwell C scale. The face-centered cubic (FCC) stainless steels and FCC alloys of copper, aluminum, and nickel are more resistant because of their inherent high ductility and lower diffusivity for hydrogen. The BCC and FCC stainless steels are also more resistant because of their relatively low strength, but they too may be made susceptible if the material is highly cold worked [8].

2.2.4 Comparison of Environmentally Induced Cracking Mechanisms

Corrosion fatigue cracking (CFC) is similar to stress corrosion cracking (SCC) and hydrogen induced cracking (HIC) inasmuch as a corrosive solution induces brittle fracture in an alloy that is normally ductile in a noncorrosive environment. SCC and HIC are also similar in that brittle fractures occur in a corrosive environment under constant tensile stress. For CFC, the stress is cyclic rather than constant but must have at least some tensile component, as in SCC and HIC. Brittle fractures occur by cleavage of the metal and, as mentioned earlier, propagate perpendicular to the direction of the principle tensile stress. Beyond these similarities, however, the differences between the mechanisms are striking.

In contrast to SCC, corrosion fatigue cracks usually form more slowly and corrosion products are more likely to be present in the crack. Corrosion products will usually be absent in stress corrosion and hydrogen induced cracks as long as the component has not been exposed for some time after the cracks were formed. CFC cracks are often relatively blunt at the crack tip, in comparison to SCC and HIC cracks. In contrast to SCC, corrosion fatigue fractures are typically transgranular, which is also the case for air fatigue failures. To further compare SCC with HIC, cracks from HIC are highly brittle, fast growing and usually unbranched while stress corrosion cracks are characteristically branched and grow at slower

rates. Hydrogen induced cracks are more often transgranular than intergranular, in contrast to SCC, in which intergranular cracking predominates. In addition, cathodic polarization initiates or enhances HIC but suppresses or arrests SCC. Any corrosive solution may produce HIC in a susceptible alloy, if hydrogen is liberated on the surface. On the other hand, SCC requires a specific and usually different dissolved species for each alloy [8].

2.3 Problematic Weld Discontinuities

At some level of examination, all welded structures contain pre-existing cracks, crack-like flaws or other imperfections to some degree. A welding defect is a discontinuity that cannot be tolerated in a specific weldment. The most significant of these are usually associated with geometric stress concentrations, such as abrupt changes in section, weld toes, weld roots, weld start/stop positions (including arc-strikes), hydrogen cold cracking, liquation cracking, solidification cracking, incomplete weld penetration, lack of fusion, stress relief (reheat) cracking, and even weld porosity and trapped slag [9]. The shape or dimensions of acceptable discontinuities are usually described in fabrication codes or specifications applicable to the construction of a particular component (e.g. ANSI/AWS D1.1, *Structural Welding Code - Steel*, and ASME *Boiler and Pressure Vessel Code*). Incomplete weld penetration is one of the more serious weld defects and has been a potent cause of fracture initiation and propagation in weldments. Other sources of fracture initiation in welded joints have included lack of weld fusion, grossly defective welds, and various other types of welding cracks and crack-like flaws in the roots of single-sided welds [9].

The following sections are therefore devoted to a discussion regarding several of the most serious weld discontinuities including some of their known causes and proven methods of

prevention. This background information will aid in determining the cause of the failure of the circumferential weld seam in the disc filter core pipe.

2.3.1 Incomplete Fusion

Incomplete fusion is defined in ANSI/AWS A3.0, *Standard Welding Terms and Definitions* [10], as a weld discontinuity in which fusion did not occur between weld metal and fusion faces or adjoining weld beads. *Figure 2.1* illustrates various possible locations of incomplete fusion. The discontinuity can be attributed to design, procedure, or technique. For example, when a welded joint is designed with an extremely narrow groove angle, the risk of incomplete fusion into the groove face is much greater. Manipulation of the welding arc is probably the most common cause of incomplete fusion. A welder's ability to manipulate the welding arc is considered a primary purpose for welder performance qualification testing. Travel speed, weave pattern and dwell times are just a few examples of arc manipulation.
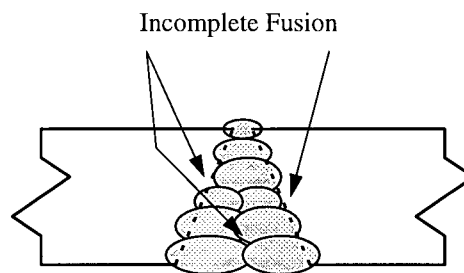
Incomplete Fusion

Figure 2.1 **Multipass Weld with Incomplete Fusion**

Joint cleanliness may also affect the probability of incomplete fusion. The wetting action of the molten pool is optimum when the adjoining groove faces or weld beads maintain their

maximum surface energy. Dirt, grease and other contaminants will only reduce this surface energy, thus reducing the wetting action [11].

2.3.2 Incomplete Joint Penetration

Incomplete joint penetration, also commonly referred to as Lack Of Penetration (LOP), is defined in ANSI/AWS A3.0 as a root condition in a groove weld in which weld metal does not extend through the joint thickness. Two examples of incomplete joint penetration are shown in *Figure 2.2*. Typically, incomplete joint penetration is caused by insufficient heat input to melt through a given joint cross-section. A backing strip may be used in many applications to facilitate root pass fusion; however, proper manipulation of the welding arc remains crucial. Numerous applications of butt joints are unsuitable for using backing material. In some situations, the back side of the joint is simply not accessible. In other cases, a backing strip creates an internal obstruction that remains after the joint is completed. Pipe and tube butt joints are common examples which may not be suitable for backing strips, particularly when the backing strip has the potential to cause a flow restriction [11].

Incomplete Joint Penetration
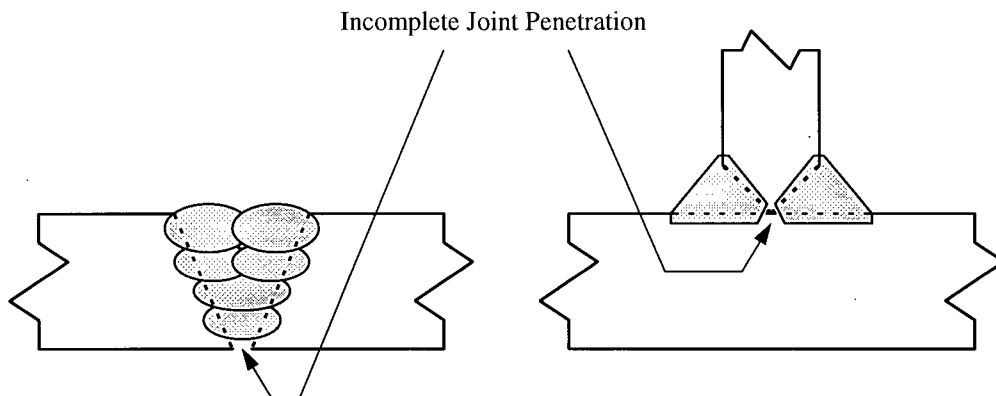
Figure 2.2 **Examples of Incomplete Joint Penetration**

2.3.3 Cracks

Cracks are defined in ANSI/AWS A3.0 as fracture-type discontinuities characterized by a sharp tip and high ratio of length and width to opening displacement. Many specifications clearly state that all welds shall be free of cracks. This type of discontinuity is usually considered to be the most detrimental to a welded joint because cracks have the potential to propagate and cause catastrophic failure. As noted in the introductory section, there are many types of cracks that may occur in and adjacent to welded joints. Some of the different types of cracks are illustrated in *Figure 2.3*. Generally, cracks may be divided into two categories: hot cracks and cold cracks. Hot cracks occur before the weld has completely solidified while cold cracks occur after the weldment has cooled, sometimes to ambient temperature.

LEGEND

1	Crater crack
2	Face crack
3	Heat affected zone crack
4	Lamellar tear
5	Longitudinal crack
6	Root crack
7	Root surface crack
8	Throat crack
9	Toe crack
10	Transverse crack
11	Underbead crack
12	Weld interface crack
13	Weld metal crack
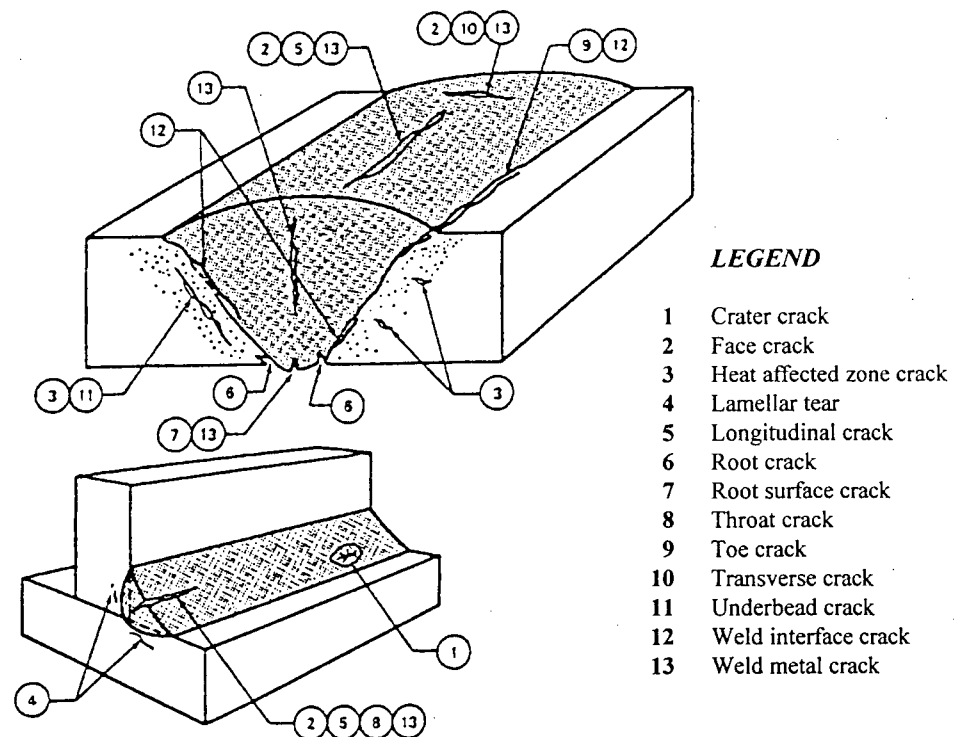
Figure 2.3 **Types of Cracks Associated with Welding [11]**

Each type of weld crack may be linked to a few specific causes. For example, a longitudinal face crack in the weld metal may be caused by an excessive depth-to-width ratio of the fusion zone. Microstructural conditions coupled with a high degree of restraint and contraction (i.e. cooling) stresses may result in a longitudinal face crack as the weld cools.

A Heat Affected Zone (HAZ) cold crack may be caused by hydrogen embrittlement of a narrow band of the heat affected zone adjacent to the fusion zone of the weld. This type of crack was discussed in one of the previous sections regarding environmentally induced cracking. This portion of the HAZ may be transformed to a brittle martensitic structure on cooling from welding temperatures. The likelihood of forming local brittle zones in the heat affected zone becomes greater with increasing carbon and alloy content of both the base and filler metals. Any increase in the carbon content will usually be accompanied by an increase in hardness and a decrease in ductility of the material. When these conditions are present in the HAZ, the weldment is considerably more susceptible to hydrogen embrittlement.

2.3.4 Undercut

Undercut is defined in ANSI/AWS A3.0 as a groove melted into the base metal adjacent to the weld toe or weld root and left unfilled by weld metal. Undercut may be detrimental to a welded joint depending on its shape (e.g. if it resembles a sharp notch) and orientation with respect to the loading conditions imposed on the component or structure. The most common causes of undercut are excessive currents, voltages or travel speeds. Undercut is easily repaired on the face of the weld; however, it is virtually impossible to repair at the weld root in pipe and tube welds without first destroying the weld joint. Preventing undercut by employing proper welding parameters and techniques is certainly more economical.

2.3.5 Porosity

Porosity is defined as a cavity-type discontinuity formed by gas entrapment which occurs during solidification of the weld bead. This type of volumetric discontinuity is usually caused by contaminants entering the welding arc. Volatilization of these contaminants causes the formation of gas pockets in the molten weld metal. If solidification occurs rapidly enough, these gas pockets may be trapped in the fusion zone of the weld. Contaminants are often admitted into the welding arc due to a breakdown of the shielding gas or if the gas flow is not sufficient to provide an inert environment. Contaminants may also enter the weld deposit if they are picked up from the surface of the materials being welded. Porosity is almost always permissible, at least to some extent, in the final weldment. However, specifying the acceptable limits for porosity may be somewhat complex. The maximum size of a pore, the minimum distance between groups of small pores, and/or the maximum number of pores smaller than a specified size are typical criteria for specifying these limits.

2.4   Analysis of the Core Pipe Weld Failure

The operation of disc filters to remove fibers from paper machine white waters for thickening (decker) or save-all applications was summarized in the introductory chapter. Concerns regarding corrosion associated with ongoing programs to close-up white water systems by way of increased recycle were also discussed. In the present chapter, the topics of environmentally induced cracking and problematic weld discontinuities have been addressed. A thorough analysis is now performed on the circumferential weld failures which occurred on Ingersoll-Rand's type 316L stainless steel disc filter core pipe.

The outer shell of the core pipe is fabricated by welding together 8″ wide annular rings of alternating material thickness. Each disc filter is mounted to a thick support ring which contains 18 openings around the circumference to accommodate the flow of filtrate from each filter segment. A thin ring located between each support ring functions simply as a spacer between adjacent disc filters. Each ring must be installed individually over the inner shell and division bars that separate adjacent channels. Consecutive rings are then affixed to one another with a full length, circumference groove weld.

Upon initial examination of the failures, the primary region of cracking appeared to be confined to the circumferential weld seams, as illustrated in *Figure 2.4*. The most severe cracking was observed in the central third section of the core pipe where the bending stresses
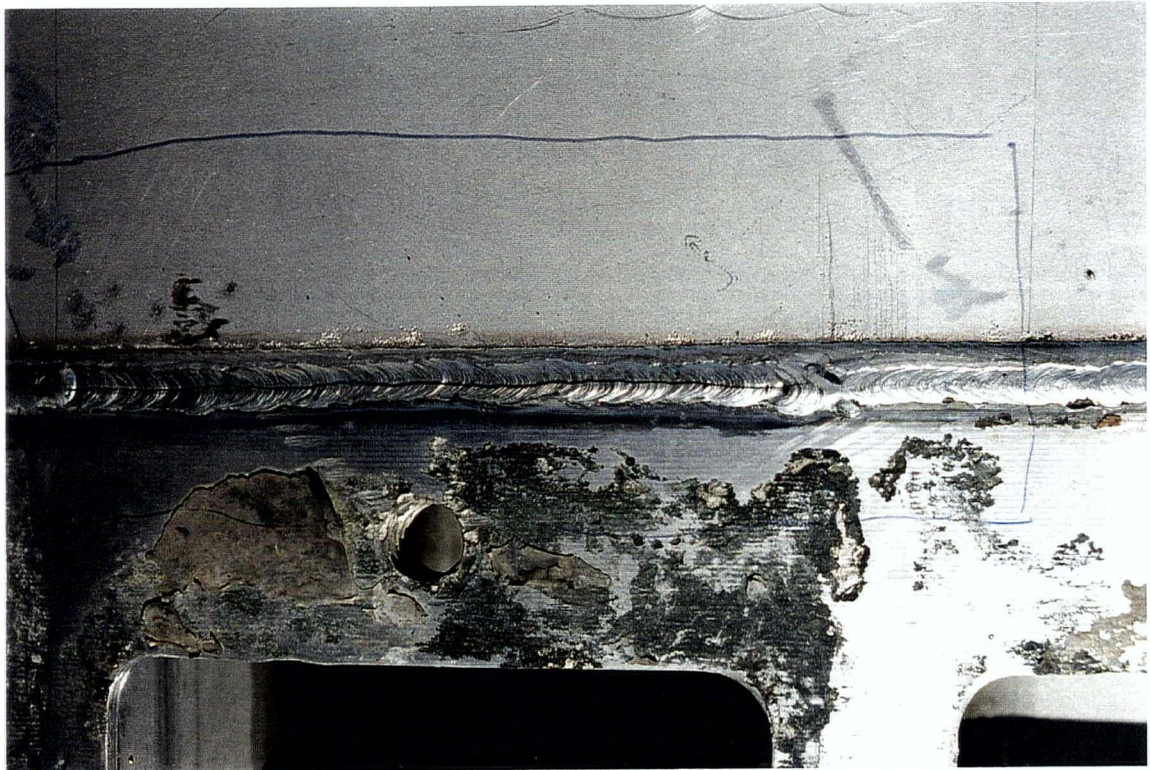
Figure 2.4 **Typical Crack in the Circumferential Weld Seam**

in the outer shell are the highest. In many cases, a number of separate cracks of varying

dimensions (from < 1″ to > 6″) were observed around the circumference of a single weld. In

addition to the primary weld cracking problem, crevice corrosion was clearly visible on the

outer surface in the vicinity of the openings and around the bolt holes used for mounting the

filter segments. Narrow bands of pitting corrosion were also observed on the spacer rings

directly adjacent to the weld seam.

Metallographic cross sections were removed from three different circumferential welds

which exhibited hairline cracks on their exterior surface. Each specimen may be identified

according to the labels given in *Figure 2.5*. Specimens *1A*, *2A*, *2D* and *3A* were taken from

the ends of the respective weld samples where no cracks were visible on the exterior surfaces.

Figure 2.5 Specimens Removed from Three Circumferential Welds

Specimens *2B/2C* and *3B/3C* were taken from two separate samples which each included a single crack approximately 2″ in length at the surface. In both cases, a transverse cut was made across the center of the crack dividing the specimens into two separate parts. Visual examination of all six specimens revealed the following general features:

- Two specimens (*1A* and *2A*) suffer from poor fit-up on the inner surface of the joint.
- Specimens *1A*, *2A*, *2D* and *3A* appear to have small cracks on the interior surface of the joint although cracking is not evident on the exterior surface.
- Five specimens showed no evidence of through penetration on the interior surface.
- One specimen (*3B/3C*) exhibited spotty through penetration, but the weld root appeared very porous at these locations.
- Most cracking on the exterior surface corresponds to the interior joint line.

These observations seem to indicate that the circumferential cracks may be attributed to lack of penetration discontinuities since the cracks appear to initiate from the root of the weld. Even when full penetration of the joint was achieved, the resulting weld root contained considerable porosity.

Specimens *1A*, *2A*, *2D* and *3A* were mounted in Lecoset 100 castable mounting material and ground to a smooth finish applying a five-stage wet grinding process that involves the successive use of increasingly finer abrasive papers (i.e. 60, 120, 180, 320 and 600 grit). The specimens were then polished to a mirror-like finish using rotating disks covered with napless cloth impregnated with two increasingly finer diamond suspensions (i.e. 6 μm and then 1 μm). The resulting surfaces were then etched to delineate the microstructures of the stainless steel specimens for metallographic examination. Etching was accomplished by swabbing the surface of each specimen for a few seconds with Kalling's reagent consisting of 2 g $CuCl_2$, 40 ml HCl, 40 to 80 ml ethanol (95%) or methanol (95%), and 40 ml water.

The specimens were examined at various levels of magnification using a conventional visual microscope. Photomacrographs of the etched surface of specimen *1A* are illustrated in *Figure 2.6*. In the upper photo, the etchant has successfully delineated the two welding passes and revealed a large crevice adjacent to the weld root. The parent material side of the defect appears rougher than the edge of the root pass which may be indicative of corrosion. A narrow, unbranched crack emanating from the top of the crevice has also propagated into the root pass weld bead, as illustrated in the lower photo. The advanced stage of the defect makes it difficult to determine whether or not the root pass penetrated through the full thickness of the joint. Crevice corrosion originating from incomplete fusion might also produce a similar condition.

Poor joint fit-up in specimen *2A* is clearly visible in the photomacrographs shown in *Figure 2.7*. A sizable lack of penetration defect is also evident, and corrosion appears to have broadened the initial discontinuity. Furthermore, a single crack has initiated from the tip of the defect and has propagated through the HAZ and into the root pass weld bead. Visual examination of specimen *3A* (photomacrographs are not shown) revealed a substantial lack of penetration defect, similar to that found for specimen *2A*, but without any corrosion.

Photomacrographs corresponding to the non-etched and etched surface of specimen *2D* are presented in *Figure 2.8 (a)* and *(b)*, respectively. The primary defect is certainly a severe lack of penetration: the root pass barely penetrates halfway through the joint thickness. Parent material beneath the weld root has also suffered from severe corrosion which has produced a substantial internal pit below the root pass. A secondary region of cracking appears to have initiated from pitting on the internal surface of the shell, and the branched, multiple-crack morphology is characteristic of stress corrosion cracking.
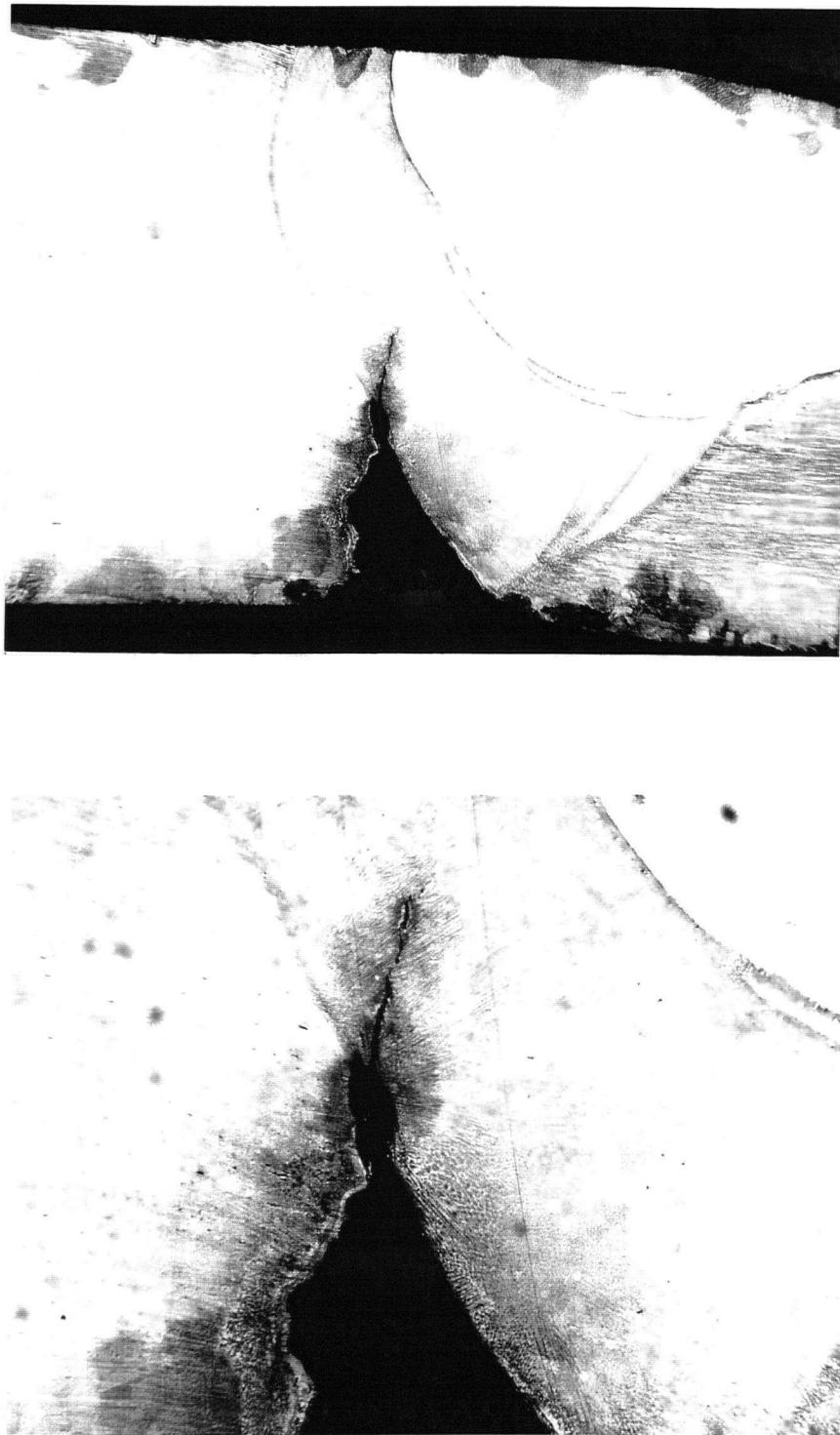
Figure 2.6 **Photomacrographs of Specimen** *1A:* **Etched** (Upper: 16 ✕; Lower: 40 ✕)
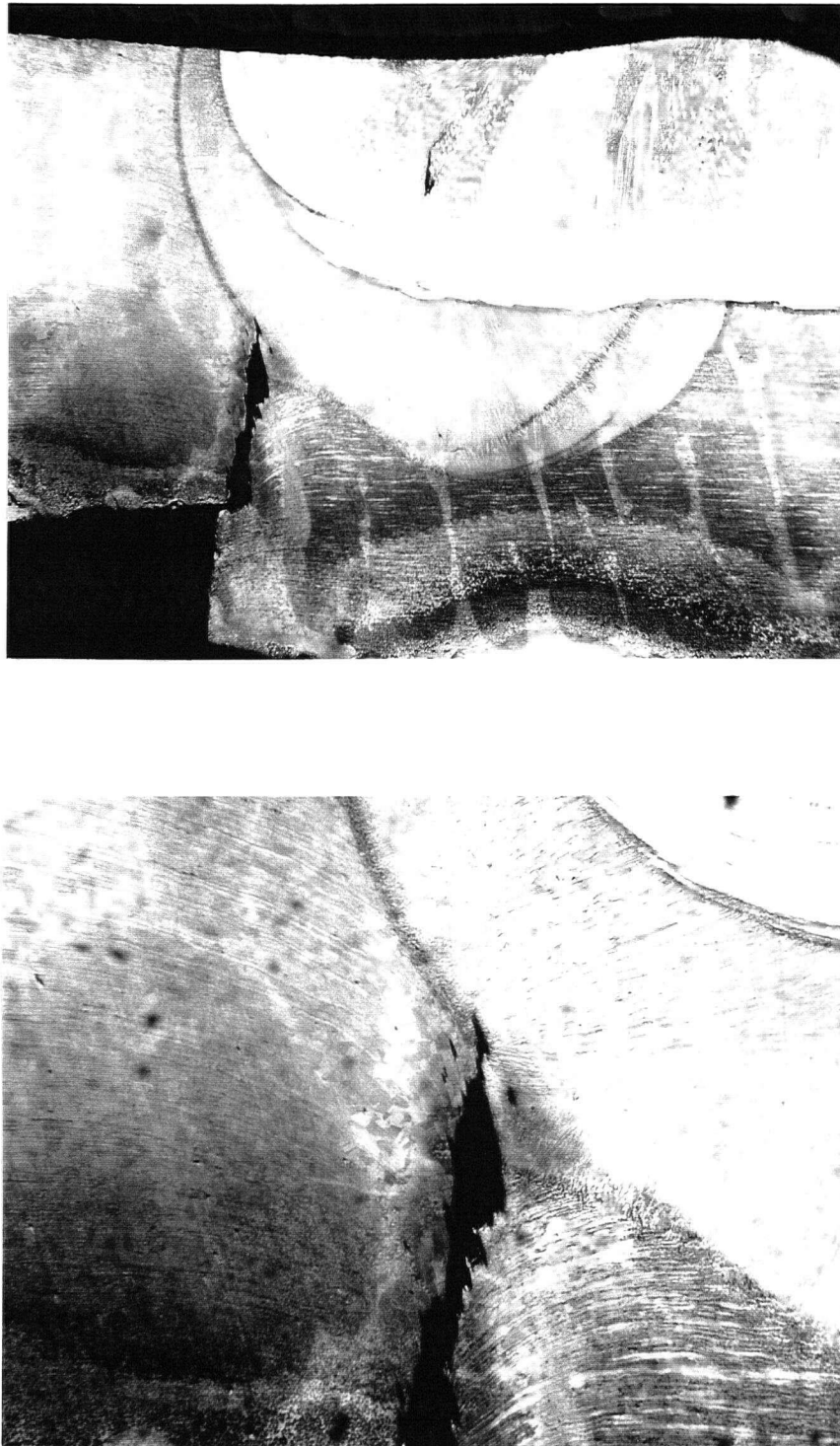
Figure 2.7 **Photomacrographs of Specimen 2A: Etched** (Upper: 16 ×; Lower: 40 ×)
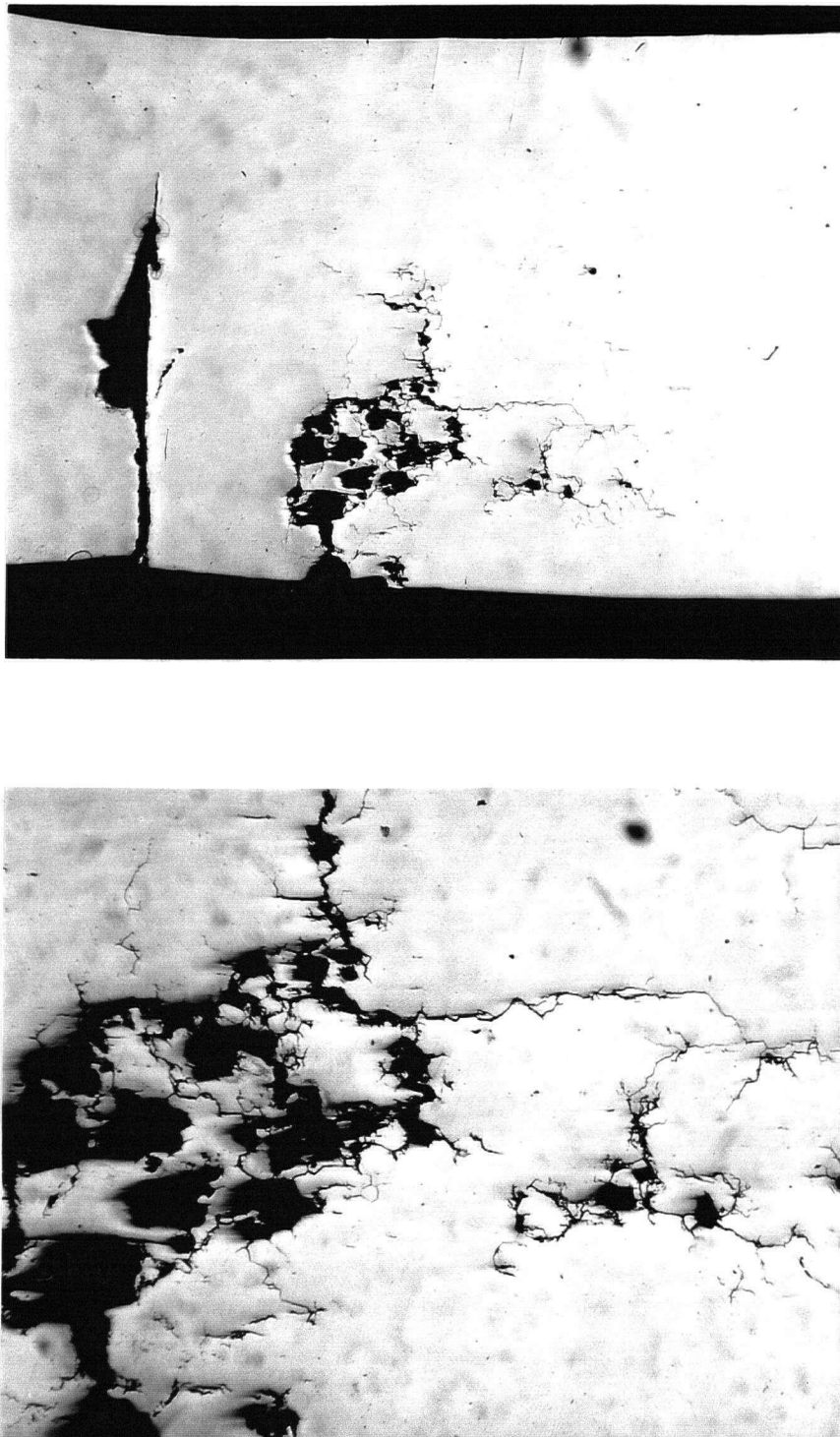
Figure 2.8 (a) **Photomacrographs of Specimen** *2D:* **Non-etched** (Upper: 16 ✕; Lower: 40 ✕)

Figure 2.8 (b) **Photomacrographs of Specimen** *2D:* **Etched** (Upper: 16 ✕; Lower: 40 ✕)

The cracks in specimens *2B/2C* and *3B/3C* were forced open by simple mechanical overload. The fracture surfaces were initially covered with a dark, fibrous residue that was subsequently removed by ultrasonically vibrating the specimens in ethanol. Some regions of the fractures appeared to be hammered, likely due to the continuous abrasion of mating surfaces. Undamaged areas of the fracture surfaces were therefore selected and then examined using both visual and scanning electron microscopy (SEM) techniques.

Visual examination aided by low power microscopy revealed the following features on the mating surfaces of specimen *3B/3C*:

- Through-thickness penetration was achieved at a single position in the middle of the specimen, as shown in *Figure 2.9*. However, grinding marks discernible on the thicker (support) ring reveal a ridge of base material that was not fused during welding. This ridge was certainly caused by lack of penetration because the specimen was found to have satisfactory fit-up on the inner surface of the joint.

- The failure surface is typical of brittle fracture which occurs by cleavage of the metal, exposing a granular, crystalline surface. These attributes make it easy to distinguish between the actual failure surface and that resulting from the overload since the latter produced a ductile fracture, exposing a ruptured surface with a silky appearance.

- A thumbnail or ratchet mark is clearly visible in *Figure 2.10*, and a substantial pit has developed on the ridge of base material at this location. Several other thumbnails were also observed along the same fracture surface. These features indicate that the crack had multiple points of origin.

- The visual appearance of the fracture surface beyond each thumbnail is typical of fatigue with macroscopic beach marks. Well-defined striations (parallel lines) are also evident with increased magnification, as illustrated in *Figure 2.11*.

- Similar observations were made for specimen *2B/2C*.

The crack front in specimen *3C* was subsequently examined using SEM techniques. The scanning electron fractograph, shown in *Figure 2.12*, was initially thought to reveal branched,
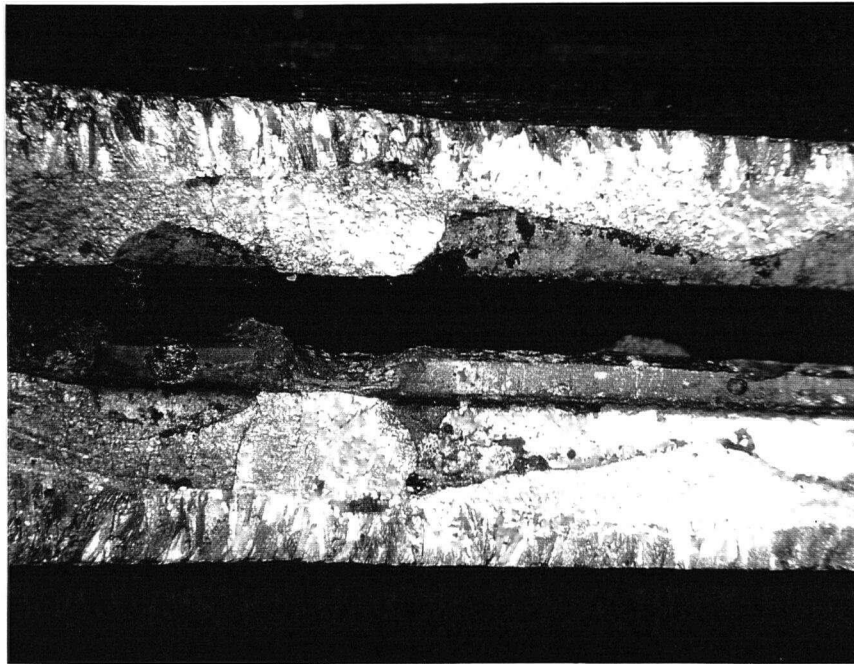
Figure 2.9 **Photomacrograph of Specimen *3B/3C*** (8 ✕)
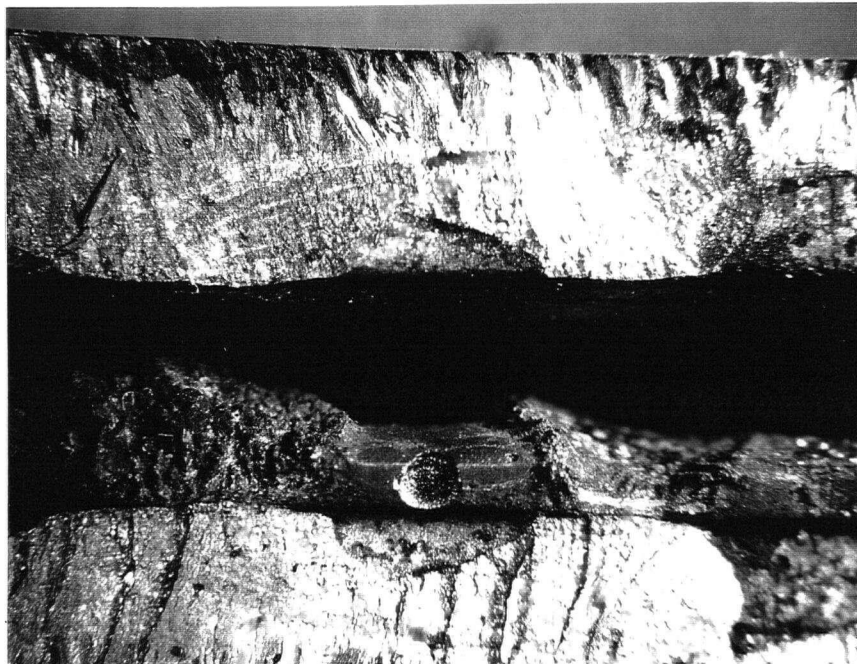
Figure 2.10 **Photomacrograph of Specimen *3B/3C*** (10 ✕)
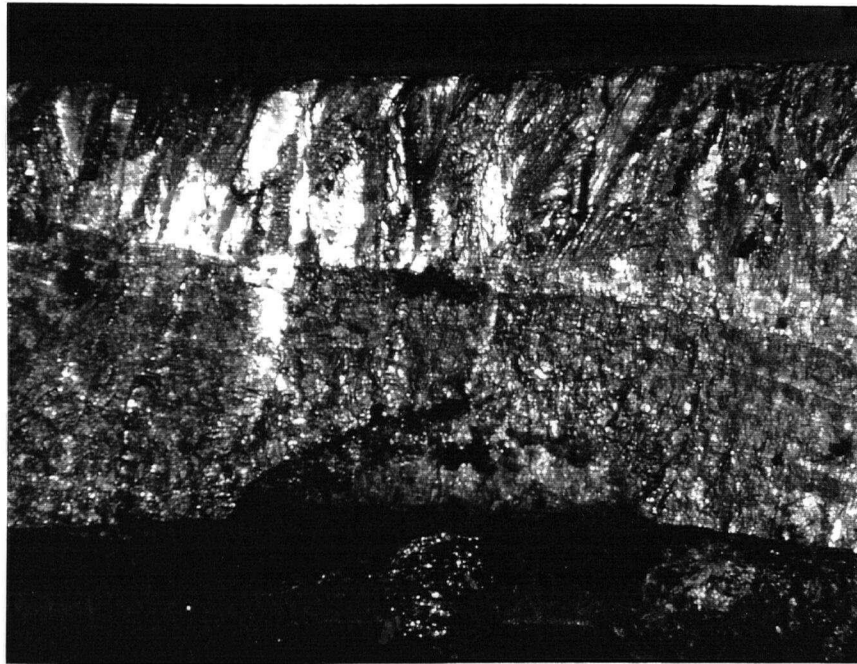
Figure 2.11 **Photomacrograph of Specimen *3C*** (20 ×)
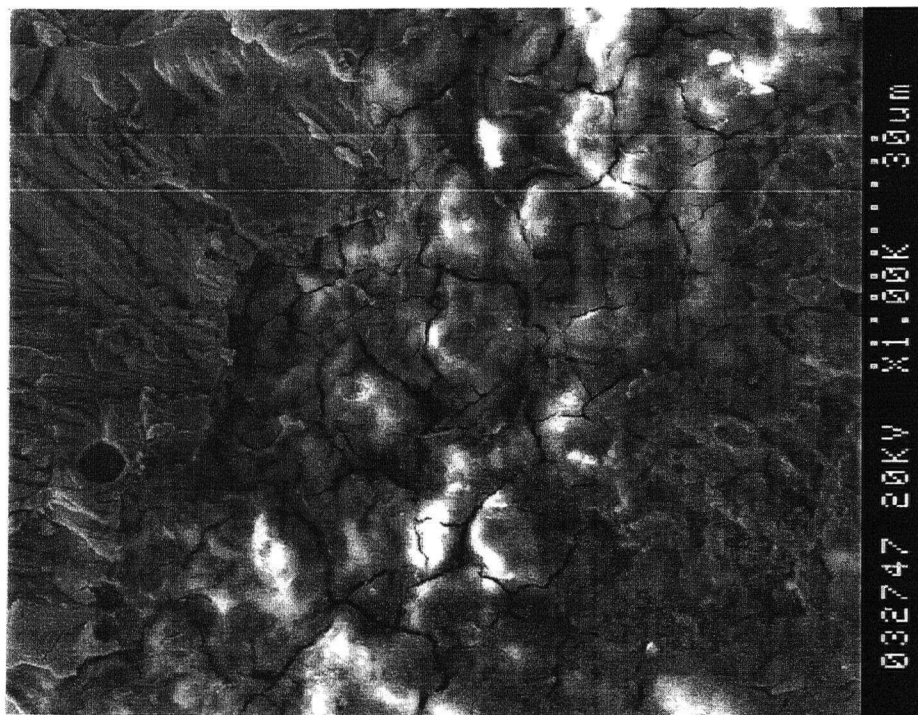
Figure 2.12 **Scanning Electron Fractograph of Specimen *3C*** (1000 ×)

intergranular stress corrosion cracking. However, further scrutiny at a higher magnification revealed a thin layer of scale near the tip of the crack, as illustrated in *Figure 2.13*, and the apparent cracking is limited to the surface incrustation.
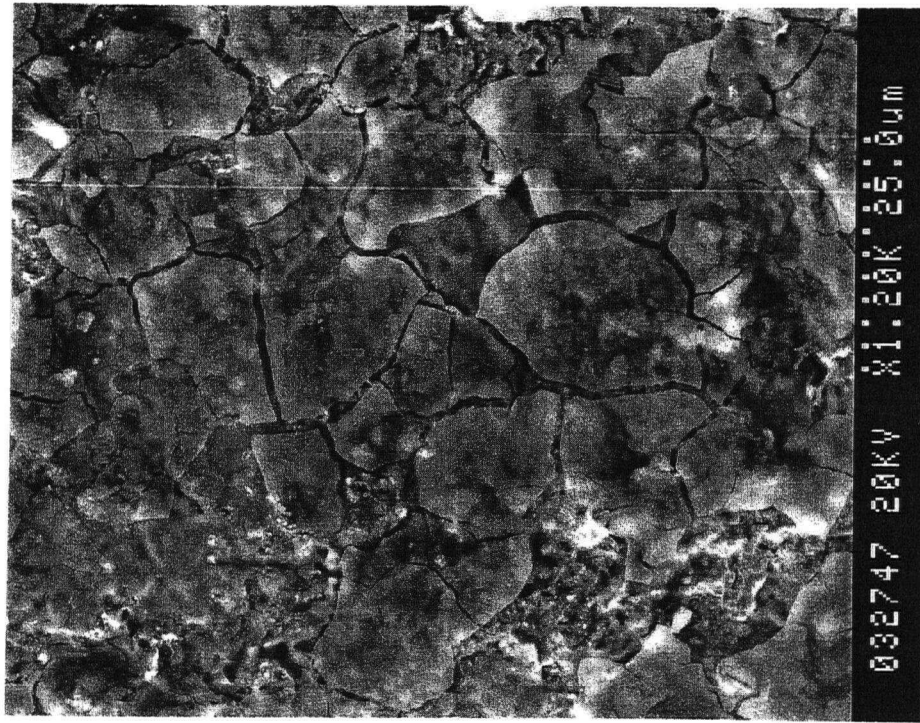
Figure 2.13 **Scanning Electron Fractograph of Specimen** *3C* (1200 ✕)

Based on the foregoing observations, it may be concluded that the circumferential weld cracking problem was caused by corrosion fatigue emanating from lack of penetration root defects. In all likelihood, the narrow gap between abutting rings in the outer shell served to increase the concentration of the local (white water) environment and acted as a preferential site for crevice corrosion. Porosity at the same location may have aggravated the situation. The crack initiation period is therefore insignificant when compared to the total service life of the core pipe, and crack propagation occurs by corrosion fatigue induced by the fluctuating stresses that are imposed during routine operation. Although stress corrosion cracking was

identified at one specific location, it was not a contributing factor in the failures of the circumferential weld seams.

Corrosion fatigue cracking (CFC) may be mitigated by any means that reduces the general corrosion rate, including inhibitors, cathodic protection (when HIC is not a danger), reduction of oxidizers, or increase in pH. A change to a more corrosion-resistant alloy (i.e. duplex stainless steels) may also be effective, but only if the corrosion rate is sufficiently low. Barrier coatings to exclude the corrosive solution from the alloy surface and sacrificial zinc (galvanized) coatings to cathodically protect steel at breaks in the coating may also be used to prevent CFC. Redesigning the component to reduce or remove cyclic stresses will, of course, prevent or improve resistance to CFC. When appropriate, shotpeening may also be helpful in reducing tensile stresses [8].

For the disc filter core pipe examined in the present investigation, the proposed solution involves a number of fundamental design changes which, if successful, will have a considerable impact on reducing the cyclic stresses imposed during routine operation. Development and implementation of these changes, however, are beyond the scope of this research. In the final chapter of this thesis, a new core pipe design will be compared to the original Ingersoll-Rand design using finite element analysis and fracture mechanics concepts developed in the forthcoming two chapters.

CHAPTER 3

FINITE ELEMENT SUB-MODELING

3.1   Introduction and Motivation

Consider a beam in equilibrium, fixed at one end and subject to an arbitrary loading condition on the other, as illustrated in *Figure 3.1 (a)*.   To determine the resulting displacement solution and stress distribution in the beam, a finite element analysis may be performed using the numerical model shown in *Figure 3.1 (b)*. Now consider the blue region in the center of the web consisting of eight shell elements, as shown in *Figure 3.2 (a)*. If the actual purpose of this analysis was to investigate the stress concentration around various slots made in the center of the web (dashed lines), the present model of the beam would not be suitable due to the coarse finite element mesh.   The entire model of the beam could be remeshed using much smaller elements, but the larger model would place significantly higher demands on the hardware, in terms of required disk space, and on the software program due to an increase in the maximum wavefront.

Local mesh refinement could be attempted in the blue region itself, as illustrated in *Figure 3.2 (b)*, but it would be difficult to maintain element compatibility in the central region of the web without affecting the elements that comprise the beam flanges.   This inconvenience is frequently encountered when performing local mesh refinement as topological changes to one region of the model tend to propagate throughout a good portion of the remaining regions of the model.   When local mesh refinement produces large variations in the size of adjacent elements, numerical ill-conditioning of the stiffness matrix may be imminent and may lead to inaccurate results.
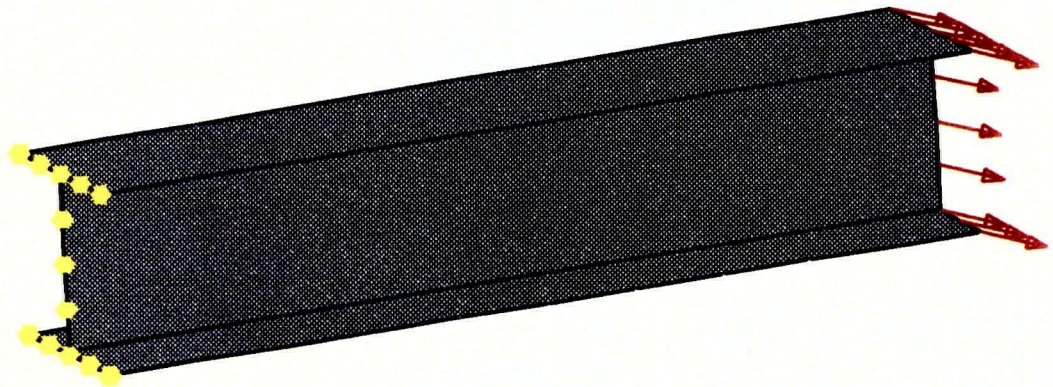
Figure 3.1 (a) **Geometry of a Typical Cantilever Beam**
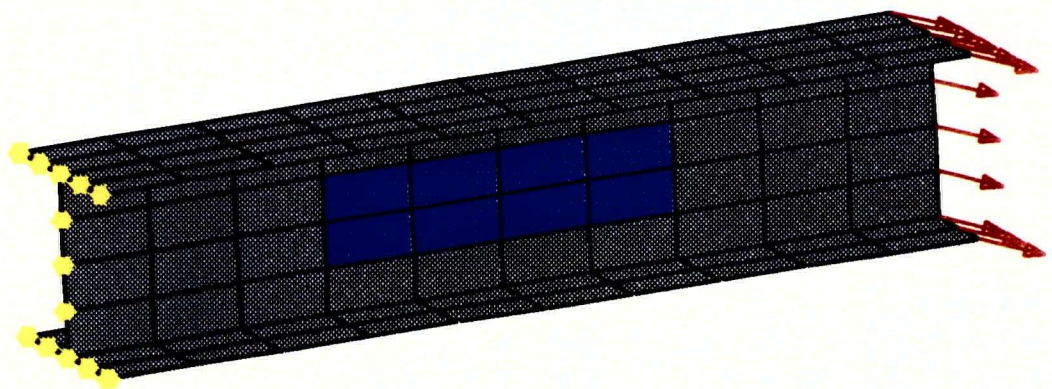
Figure 3.1 (b) **Finite Element Model of the Cantilever Beam**
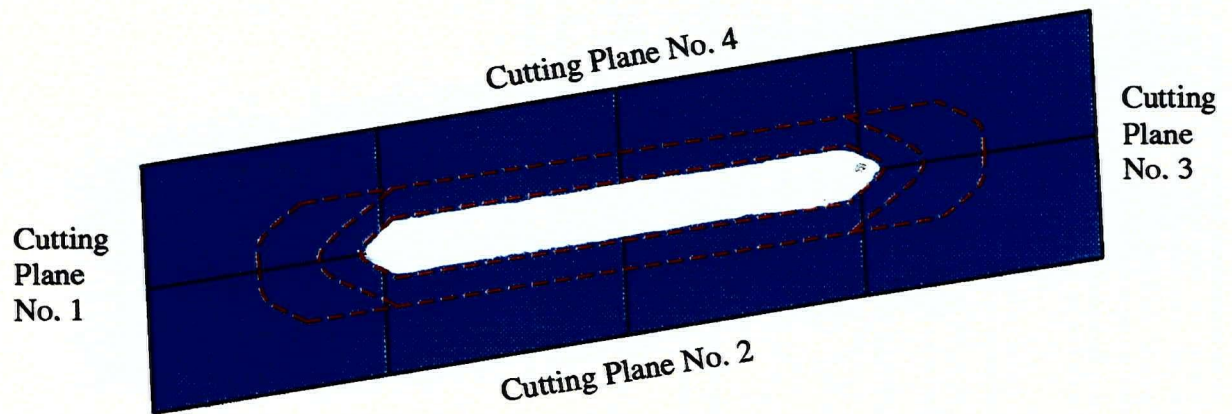
Figure 3.2 (a) **Original Shell Element Model of the Web**
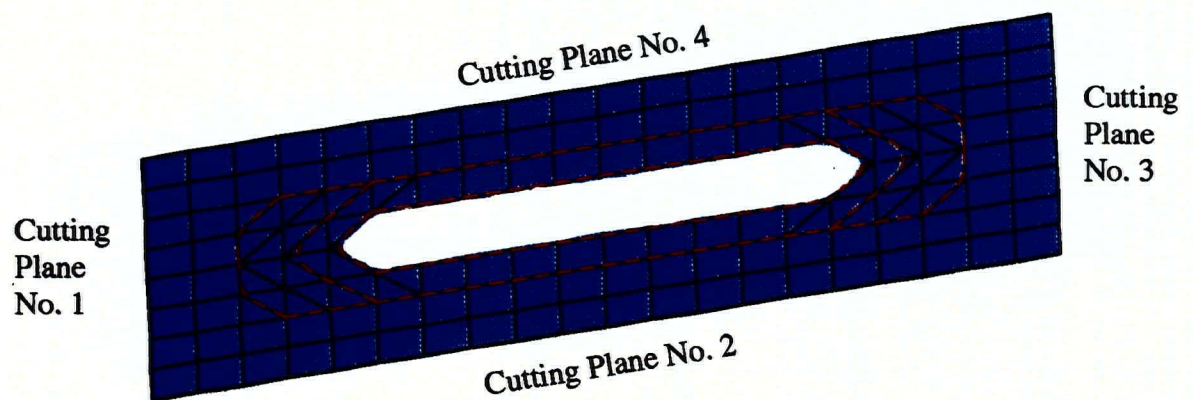
Figure 3.2 (b) **Local Mesh Refinement in the Web**

Finite element procedures which employ local mesh refinement also suffer from another disadvantage in that the entire finite element model must be resubmitted for the analysis of each new design alternative. Consequently, this approach is generally not an effective use of computational resources, that is, assuming both the hardware and software program are capable of handling the larger model.

The two meshes illustrated in *Figure 3.2* may be considered as sub-models of the original finite element model of the beam. The first or *coarse* sub-model (*Figure 3.2 (a)*) has the same finite element topology as the blue region in the original model while the second or *refined* sub-model (*Figure 3.2 (b)*) has a much finer mesh. Now assume that a finite element analysis has been performed on the original model of the beam. If a sub-region could be modeled with a finer mesh while keeping the number of boundary nodes unchanged, there would be a one-to-one correlation on the boundary. The displacement solution from the coarse mesh may be used as boundary conditions for the sub-region, and no approximation is introduced. In such cases, the analysis is identical to the commonly used superelement or sub-structuring technique in finite elements. Unfortunately, it is not always possible to have such a one-to-one correlation, as seen in the earlier beam example, and a practical need exists to calculate appropriate boundary conditions for a sub-region with an arbitrarily fine mesh.

These practical considerations have lead to the development of several sub-modeling techniques which offer more flexibility in modeling the sub-region. Carey [12] and Schwartz [13] have taken an approach using constraint equations for local refinement within a sub-region that reduces propagation throughout the whole model. Hirai et al. [14] have used a zooming method which identifies the sub-region boundary then eliminates all the internal degrees of freedom in the whole model outside the sub-region and then refines the sub-region. The specified boundary stiffness/force method extracts the stiffness coefficients

and the internal nodal forces from the whole model solution acting on the sub-region boundary [15]. These become the boundary conditions for a separate sub-region model.

Each of these methods requires that the computer code be able to perform the necessary operations for the method to execute successfully. The local refinement method requires the ability to input constraint equations. The specified boundary displacement method is extremely sensitive to small errors in the boundary displacements, but this method can be done manually if the displacement output is available. The ANSYS [16] finite element code has an automated implementation to interpolate for displacements using the element interpolation functions so that the boundary nodes do not have to coincide with the full model nodes. The specified boundary stiffness/force method requires access to the structure's stiffness matrix coefficients and internal nodal forces which are usually not available in most commercial finite element codes. The following section introduces a different method to deal with boundary condition incompatibilities which provides an alternative approach to finite element sub-modeling or sub-structuring. In the final section of this chapter, two different numerical examples are presented to demonstrate the procedure.

3.2   Nodal Force Boundary Condition (NFBC) Program

3.2.1 General Methodology

Consider the same beam example and finite element models used in the previous section, and assume the nodal displacement solution has been obtained from the full model analysis. In the following discussion, the sub-model faces that were not on the exterior surface of the original model are to be referred to as *cutting planes*. In this example, both sub-models contain four separate cutting planes and two original surfaces. The nodal displacement

solution from the full model analysis could be applied as displacement constraints on the boundary nodes in the coarse sub-model, as shown in *Figure 3.2 (a)*. In the case of a shell element model, each displacement or rotation constraint would generate a nodal reaction force or moment. Summing these reactions over the faces of the sub-model would produce a resultant force and moment for each cutting plane. Now consider the refined sub-model shown in *Figure 3.2 (b)*. The basic idea in the proposed technique is to take one cutting plane at a time and apply forces and moments (force couples) on the refined sub-model that will be equivalent (in a global sense) to the global reactions obtained from the coarse model.

To simplify the following discussion, *cutting plane one in the coarse sub-model* will be referred to as *face I-a*, while *cutting plane one in the refined sub-model* will be referred to as *face I-b*. Let *m* equal the number of nodes on face I-a and *n* equal the number on face I-b. The components of the total reaction force, acting on face I-a, may be determined as follows:

$$F_x^{I-a} = \sum_{i=1}^{m} \left\{ f_{ax}^{(i)} \right\} \quad F_y^{I-a} = \sum_{i=1}^{m} \left\{ f_{ay}^{(i)} \right\} \quad F_z^{I-a} = \sum_{i=1}^{m} \left\{ f_{az}^{(i)} \right\} \tag{3.1}$$

where $f_{ax}^{(i)}$, $f_{ay}^{(i)}$, and $f_{az}^{(i)}$ are the nodal reaction force components on face I-a acting in the global x-, y-, and z-directions, respectively. If the centroid of face I-a has coordinates (x_a^c, y_a^c, z_a^c), the components of the total reaction moment, acting about the face centroid, may be determined from the nodal reaction forces and moments as follows:

$$M_x^{I-a} = \sum_{i=1}^{m} \left\{ m_{ax}^{(i)} + (y_a^{(i)} - y_a^c) * f_{az}^{(i)} - (z_a^{(i)} - z_a^c) * f_{ay}^{(i)} \right\}$$

$$M_y^{I-a} = \sum_{i=1}^{m} \left\{ m_{ay}^{(i)} + (z_a^{(i)} - z_a^c) * f_{ax}^{(i)} - (x_a^{(i)} - x_a^c) * f_{az}^{(i)} \right\} \tag{3.2}$$

$$M_z^{I-a} = \sum_{i=1}^{m} \left\{ m_{az}^{(i)} + (x_a^{(i)} - x_a^c) * f_{ay}^{(i)} - (y_a^{(i)} - y_a^c) * f_{ax}^{(i)} \right\}$$

where $m_{ax}^{(i)}$, $m_{ay}^{(i)}$, and $m_{az}^{(i)}$ are the reaction moment components acting about the global x-, y-, and z-axes, respectively, and $x_a^{(i)}$, $y_a^{(i)}$, and $z_a^{(i)}$ are the coordinates of the ith node on face I-a. Now consider the refined sub-model, subject to an unknown set of nodal forces acting on all n nodes on face II. The components of the total applied force, acting on face II, may be determined as follows:

$$F_x^{I-b} = \sum_{i=1}^n \left\{ f_{bx}^{(i)} \right\} \quad F_y^{I-b} = \sum_{i=1}^n \left\{ f_{by}^{(i)} \right\} \quad F_z^{I-b} = \sum_{i=1}^n \left\{ f_{bz}^{(i)} \right\} \tag{3.3}$$

where $f_{bx}^{(i)}$, $f_{by}^{(i)}$, and $f_{bz}^{(i)}$ are the nodal force components on face I-b acting in the global x-, y-, and z-directions, respectively. Since both sub-models represent the same portion of the full model, face I-b will have the same centroid as face I-a (i.e. x_a^c, y_a^c, z_a^c). The components of the total applied moment, acting about the face centroid, may be determined from the applied nodal forces as follows:

$$M_x^{I-b} = \sum_{i=1}^n \left\{ m_{bx}^{(i)} + (y_b^{(i)} - y_b^c) * f_{bz}^{(i)} - (z_b^{(i)} - z_b^c) * f_{by}^{(i)} \right\}$$

$$M_y^{I-b} = \sum_{i=1}^n \left\{ m_{by}^{(i)} + (z_b^{(i)} - z_b^c) * f_{bx}^{(i)} - (x_b^{(i)} - x_b^c) * f_{bz}^{(i)} \right\} \tag{3.4}$$

$$M_z^{I-b} = \sum_{i=1}^n \left\{ m_{bz}^{(i)} + (x_b^{(i)} - x_b^c) * f_{by}^{(i)} - (y_b^{(i)} - y_b^c) * f_{bx}^{(i)} \right\}$$

where $x_b^{(i)}$, $y_b^{(i)}$, and $z_b^{(i)}$ are the coordinates of the ith node on face I-b. To achieve the objective stated above, the nodal forces imposed on face I-b must generate a resultant force and moment equivalent to those generated on face I-a. Accordingly, the resultant force and moment components must satisfy the following relations:

$$F_x^{I-a} = F_x^{I-b} \quad F_y^{I-a} = F_y^{I-b} \quad F_z^{I-a} = F_z^{I-b} \tag{3.5}$$

$$M_x^{I-a} = M_x^{I-b} \quad M_y^{I-a} = M_y^{I-b} \quad M_z^{I-a} = M_z^{I-b} \tag{3.6}$$

The following three step procedure was used to determine an appropriate set of nodal forces (for each cutting plane) which satisfies equations (3.5) and (3.6):

i. Compute a set of **uniform** nodal forces which generates the required global resultant force. These forces inadvertently generate a resultant moment about the face centroid.

ii. Adjust the required resultant moment by the amount already generated by the uniform nodal forces in step (i), then compute a set of **linearly distributed** nodal forces which generates the remaining moment. This set of nodal forces must not produce a net resultant force; otherwise, force equilibrium will not be satisfied.

iii. Using the Principle of Superposition, combine the sets determined in steps (i) and (ii) above, and then apply the new set of nodal forces to the numerical model.

The first step in the above procedure is accomplished by simply dividing the required global force components by the number of nodes on face I-b. Accordingly, the components of the uniform nodal forces may be determined as follows:

$$f_{bx}^{(i)} = \frac{F_x^{I-a}}{n} \qquad f_{by}^{(i)} = \frac{F_y^{I-a}}{n} \qquad f_{bz}^{(i)} = \frac{F_z^{I-a}}{n} \qquad (3.7)$$

The moments generated by the uniform nodal forces about the face centroid may be calculated using equation (3.4). The remaining moment which must be generated by the linearly distributed nodal forces may be determined, in component form, as follows:

$$M_x^{I-b} = M_x^{I-a} - M_x^{\circ I-b} \qquad M_y^{I-b} = M_y^{I-a} - M_y^{\circ I-b} \qquad M_z^{I-b} = M_z^{I-a} - M_z^{\circ I-b} \qquad (3.8)$$

where $M_x^{\circ I-b}$, $M_y^{\circ I-b}$, and $M_z^{\circ I-b}$ are the components of the resultant moment generated by the uniform nodal forces on face I-b. To complete step (ii) in the above procedure, it is necessary to determine another set of nodal forces which generates the moments computed using equation (3.8). A numerical algorithm was developed to accomplish this objective.

3.2.2 Numerical Algorithm

The following procedure may be used to determine a set of nodal forces which generates a specified global moment (three components) about the centroid of any given face while, at the same time, produces a net global force equal to zero. For the purpose of clarity, the algorithm is presented mainly in a descriptive, text format. The numerical algorithm developed for the complete Nodal Force Boundary Condition (NFBC) program is included in Appendix A. Furthermore, the following steps pertain only to step (ii) in the three step procedure outlined in the previous section.

Step 1   Determine the minimum and maximum x-, y-, and z-coordinates for face I-b. Using these coordinates as (8) distinct vertices, a fictitious bounding box may be pictured which fully encompasses the entire face. For example, if the minimum and maximum x-coordinates are (x_{min}, x_{max}), then the $x = x_{min}$ and $x = x_{max}$ planes will form two sides of the bounding box. The other four sides are located in the same manner using the y- and z-coordinates. A typical bounding box is illustrated in *Figure 3.3*.

Step 2   Locate the centroid of the bounding box which also coincides with the centroid of the face. Using the centroid as a dividing point, the bounding box may be divided into 12 overlapping regions (labeled **A** through **L** in *Figure 3.3*). Regions **A** - **D** are used to determine the magnitude of the nodal forces in the y-direction only. Regions **E** - **H** are used for the z-direction nodal forces, and the x-direction nodal forces are determined using regions **I** - **L**.

Step 3   The basic strategy is to first compute the required forces at the vertices of the bounding box which generate the appropriate global moments. The second step will be to transfer the forces from the exterior vertices to the nodes within each region. Using three force components at each vertex results in a total of 24 unknown forces. However, the magnitude of each force depends on its perpendicular distance (or

lever arm) to the centroid. For example, the y-direction forces at vertices ❶ and ❺ are the same distance from the centroid, in the x-z plane; consequently, any node located along a line joining these two vertices will have the same y-component of force. Since the y-direction forces at the two vertices are equal ($F_{1Y} = F_{5Y}$), one unknown force component may be eliminated. The total number of unknown forces may be reduced to 12 by applying the same approach at the other vertices and in the other two global directions.
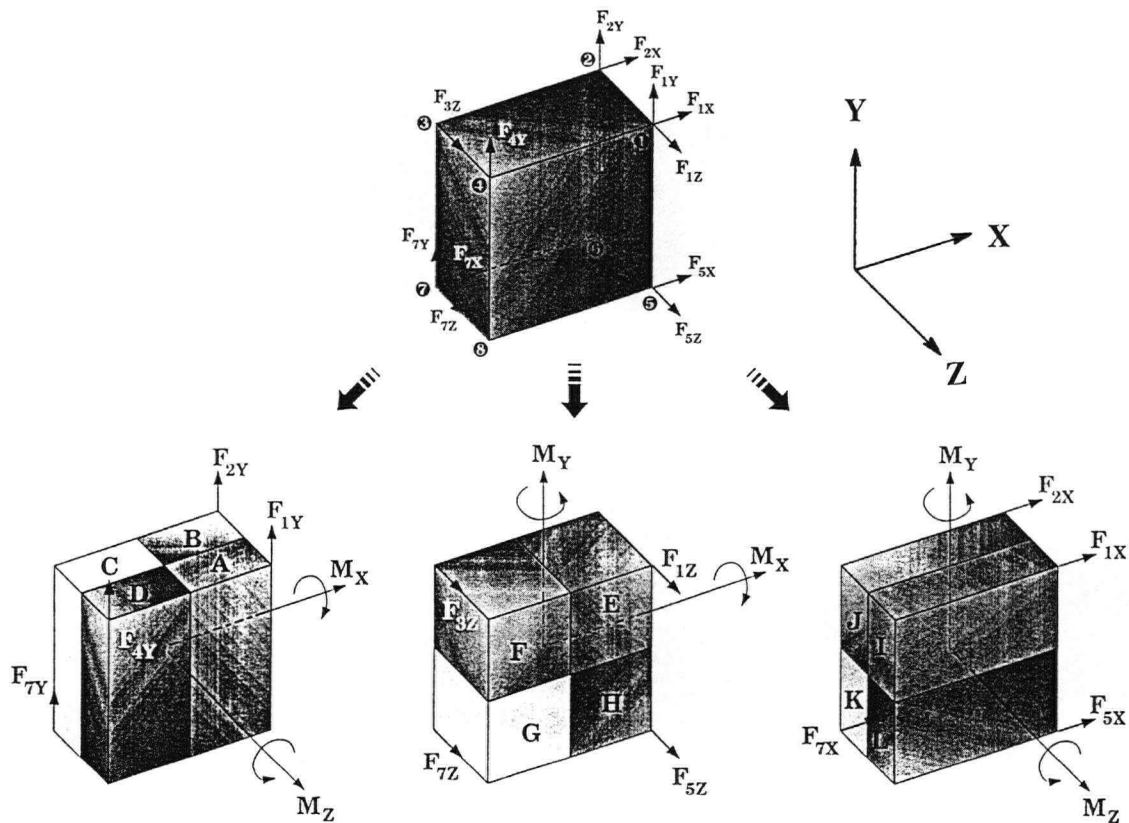
Figure 3.3 **Typical Bounding Box and Force Determination Regions**

Step 4   The length vector joining each node to the centroid of the bounding box may be separated into three components. This effectively creates one moment arm about each of the three global axes for each nodal point. Each node is then assigned three factors (ranging from 0 to 1) according to the ratios of its respective moment arms relative to the maximum moment arms achievable at the vertex of each region.

Step 5   Once the factors for each node have been obtained, an ***effective moment arm length*** is calculated for each of the 12 unknown forces. For example, the effective moment arm length about the z-axis for force F_{1Y} in region **A**, denoted L_z^A is:

$$L_z^A = \sum_{i=1}^{n_A}\left\{factor_{xz}^{(i)} * l_z^{(i)}\right\} \tag{3.9}$$

where $factor_{xz}^{(i)}$ is the moment arm factor in the x-z plane and $l_z^{(i)} = ABS\left(z_b^{(i)} - z_b^c\right)$ is the length of the moment arm about the z-axis of the ith node. The product is summed over n_A nodes in region **A**.

Step 6   Using the effective moment arms determined in the previous step, equations may then be developed for the moments generated about the global axes due to the nodal forces in each region. Continuing with the example from step 5, the global moment about the z-axis due to y-direction nodal forces in region **A**, denoted M_z^A is:

$$M_z^A = F_{1Y} * L_z^A \tag{3.10}$$

Step 7   A total of six equilibrium equations (i.e. three force and three moment) may be written for the 12 unknown forces. Each moment equation was then separated into two equations according to the direction of the forces that were generating the moment. For example, the total moment equation about the z-axis was divided into separate equations for the x- and y-direction forces. The effective moment arms were then compared and a ratio calculated for each pair of equations. The strategy here was to distribute a greater percentage of the load to those regions more capable of generating a moment. This was accomplished by introducing a constraint equation for each pair of moment equations.

Step 8   The procedure outlined in steps 1 through 7 produces a system of equations consisting of six independent equilibrium equations and three additional constraint equations in the 12 unknown forces. This system of equations was solved numerically using an optimization routine called the Constrained Steepest Descent (CSD) method. The entire CSD routine was incorporated into the nodal force

boundary condition (NFBC) program. The unknown forces at the vertices of the bounding box were minimized according to the following objective function:

$$f = \sum_{j=1}^{12} \left\{ \left(ABS(F_j) - g(j) * f_{ave} \right)^2 \right\} \tag{3.11}$$

where $g(j)$ is a function of the mesh density and moment arms in each region, and f_{ave} is the average value of the vertex forces calculated from the previous iteration.

Step 9   The final step in the procedure is to transfer the forces from the vertices to the nodal points inside each region. This was accomplished by multiplying the force components at each vertex by the appropriate moment arm factor for the nodes within the respective region. For example, a node in region **A** would be assigned a percentage of F_{1Y} depending on its moment arm factor in the x-z plane. The same node may also be located in region **E**, in which case it would be assigned a percentage of F_{1Z} depending on its moment arm factor in the x-y plane.

3.3   Numerical Examples

3.3.1 Introduction

The following two sections demonstrate the proposed sub-modeling procedure. The nodal force boundary condition (NFBC) program is used to determine the appropriate boundary conditions for two different sub-models of the core pipe disc filter. In the first example, the boundary conditions are transferred from a five-ring shell element model of the core pipe to a sub-model with the same element topology. In fact, the sub-model was extracted directly from the original five-ring model. This example serves to illustrate the steps involved in the sub-modeling procedure. Since the only difference between the sub-model and the corresponding region in the full model is the calculated boundary condition, numerical results from the two models may be compared to demonstrate the effectiveness of the nodal force boundary condition routine. In the second example, the true motivation for

the development of the program is revealed when the boundary conditions from an updated (i.e. new design) five-ring shell element model are transferred to a solid element sub-model.

In both examples, the numerical model geometries are first presented to illustrate the finite element meshes used in the subsequent analyses. Next, the necessary steps involved in the proposed sub-modeling procedure are described with specific reference to the example cases. Numerical results are presented in terms of von-Mises and alternating stress (S_{zz}) contour plots for both the full model and respective sub-models.

3.3.2 Shell Element Sub-Modeling Example

In this first example, the original disc filter core pipe with five-rings is referred to as the *full* model. The finite element mesh, consisting of 10,269 four-noded, linear shell elements connected by 9,108 nodes, is shown in *Figure 3.4*. Note that end boundary conditions, reaction forces from the disc filter segments, and other applied loads are not illustrated in the figure for clarity of the finite element mesh. As already mentioned, the *final* sub-model is a sub-region of the five-ring model constructed by simply extracting a meshed region of approximately 1,800 shell elements from the top or compressive side of the full core pipe model. The resulting finite element mesh, for which new force boundary conditions will be determined, is shown in *Figure 3.5 (a)*. In the proposed sub-modeling procedure, it is also necessary to extract that portion of the full model which directly corresponds to the geometry of the final sub-model. This creates a mesh for what is called the *displacement* sub-model, as shown in *Figure 3.5 (b)*. In this particular example, the finite element meshes of the respective sub-models are identical since the same method was employed to create both sub-models. In practical sub-modeling situations, the final sub-model will always be more
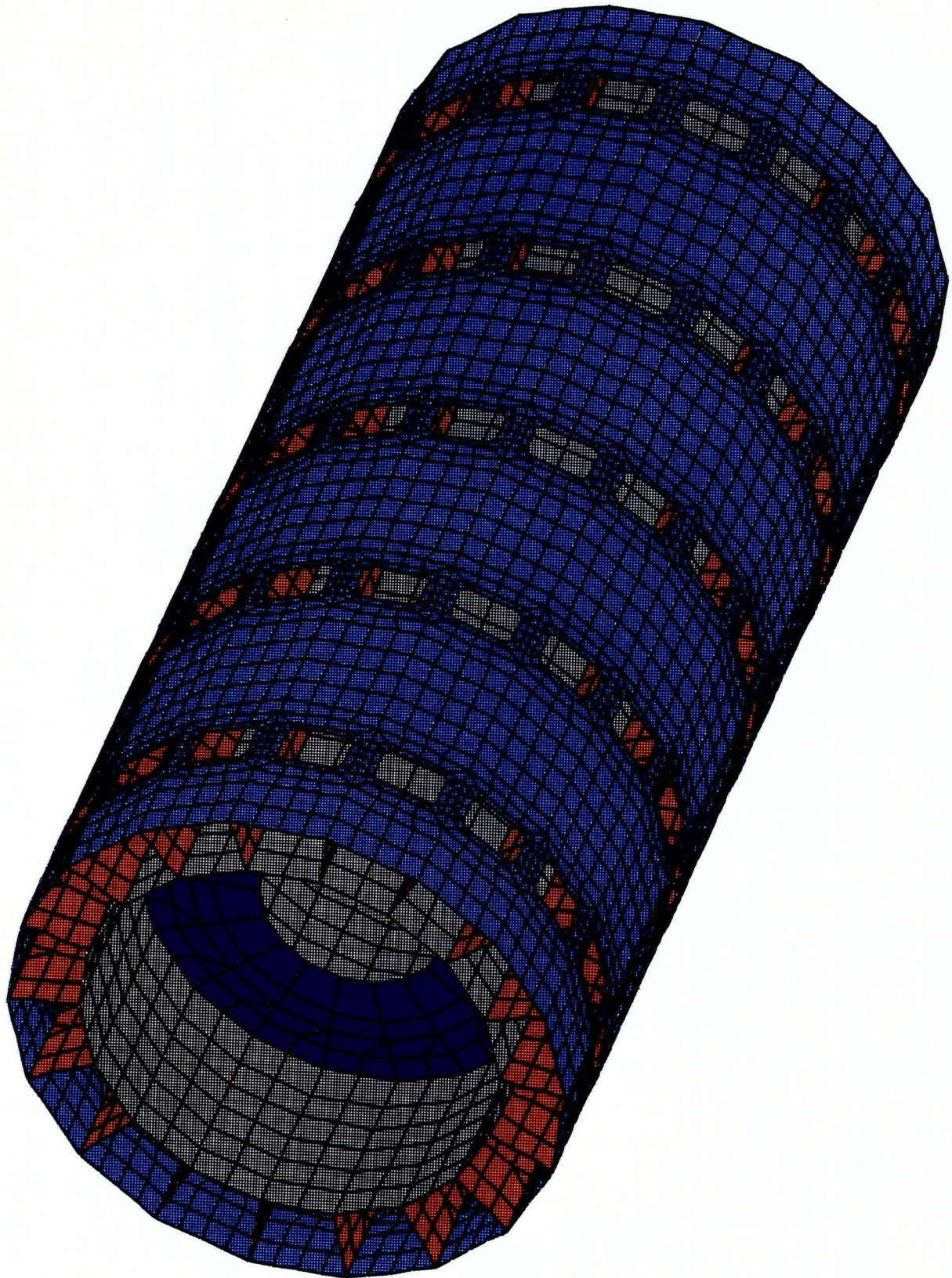
Figure 3.4 **Original Disc Filter Core Pipe (Five-Ring Model)**
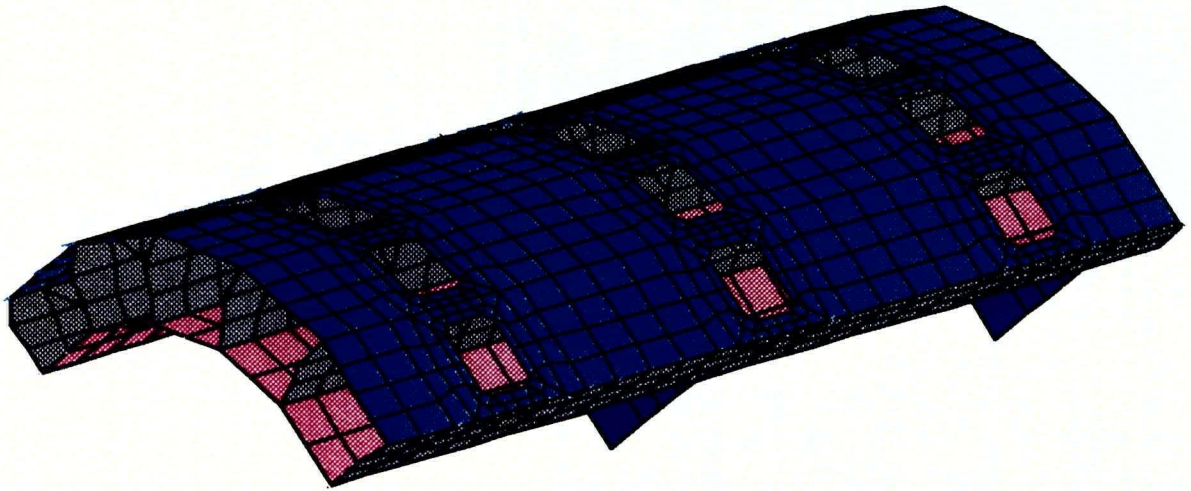
Figure 3.5 (a) **Finite Element Mesh of the *Final* Sub-Model**
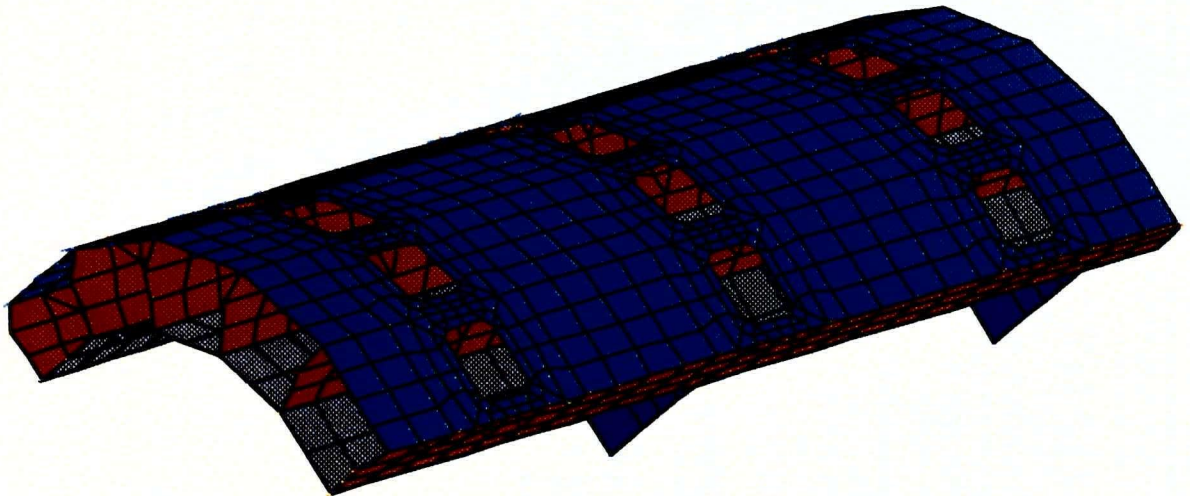
Figure 3.5 (b) **Finite Element Mesh of the *Displacement* Sub-Model**
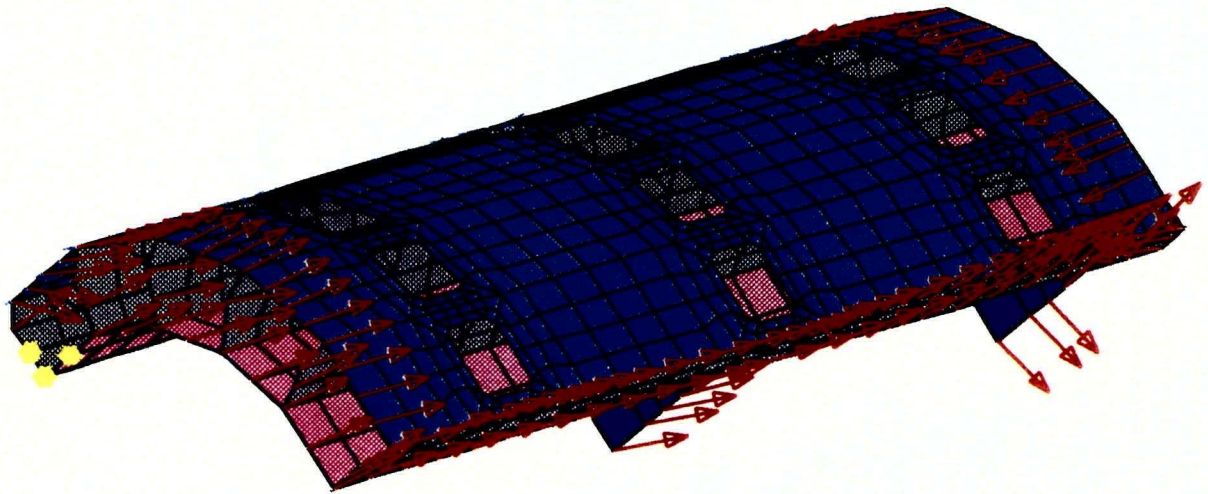
Figure 3.6 (a) *Final* **Sub-Model with Nodal Force Boundary Condition**
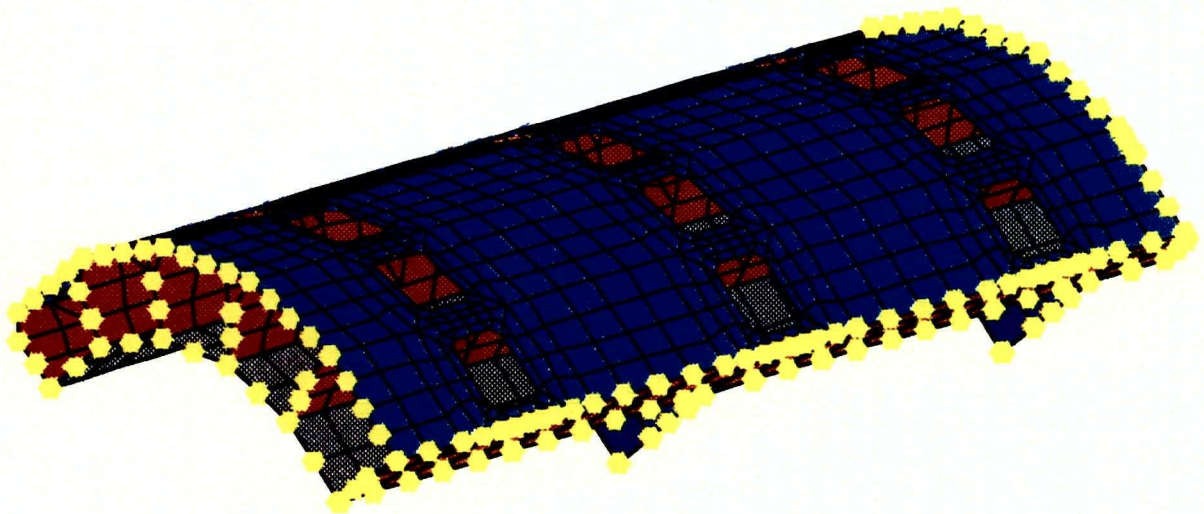
Figure 3.6 (b) *Displacement* **Sub-Model with Displacement Boundary Condition**

refined than the displacement sub-model. The final sub-model may also be constructed from solid elements as opposed to shell or two-dimensional elements and may employ higher order elements than those used in the full model. This sub-modeling example serves to assess the accuracy with which the boundary conditions were transferred to the final sub-model.

As illustrated in *Figure 3.7*, the proposed sub-modeling procedure using the nodal force boundary condition program may be separated into the following four steps:

Step 1   The full five-ring numerical model of the disc filter core pipe was submitted to the EMRC's NISA II [17] solver to determine the displacement solution for every node in the structure. The DISPLAY III [18] pre/post-processor was then used to prepare the resulting von-Mises and alternating (S_{zz}) stress contour plots that will later be compared to the sub-model results.

Step 2   Before the displacement sub-model could be submitted to the solver, it was necessary to impose a displacement constraint on each boundary node equal to the respective nodal displacement solution determined from the full model analysis. *Figure 3.6 (b)* illustrates the displacement constraints that were applied to the sub-model. The displacement sub-model was then submitted to the NISA II solver to determine the nodal reaction forces and moments corresponding to each boundary node where a displacement constraint was specified.

Step 3   The data files required by the nodal force boundary condition program were then prepared. A separate data file was needed for each cutting plane on the displacement sub-model. Four cutting planes were used in the current example. Each data file consists of the nodal coordinates and reaction forces and moments for all the boundary nodes on a single cutting plane. These values were taken from the NISA output file obtained in the previous step. Each data file also contains the nodal coordinates for those nodes on the corresponding cutting plane in the final sub-model. The nodal force boundary condition program was then used to determine the unknown boundary conditions. This produced four separate output

Step 1:

Step 2:

Step 3:

Step 4:

Data File

Displacement Sub-Model:
- ❖ Nodal Coordinates
- ❖ Reaction Forces & Moments

Final Sub-Model:
- ❖ New Sub-Model Nodal Coordinates

Note: Performed separately for each cutting plane

Nodal Force Boundary Condition Program

Output File

Final Sub-Model:
- ❖ New Sub-Model Computed Nodal Forces
- ❖ Session File Compatible

NISA II

NISA II

NISA II

Full Model Results: Displacement Solution Stress Contour Plots

Final Sub-Model Results: Stress Contour Plots

Figure 3.7 **Proposed Sub-Modeling Procedure**

files which together contain the computed nodal forces for all the boundary nodes in the final sub-model. When applied to the boundary, these forces will produce the same global effect as the elements adjacent to the cutting planes and thus simulate the remaining portion of the original structure.

Step 4 The output files prepared in the previous step are compatible with the NISA session file format; therefore, the four files in this example were read directly by NISA's Display III pre/post-processor which transferred the computed nodal forces to the boundary nodes in the final sub-model. The forces at three arbitrary boundary nodes were then replaced by a fixed displacement constraint to eliminate any rigid body rotation. The final sub-model with the calculated nodal force boundary conditions and fixed displacement constraint is shown in *Figure 3.6 (a)*. The numerical model was then submitted to the NISA II solver to determine the displacement solution. The DISPLAY III pre/post-processor was then used to prepare the resulting von-Mises and alternating (S_{zz}) stress contour plots. These results are later compared to the corresponding results for the full five-ring model of the core pipe.

The objective of this four step procedure is to simulate the remaining portion of the original structure by imposing an appropriate set of nodal forces along the boundaries of the final sub-model. The nodal forces generate a resultant force and moment on each cutting plane that would be equivalent to the resultants generated by the original structure. It is important to note that equilibrium is only satisfied globally on each cutting plane and not on a local element level. As a consequence, elements on or near the boundaries of the sub-model may not render accurate numerical results and, therefore, should not be included in any subsequent design analysis. These local inaccuracies diminish quite rapidly, as can be seen from the von-Mises stress contour plot in *Figure 3.8*, so that satisfactory results are usually obtained for a large percentage of the sub-model.
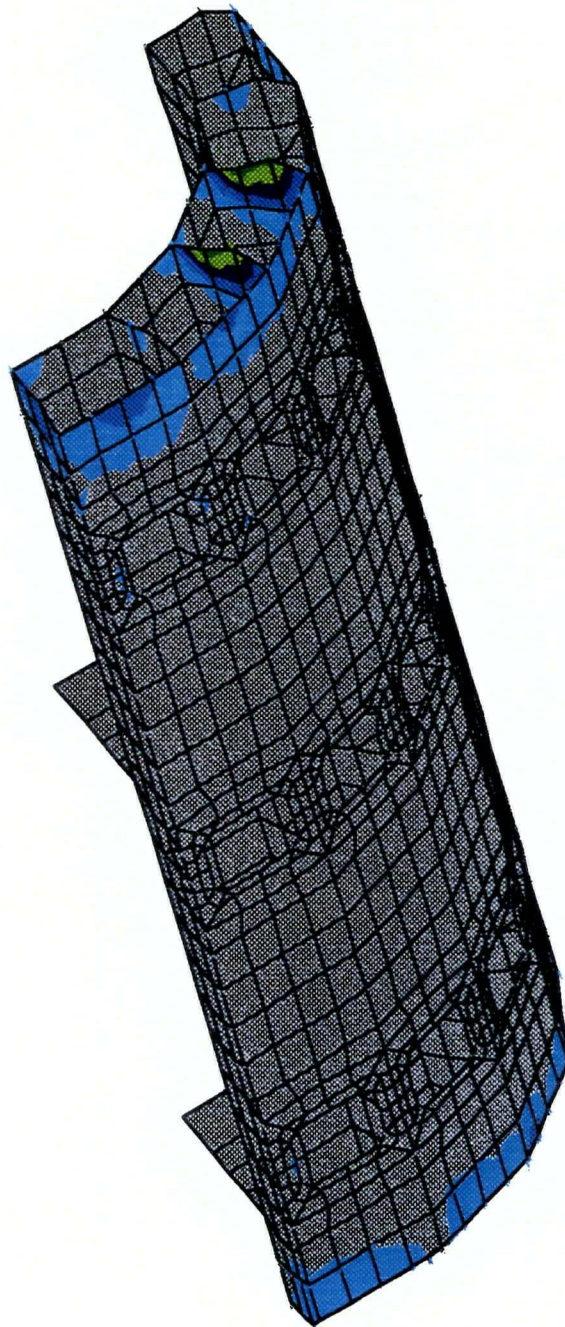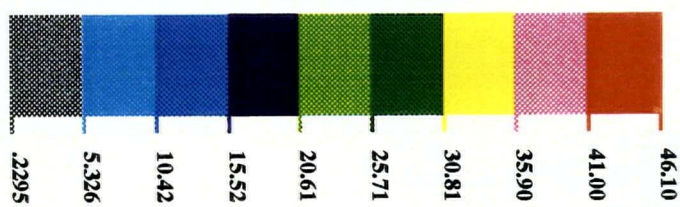
Figure 3.8 **Von-Mises Stress Contour Plot Showing Local Inaccuracies**

To illustrate the typical level of accuracy that may be achieved, a region from the center of the final sub-model was selected and the stress results compared to the corresponding region in the original full five-ring model. The von-Mises stress contours determined from the full model and final sub-model are shown in *Figure 3.9 (a)* and *(b)*, respectively. It is clearly evident that both models exhibit the same stress pattern around the openings for the filter segments, and the range of stress values is also very similar. The maximum von-Mises stress, which is located in diagonal corners of the openings, is 5.1 ksi for the full model and 4.8 ksi for the sub-model, a difference of less than 6 %. The alternating stress (S_{zz}) contours for the full model and final sub-model are shown in *Figure 3.10 (a)* and *(b)*, respectively. Again, both models exhibit a similar stress pattern around the openings in the outer shell. The maximum compressive alternating stress is located in diagonal corners of the openings and has a value of -5.1 ksi in the full model and -4.9 ksi in the final sub-model. The difference in these two stress values is about 4 %.

This first example illustrates that accurate results may be obtained for finite element sub-models using an imposed nodal force approach to determine the unknown boundary conditions. The four main steps involved in the proposed sub-modeling technique have been outlined, and a sub-modeling example has been presented to illustrate the procedure. In the final section of this chapter, a second example is used to demonstrate the full capabilities of the developed program thus revealing the main advantages of this sub-modeling technique. This example is much more significant from the practical point of view, since the appropriate boundary conditions for a solid element sub-model are determined directly from a shell element model.
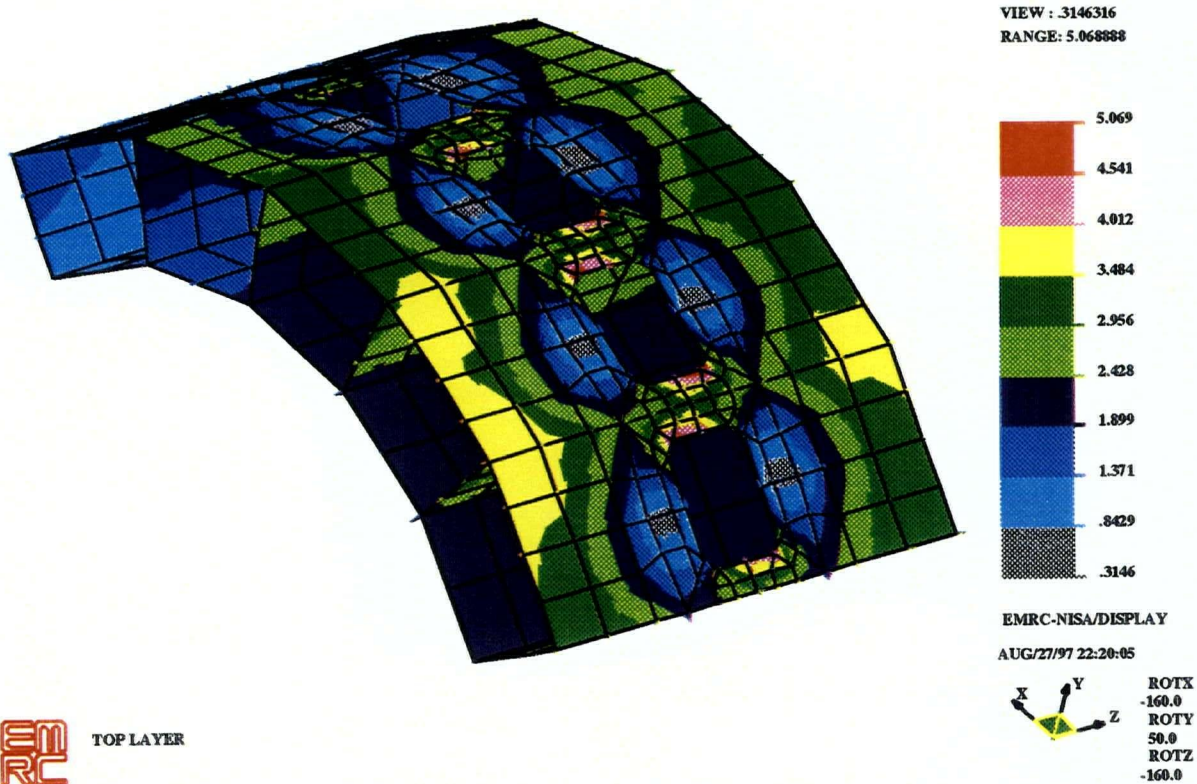
Figure 3.9 (a) **Von-Mises Stress Contours - Full Model**
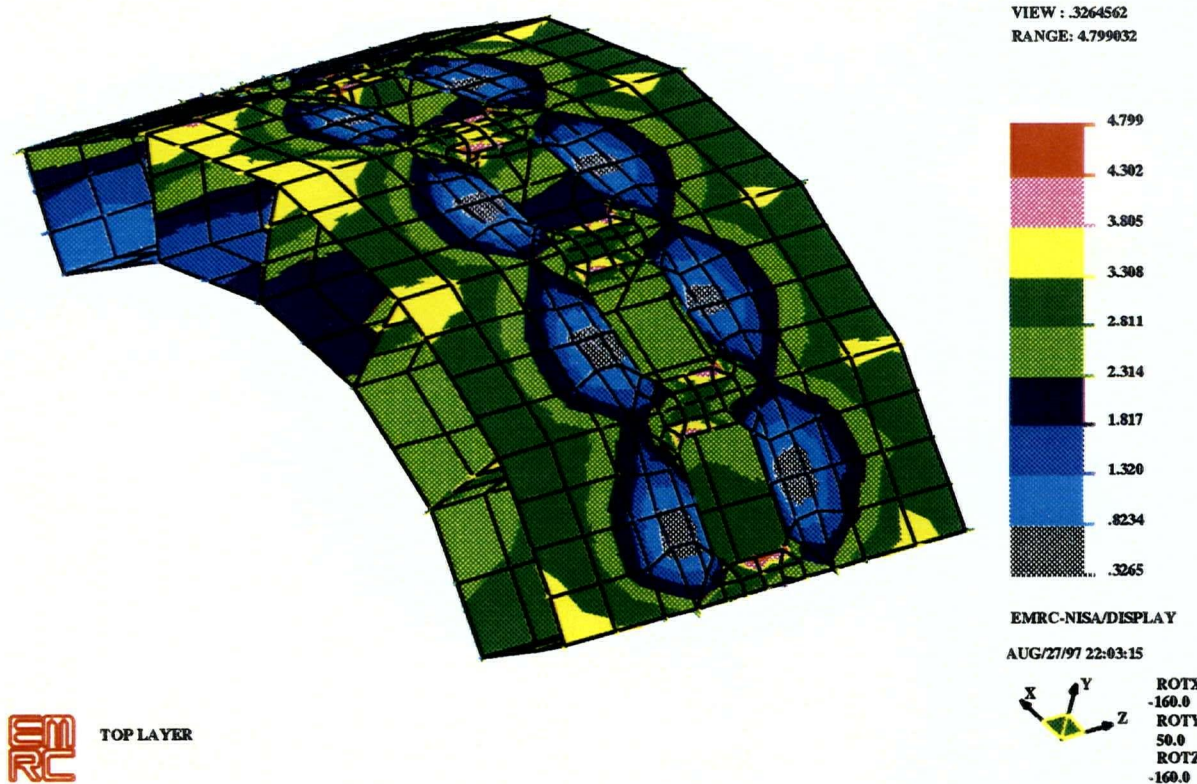
Figure 3.9 (b) **Von-Mises Stress Contours - Final Sub-Model**
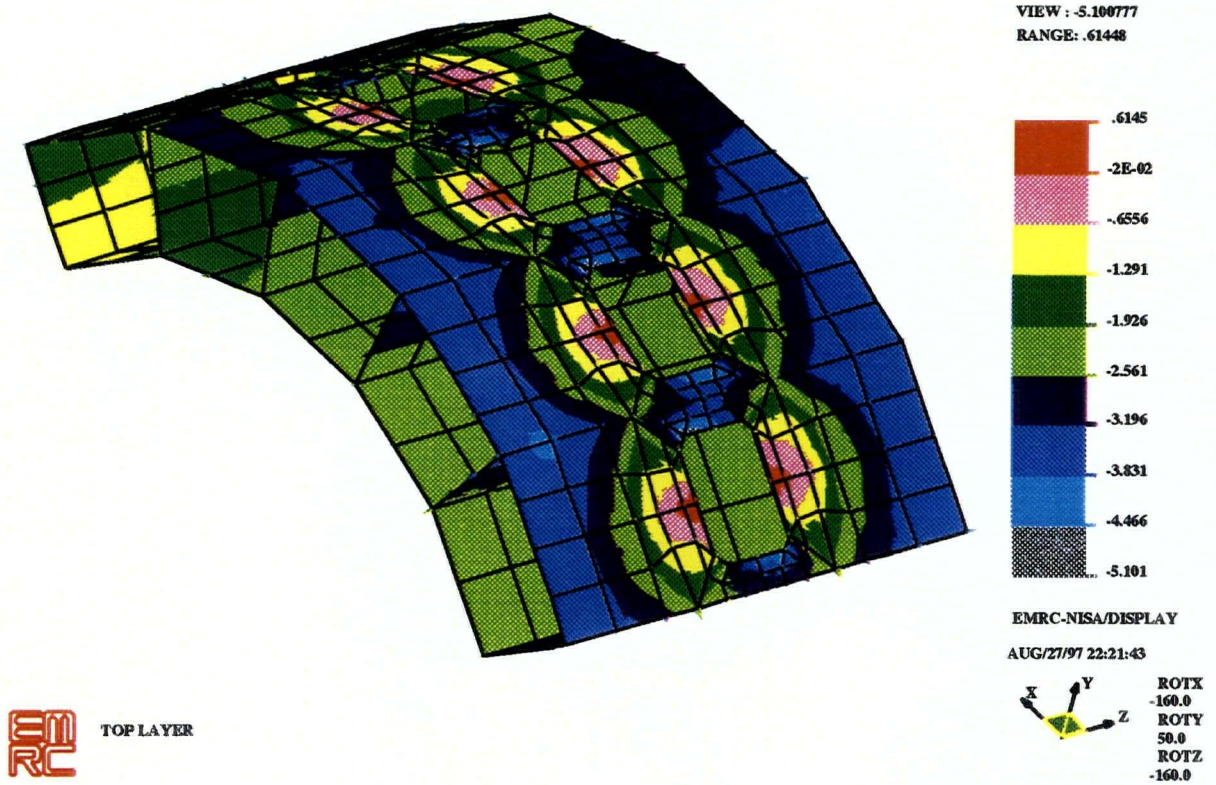
Figure 3.10 (a) **Alternating Stress Contours - Full Model**
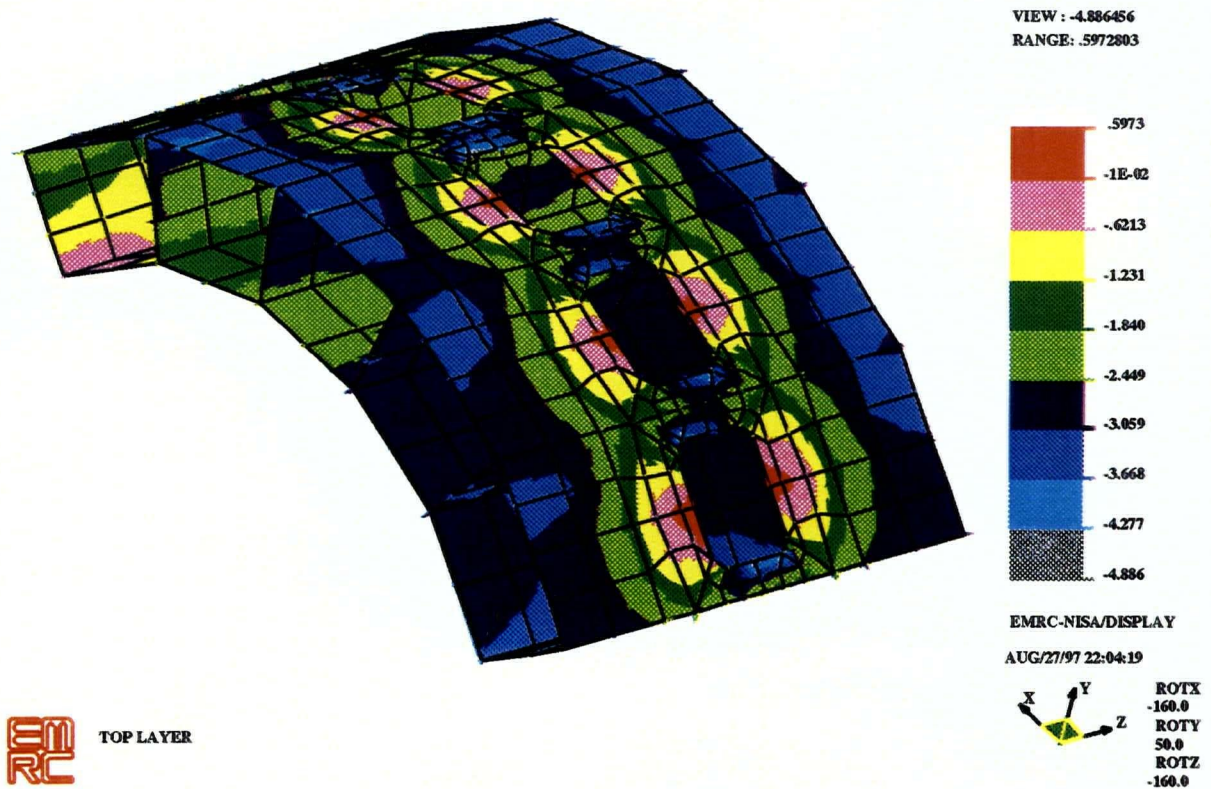
Figure 3.10 (b) **Alternating Stress Contours - Final Sub-Model**

3.3.3 Solid Element Sub-Modeling Example

An updated five-ring finite element model of the new disc filter core pipe design was used as the full model in this example. The finite element mesh, which consists of 10,929 four-noded, linear shell elements connected by 9,666 nodes, is shown in *Figure 3.11*. The final sub-model, for which the boundary conditions will be determined, consists of 4,756 non-linear solid elements (20-noded brick and 15-noded wedge elements) connected by 27,889 nodes. As a matter of interest, this particular sub-model, which is illustrated in *Figure 3.12 (a)*, was used to determine the appropriate stitch and plug weld configurations for the new core pipe design in a separate project [88]. For this application, it was necessary to model the region of maximum tensile stress, so the final sub-model represents a portion of the geometry taken from the lower or tensile region of the full model. Again, the displacement sub-model is the region in the full model which corresponds to the geometry of the final sub-model. In this case, the displacement sub-model consists of only 386 four-noded, linear shell elements and 392 nodes, as shown in *Figure 3.12 (b)*. Contrary to the first example, the displacement sub-model is markedly different from the final sub-model as will normally be the case in practice. Solid elements were chosen to accurately model the stitch weld geometry, and non-linear elements were required to correctly represent the bending effects in the inner and outer plates. The solid element sub-model also contains more than 12 times more elements and about 71 times more nodes than the displacement sub-model. In fact, the final solid element sub-model represents only 5 % of the full model geometry but contains almost half as many elements and almost three times as many nodes as the full five-ring model. The same four step procedure described in the previous section was used to determine the boundary conditions for the final solid element sub-model.
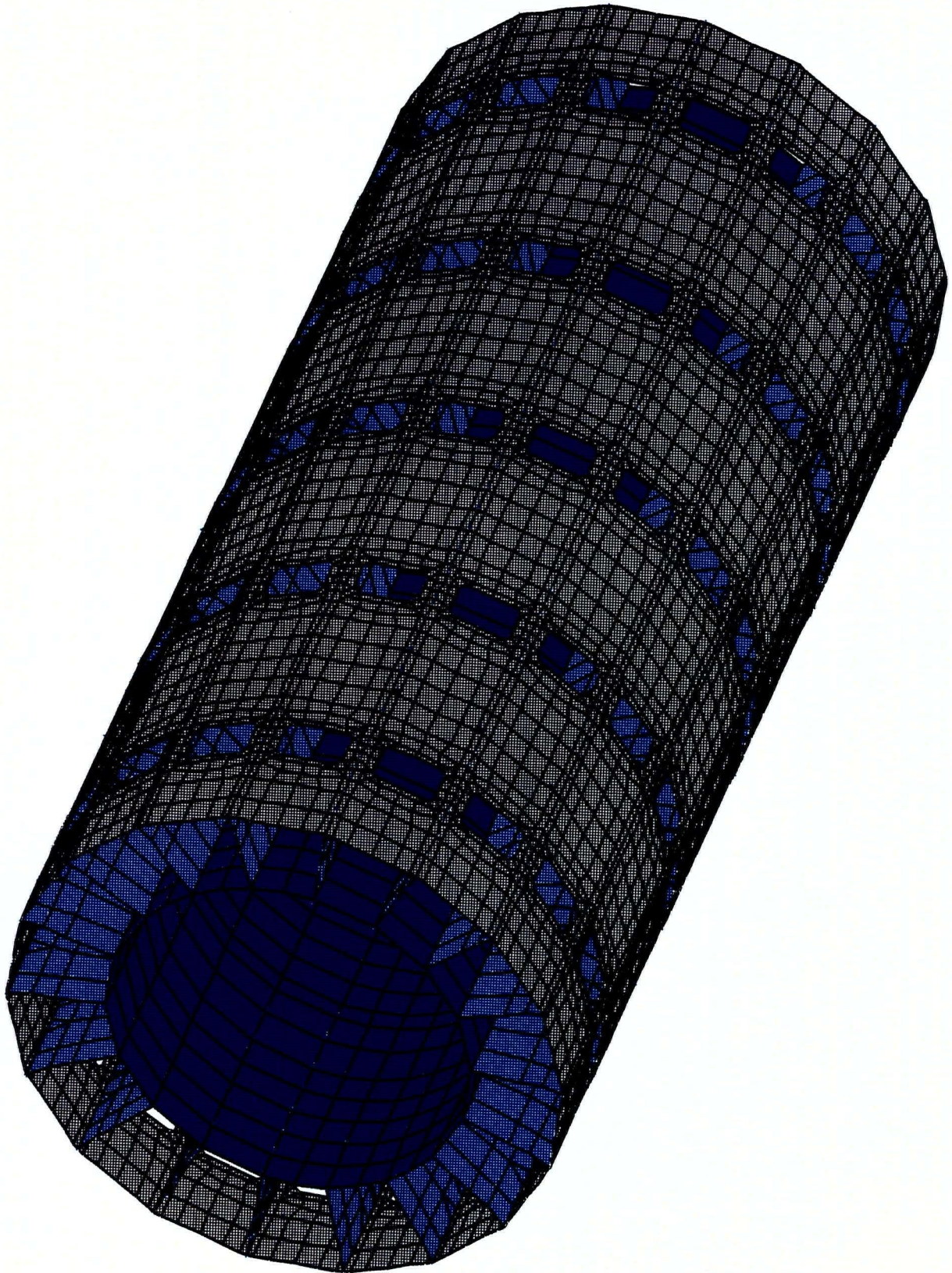
Figure 3.11 **Finite Element Model of the New Core Pipe Design**
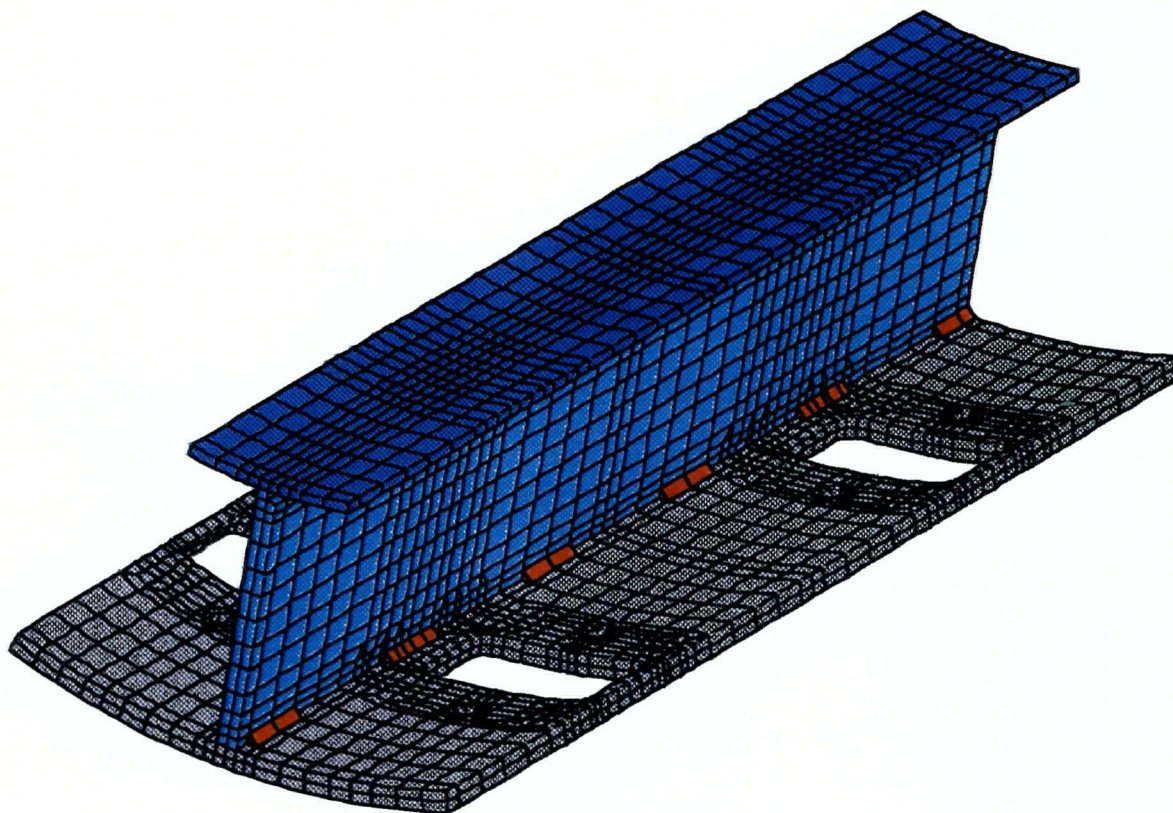
Figure 3.12 (a) **Finite Element Mesh of the Solid Element Sub-Model**
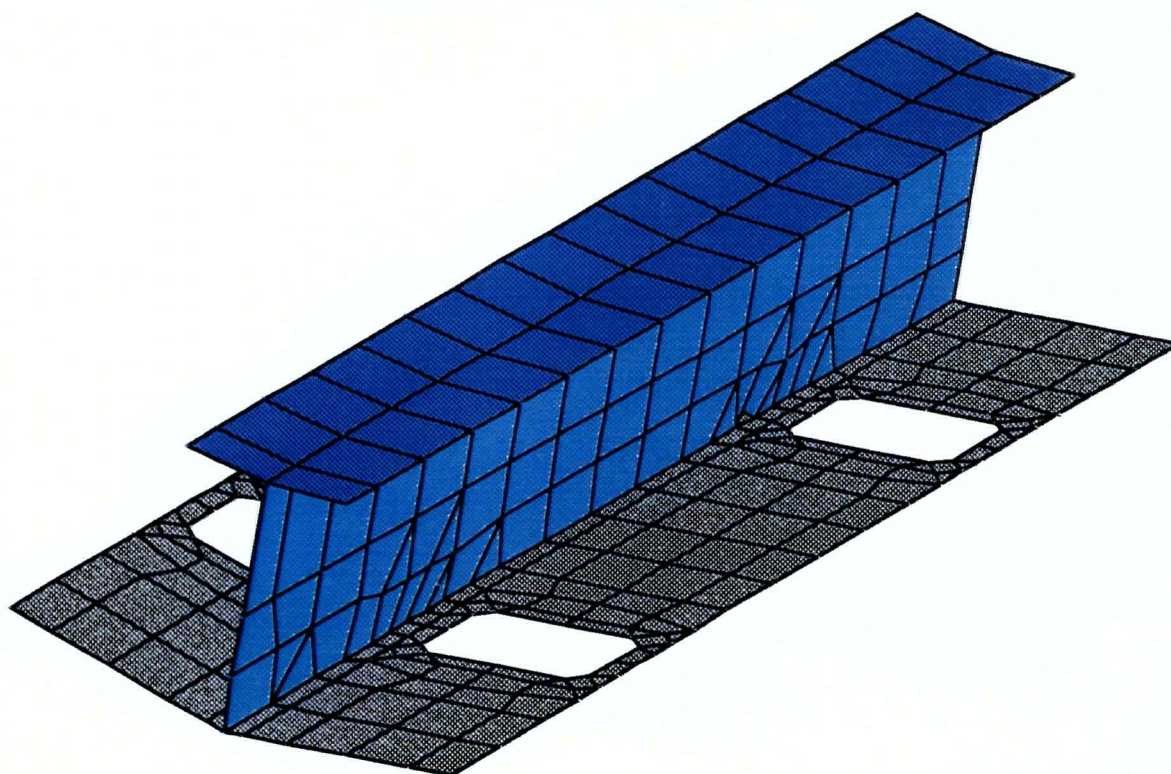
Figure 3.12 (b) **Finite Element Mesh of the Displacement Sub-Model**

The same four step procedure described in the previous section was used to determine the boundary conditions for the final solid element sub-model. The first step was to obtain the full model displacement solution using the NISA II solver. Next, the nodal displacement solution was imposed on the boundary nodes in the displacement sub-model. This shell element sub-model was then submitted to the NISA II solver to determine the nodal reaction forces and moments corresponding to each boundary node. The data files for the nodal force boundary condition program were then prepared.

In this example, the longitudinal edges of the inner and outer plates were handled separately thus increasing the number of cutting planes to six. Consequently, six data files were prepared because a single file is required for each cutting plane. A brief discussion is required to explain why six cutting planes were used in the current example while only four were used in the previous analysis.

The solid element sub-model contains several nodes in the thickness direction of the inner and outer plates. It is therefore possible to generate a moment at any location along the edge of either plate by the addition of a force couple. This is not possible when only one node is present in the thickness direction, as was the case in the first example. By separating the inner and outer plate edges into different cutting planes, independent resultant forces and moments may be generated along each edge. If a single cutting plane had been used for both edges, the global force and moment generated by the nodal force boundary condition program would have been distributed over the two edges concurrently. This could possibly lead to inaccurate stress results if one plate carries a much greater percentage of the total load than the other plate during routine operation. A single cutting plane was acceptable in the first example because the region of interest was sufficiently remote from the applied boundary condition. In addition, the shell element sub-model contained a number of vertical division

bars that tied the inner and outer plates together. The interior region of the sub-model was therefore less sensitive to the actual distribution of load on the boundaries. Finally, as the number of cutting planes is increased, the extent of each cutting plane is decreased, resulting in a more accurate transfer of boundary conditions to the final solid element sub-model. The effort expended in preparing a large number of data files becomes the practical limitation on the number of cutting planes used in any particular sub-modeling analysis.

Once all six data files were prepared, the nodal force boundary condition program was used to determine the unknown boundary conditions on each cutting plane. The computed nodal forces were then transferred to the boundary nodes in the final sub-model using NISA's Display III pre/post-processor. The forces at three arbitrary boundary nodes were again replaced by a fixed displacement constraint to eliminate possible rigid body rotation. To complete the final step, the solid element sub-model was submitted to the NISA II solver to determine the displacement solution. The stress results obtained for the solid element sub-model are compared to the full model results below.

The von-Mises stress contours determined from the full model and final sub-model are illustrated in *Figure 3.13 (a)* and *(b)*, respectively, while the alternating stress contours are given in *Figure 3.14 (a)* and *(b)*. In both figures, the stress results have been cropped along the boundaries to remove local inaccuracies that normally occur on the periphery of the final sub-model. Upon initial examination, the stress contours for the two models appear to be quite different. A closer scrutiny reveals that the smaller, non-linear elements used in the solid model have captured the stress raiser at the corners of the openings in the outer plate. The full model of the core pipe, however, did not accurately represent the stress concentration because a single shell element was used to model each corner of the opening. This difference in maximum value makes it difficult to compare the respective stress contours because the

VIEW : .4472307
RANGE: 4.685456

4.685
4.215
3.744
3.273
2.802
2.331
1.860
1.389
.9181
.4472

EMRC-NISA/DISPLAY

AUG/28/97 01:26:35
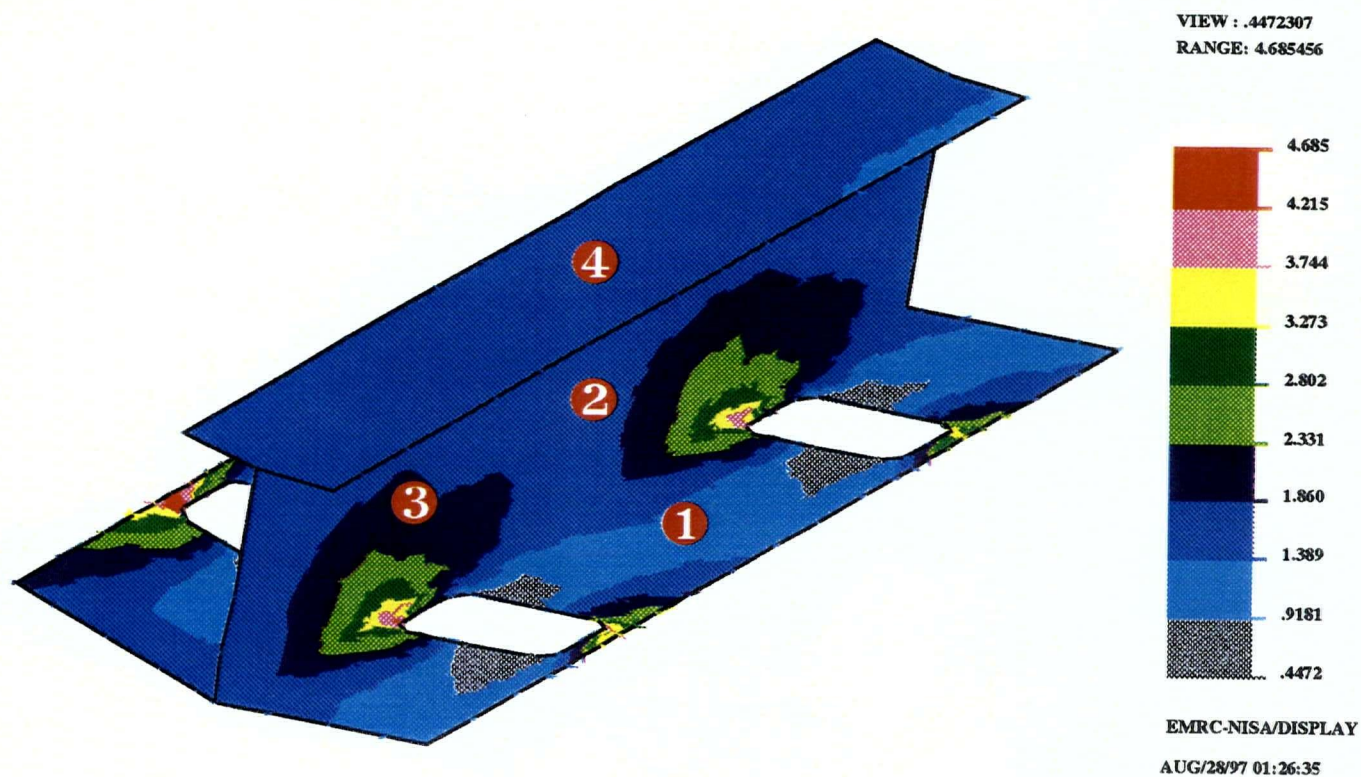
Figure 3.13 (a) **Von-Mises Stress Contours - Full Model (Shell Elements)**

VIEW : .0349456
RANGE: 18.42509

18.43
16.38
14.34
12.30
10.25
8.208
6.165
4.122
2.078
3E-02

EMRC-NISA/DISPLAY

AUG/28/97 00:45:33
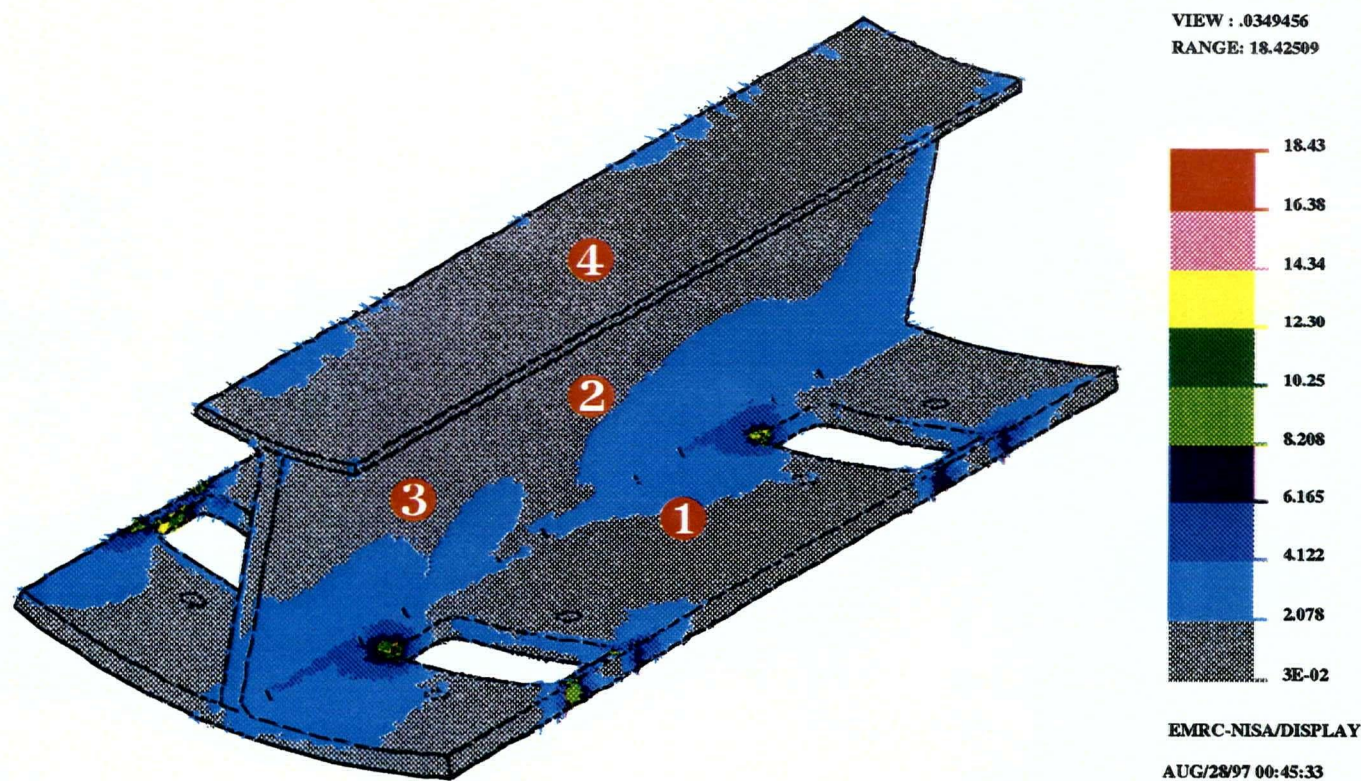
Figure 3.13 (b) **Von-Mises Stress Contours - Final Sub-Model (Solid Elements)**

VIEW : -.2360149
RANGE: 4.592862

4.593
4.056
3.520
2.983
2.447
1.910
1.374
.8371
.3005
-.2360

EMRC-NISA/DISPLAY
AUG/28/97 01:26:57
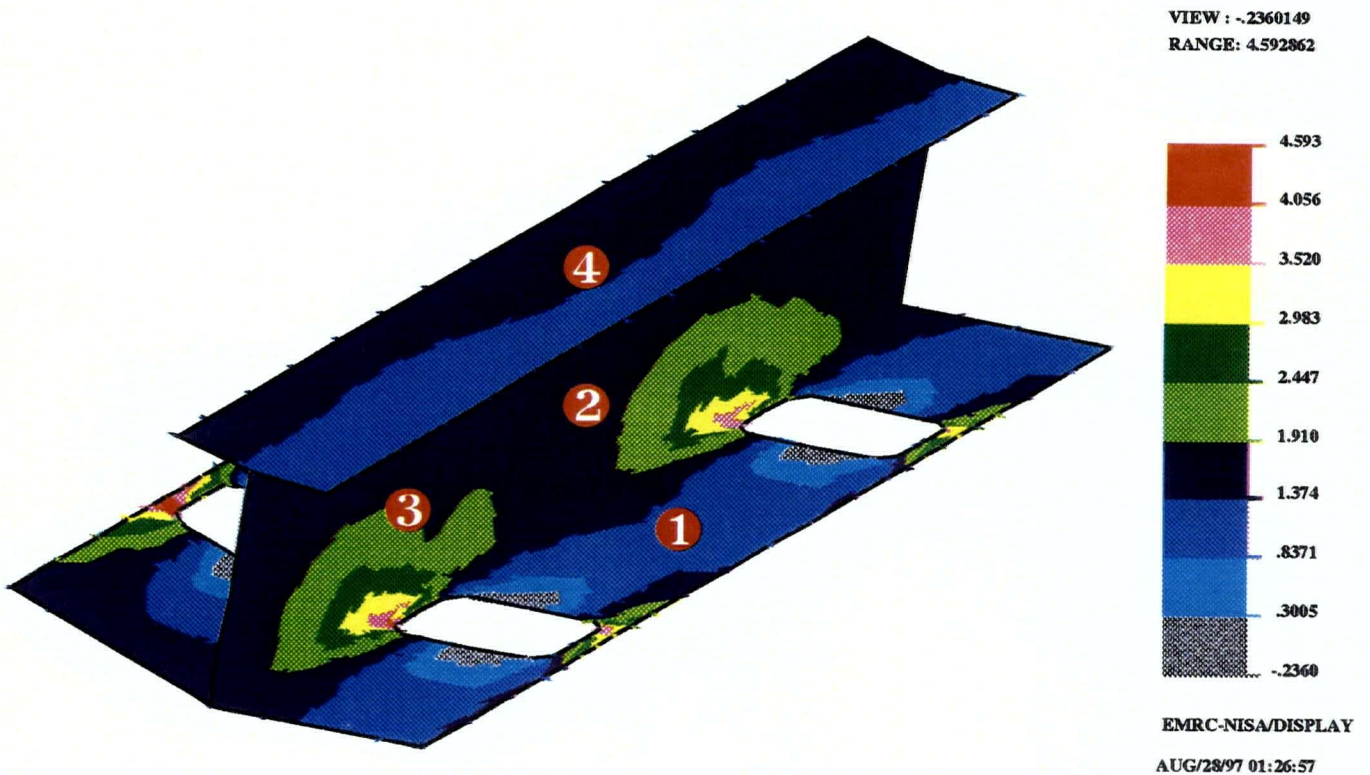
Figure 3.14 (a) **Alternating Stress Contours - Full Model (Shell Elements)**

VIEW : -4.427711
RANGE: 16.5095

16.51
14.18
11.86
9.530
7.204
4.878
2.551
.2250
-2.101
-4.428

EMRC-NISA/DISPLAY
AUG/28/97 00:47:12
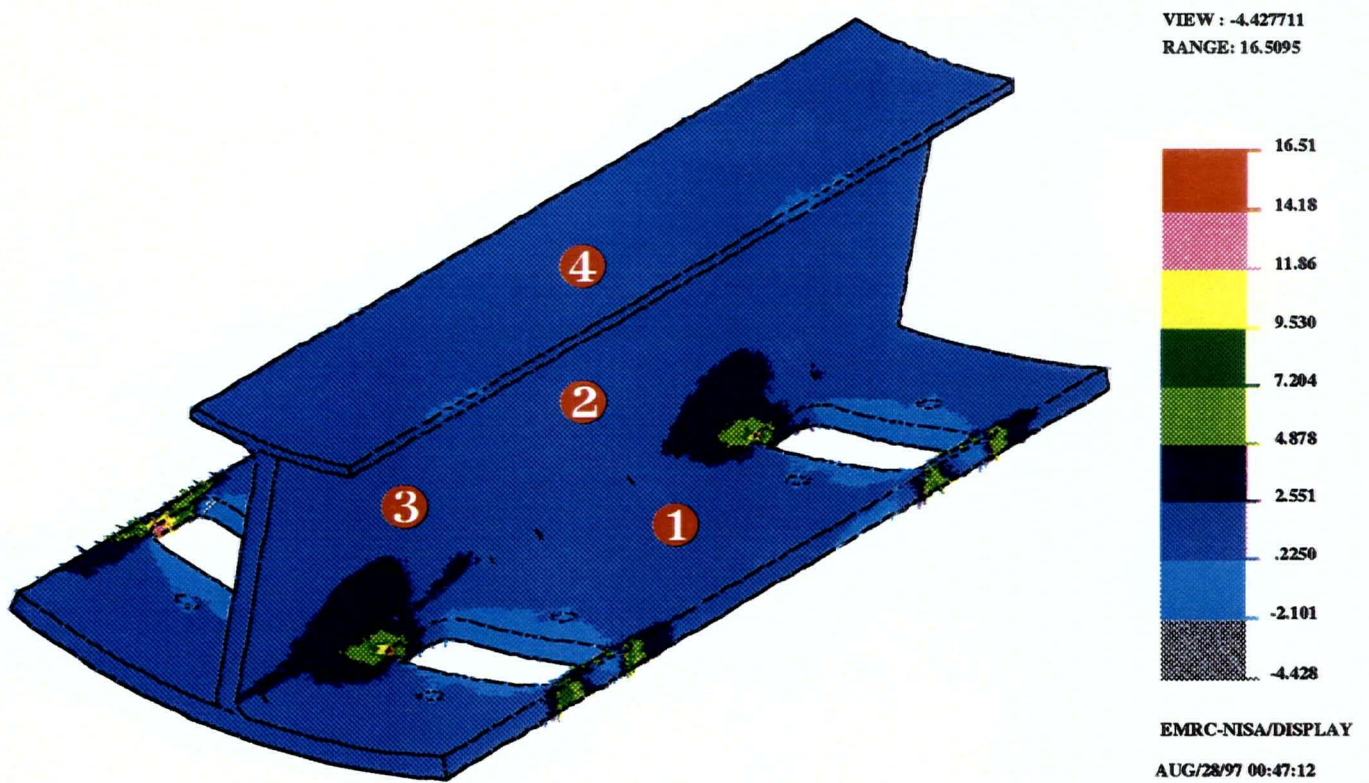
Figure 3.14 (b) **Alternating Stress Contours - Final Sub-Model (Solid Elements)**

range of stress represented by each contour band is different for the two models.

Von-Mises and alternating stress values were therefore obtained at four positions remote from the stress concentration, as indicated in *Figures 3.13* and *3.14*. The resulting values are compared in *Table 3.1*. At the four positions considered, the maximum absolute difference between the solid sub-model result and that obtained from the full model was approximately 0.1 ksi. The largest percent difference, occurring at the position on the outer plate, was found to be about 7 % for the von-Mises stress and 8 % for the alternating stress component. These results are extremely favorable considering the differences in element size, type and order used in the solid element sub-model compared to those used in the full model. This example clearly demonstrates the successful implementation of the nodal force boundary condition program. More importantly, it illustrates an alternative approach to finite element sub-modeling which eliminates the need for transition elements and local mesh refinement. In fact, the only demand this technique places on the finite element model is that the geometry of the sub-model can be approximated by a meshed region in the full model.

Table 3.1 **Stress Values at Four Positions on the Core Pipe**

Position	Finite Element Model	Von-Mises Stress (ksi)	Alternating Stress (ksi)
1	Full Model (shell elements)	1.4	1.3
	Sub-Model (solid elements)	1.5	1.2
	Percent Difference	7 %	- 8 %
2	Full Model	1.8	1.7
	Sub-Model	1.9	1.8
	Percent Difference	6 %	6 %
3	Full Model	1.9	1.9
	Sub-Model	1.8	1.9
	Percent Difference	5 %	0 %
4	Full Model	1.5	1.5
	Sub-Model	1.5	1.5
	Percent Difference	0 %	0 %

CHAPTER 4

FATIGUE OF WELDED JOINTS

4.1   Background and Literature Review

4.1.1 Welding Induced Residual Stress

The distribution of residual stresses in welded plates has been widely investigated for many years. A schematic representation of the changes in temperature and longitudinal stresses during welding is illustrated in *Figure 4.1* [19]. A section of material in the vicinity of the weld experiences different rates of expansion and contraction compared with other sections of the weldment. Prior to welding (section **A-A**), the plates are assumed to be at a uniform temperature and in a relatively stress free condition. As the welding arc approaches (section **B-B**), the temperature increases rapidly, and the material begins to expand. This initial expansion is restrained by cooler material further away from the heat source, which generates compressive residual stresses in the section. At some critical temperature, the flow stress of the section is exceeded in the Weld Bead (WB) and Heat Affected Zone (HAZ), and further heating results in a decline in stress as the metal becomes softer. As the welding arc passes (section **C-C**), the temperature of the section decreases causing a reversal of the plastic strains in the WB/HAZ region from compressive to tensile. A lower temperature is then reached at which the section's flow resistance increases, and the section begins to experience tensile stresses in the contracting region of the WB/HAZ, opposed by compressive stresses in the cooler, adjacent material. Further decrease in temperature is then

accommodated by the section in the form of elastic tensile stresses, confined mainly to the

region of the WB/HAZ, until the weldment cools down completely (section **D-D**) [20].
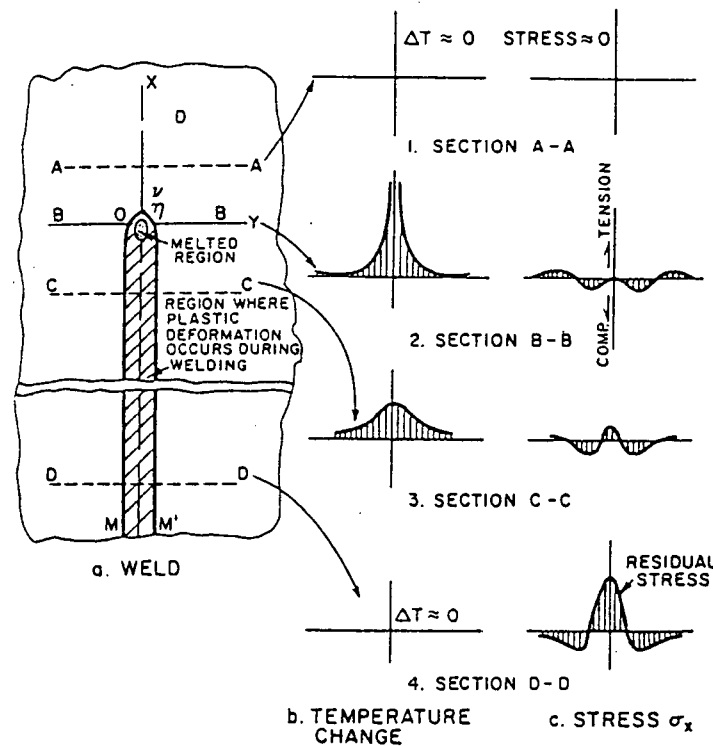
Figure 4.1 **Development of Longitudinal Residual Stresses [20]**

The final distribution of longitudinal residual stress, which acts in the direction of the

weld line, has a maximum value in the center of the weld and decreases from tensile stresses

in the weld bead and heat-affected zone to compressive stresses in the surrounding parent

material so that the resulting distribution will be self-equilibrated. In the case of low carbon

steel welds, the maximum tensile value may be of the same order as the yield strength of the

weld metal depending on the rigidity of the structure and the thickness of the weldment [21].

For a general cross-section taken perpendicular to the weld line, the transverse residual

stress varies symmetrically from tensile stress at the upper and lower surfaces of the plate to a

narrow band of compressive stress in the center part of the plate. The transverse residual

stress profile will change somewhat according to the shape of the weld bead and the number

of passes required for a particular joint thickness. A typical distribution of transverse residual

stress due to welding is shown in *Figure 4.2*. Normally the maximum tensile stress in the

transverse direction is less than about 20 % of the longitudinal stress for unrestrained plates

[22]. In most fabricated structures, however, the degree of restraint may be substantial;

therefore, the maximum tensile value of transverse residual stress will be considerably

higher, possibly as much as 50 % of the yield strength of the weld metal.
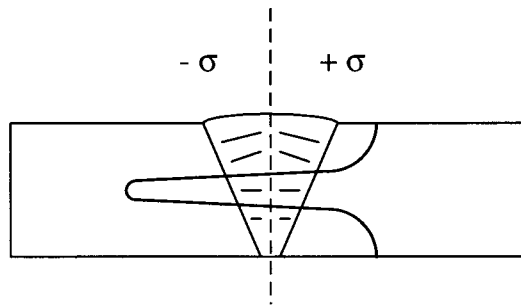
Figure 4.2 **Transverse Residual Stress Distribution [20]**

It is well known that the fatigue life of welded joints is significantly affected by welding

residual stress. Studies of fatigue crack growth in steel weldments have generally shown that

residual stresses are primarily responsible for higher or lower fatigue crack growth rates in

comparison with the base material. Regions of compressive residual stress retard the fatigue

crack growth rate while tensile residual stress regions produce the opposite effect. In studies

of fatigue crack propagation in stress-relieved joints made from structural steels, Maddox

[23] showed that the crack growth rate in the heat-affected zone as well as in the weld metal

is similar to the rate in the base material. Therefore, the magnitude of residual stress has a significant influence on weldment fatigue crack growth rates.

A growing fatigue crack will also generate its own residual stress field resulting from tensile plastic strains, both in front of and in the wake of its tip. The compressive residual stresses left in the wake cause the crack closure phenomenon. A number of researchers [22, 24 - 41] have examined various aspects related to the prediction of fatigue crack growth in residual stress fields both from the theoretical and the experimental points of view. Previous investigations show that the crack growth rates under various stress ratios are equivalent on the basis of Elber's [42] effective stress intensity range which takes into account the effects of crack closure. Although Elber's effect is caused by the remaining cyclic plastic strain on the crack surface, Fukuda and Sugina [38] showed that a similar phenomenon may be observed in welded specimens due to the remaining plastic strain caused by welding. These concepts of crack closure and effective stress intensity range will be explored in more detail in a later section. At this early stage in the discussion, it is sufficient to conclude that residual stress and crack opening behaviors become very important for predicting the fatigue life of welded components.

4.1.2 Introduction to Linear Elastic Fracture Mechanics

For a general crack front in a three dimensional body, the *fracture mode* designates the type of geometric separation. Mode I (opening mode) denotes a symmetric opening where the relative displacements between corresponding pairs are normal to the fracture surface. Modes II (shearing mode) and III (tearing mode) denote antisymmetric separation through

relative tangential displacements, normal and parallel to the crack front, respectively [43].

The three modes of crack tip deformation are illustrated in *Figure 4.3*.

Mode I	Mode II	Mode III
(Opening Mode)	(Shearing Mode)	(Tearing Mode)
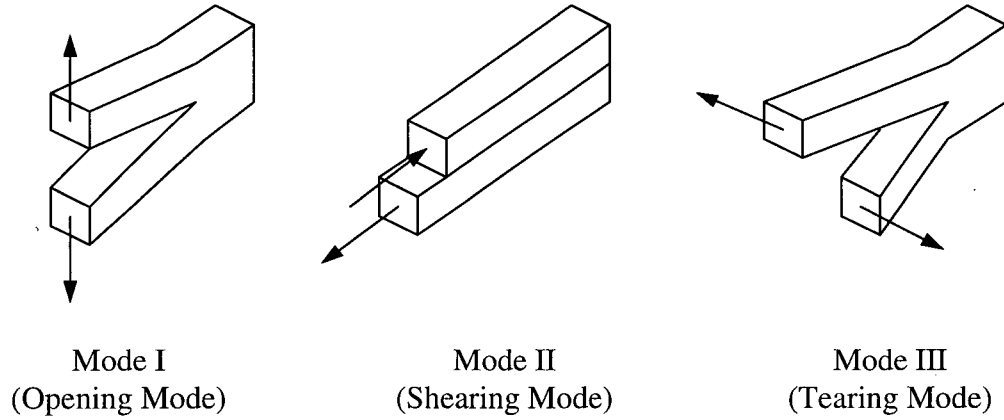
Figure 4.3 **The Three Modes of Fracture [43]**

Classical solutions for the stress and displacement fields around a crack are well known [44, 45]. The stress field surrounding the crack-tip region for a linear elastic material may be expressed in the form:

$$\sigma_{ij} = \frac{K_I}{\sqrt{2\pi r}} g_{ij}^I(\theta) + \frac{K_{II}}{\sqrt{2\pi r}} g_{ij}^{II}(\theta) + \frac{K_{III}}{\sqrt{2\pi r}} g_{ij}^{III}(\theta) \qquad (4.1)$$

where K_I, K_{II}, K_{III} are the stress intensity factors associated with the three modes of fracture, and $g_{ij}(\theta)$ are dimensionless angle-dependent expressions related to the geometry of the structure as well as Poisson's ratio, ν. As seen from this equation, the stress field becomes infinite as $r \rightarrow 0$, and the elastic stress distribution near a crack tip is said to exhibit an inverse square root singularity $(1/\sqrt{r})$. To produce accurate results for the problem of the elastic deformation of a body containing a crack, it is necessary, therefore, to generate a solution which exhibits the same stress (or strain) field singularity.

The near-tip stress and displacement distributions for a symmetric mode I deformation take, explicitly, the form [46]:

$$\begin{Bmatrix} \sigma_{xx} \\ \tau_{xy} \\ \sigma_{yy} \end{Bmatrix} = \frac{K_I}{\sqrt{2\pi r}} \cos(\theta/2) \begin{Bmatrix} 1 - \sin(\theta/2)\sin(3\theta/2) \\ \sin(\theta/2)\cos(3\theta/2) \\ 1 + \sin(\theta/2)\sin(3\theta/2) \end{Bmatrix} \tag{4.2}$$

$$\begin{Bmatrix} u_x \\ u_y \end{Bmatrix} = \frac{K_I}{2G} \sqrt{\frac{r}{2\pi}} \begin{Bmatrix} \cos(\theta/2)[\, \kappa - 1 + 2\sin^2(\theta/2)\,] \\ \sin(\theta/2)[\, \kappa + 1 - 2\cos^2(\theta/2)\,] \end{Bmatrix} \tag{4.3}$$

where G is the elastic shear modulus and $\kappa = (3 - 4\nu)$ for plane strain and $\kappa = (3 - \nu) / (1 + \nu)$ for plane stress, ν being Poisson's ratio. In this notation, tension is applied in the y-direction with the crack lying along $x \leq 0$. The polar coordinates (r, θ) are centered at the crack tip with the crack surfaces lying along $\theta = \pm\,\pi$. The strength of the singularity, K_I, is the prime unknown in any elastic crack analysis.

Of the three fracture modes, the opening mode (mode I) is generally considered to be the most dangerous loading situation since this is usually the dominant mode of deformation contributing to crack growth in metallic materials. The forthcoming discussion, therefore, will be limited to the consideration of mode I problems only, and it is convenient to drop the index I and agree that the notation K refers to mode I unless otherwise stated.

As already mentioned, the Linear Elastic Fracture Mechanics (LEFM) solution for the stress field surrounding a crack predicts infinite stresses at the crack tip. In reality, all materials yield at a finite value of stress, so the LEFM solution loses its validity in the immediate vicinity of the crack tip. However, according to McClintock and Irwin [47], the basic assumptions of fracture mechanics remain valid if yielding is confined to a very small plastic zone at the crack tip surrounded by an elastic region in which the crack tip stress field

is given by equation (4.2). A good estimate for the maximum radius of the plastic zone is given by Broek [48]:

$$r_{max} \approx \frac{1}{2\pi}\left(\frac{K_{max}}{\sigma_{ys}}\right)^2 \qquad \text{for plane stress} \qquad (4.4)$$

$$r_{max} \approx \frac{1}{6\pi}\left(\frac{K_{max}}{\sigma_{ys}}\right)^2 \qquad \text{for plane strain} \qquad (4.5)$$

where K_{max} is the maximum stress intensity factor and σ_{ys} is the yield strength of the material. Strictly speaking, LEFM analysis is valid only if r_{max} is negligible with respect to the ligament size and the crack length. In an assessment of small defects in high-strength steel, Clark [49] reported that as long as the crack is at least 25 times larger than the associated crack tip plastic zone size, LEFM concepts are directly applicable. Accordingly, in any analysis employing the presumption of LEFM, it will be necessary to calculate the crack tip plastic zone size using equation (4.4) or (4.5) to ensure that the problem under consideration meets the stated criterion.

4.1.3 Finite Element Methods in Fracture Mechanics

Crack Tip Elements

Since the early 1970's, the finite element method has become firmly established as a standard procedure for the solution of practical fracture problems, and the field of fracture mechanics has benefited significantly by advances in finite element technology. In 1979, Heymann [50] conducted an extensive review of the use of isoparametric finite elements for fracture mechanics. More recently, Liebowitz and Moyer [51] presented a broad assessment of methodologies to address elasto-static problems in two- and three-dimensions, elasto-

dynamic problems, elasto-plastic problems and the modeling of stable crack growth. They provide a thorough discussion of some of the early finite element solutions that utilized standard or conventional elements which ignored the singular strain field near the crack. In an attempt to capture the steep stress gradient in the crack tip region, some authors [52, 53] chose a finite element mesh with substantial mesh refinement around the tip of the crack. Considerable effort was expended in generating these meshes, and they were computationally expensive to solve. Recognizing these limitations, alternative techniques were developed that incorporate the asymptotic nature of the strain field directly into the shape functions of the element [46] or that enrich the element displacement field to predict the correct strain field singularity [54]. Another approach for the modeling of elasto-static crack front singularities involves the use of hybrid elements that have an assumed stress or displacement field which includes the asymptotic crack front solution [55, 56]. The weakness of these approaches lies in the use of a nonstandard elemental formulation and the necessity of nonstandard codes.

One of the most accurate techniques for calculating the stress intensity factors is the singular element technique. Henshell and Shaw [57] and Barsoum [58, 59] noticed that by displacing the midside node of an eight-noded quadrilateral isoparametric element (in two-dimensions) to the quarter-point position, the strain field of the element at the crack tip naturally exhibits a square root strain singularity compatible with that of the theoretical strain field. This concept was extended to three-dimensional problems by Ingraffea and Manu [60] and has since been tested by many authors. Later, Manu [61] generalized the method for curved crack fronts.

Singular elements may be either triangular or quadrilateral, in two-dimensions, and either wedge or hexahedral in three-dimensions. Consequently, this technique may be used in any

finite element code which has an eight-noded isoparametric element for two-dimensional plane strain, plane stress and axisymmetric analyses and a 20-noded isoparametric element for three-dimensional crack tip analyses. Another benefit of the singular element technique is that the square root singularity is produced without the assumption of the plane strain asymptotic displacement field, which is an important consideration for three-dimensional problems [51]. Furthermore, the ease of using singularity elements makes their application in linear elastic fracture mechanics very attractive.

Stress Intensity Factor Evaluation

For the case of linear elastic fracture mechanics, the stress intensity factor uniquely defines the stresses, strains and displacements in a sufficiently small region around the crack tip. Thus, the stress intensity factor effectively characterizes a crack and may be considered as a parameter which defines the redistribution of stress in a body resulting from the introduction of a crack. The representation of the stress field around a crack by the stress intensity factor is a basic concept of fracture mechanics, and the main objective is to establish meaningful relations between the value of K and the propagation of the crack. In fatigue applications, accurate determination of the stress intensity factor range, ΔK, is particularly important since the fatigue life is proportional to $(\Delta K)^m$, where m is usually between 2 and 4. Unfortunately, the relationship between the stress intensity factor and the applied load and geometry of a particular crack configuration is generally attainable only through some method of numerical solution of the relevant elasticity equations.

At some level of examination, all welded structures contain pre-existing cracks or crack-like flaws, but the application of fracture mechanics to welded joints is relatively complicated. Fatigue cracks in welded joints may be partly or fully embedded or even

completely through the thickness of the weldment, depending on the type of joint and the stage of crack growth being investigated. The shape of the crack front depends on many variables, including the size and shape of the initial defect, the magnitude and configuration of the load, the type of joint and amount of reinforcement, and the distribution of residual stress. In general, we may assume an elliptical (fully embedded) or semi-elliptical (partly embedded) shape until the crack propagates through the full thickness of the weldment. Through-thickness fatigue cracks are then normally assumed to have straight crack fronts running perpendicular to the plate surfaces. The problem of surface cracks is therefore much more complicated than through-thickness cracks. In the practical analysis of actual welded components, the loading is usually complex and far from being uniform tension or bending, and the component geometry may be another complicating factor. Moreover, the state of stress at the crack tip varies from almost plane stress at the intersection of the crack with the free surfaces to a three-dimensional stress state along the deeper parts of the crack front; consequently, the stress intensity factor varies along the crack front in most cases. An additional complication in the analysis of welded joints is that often the flaw being considered is a semi-elliptical surface crack situated in a field of stress concentration, which results in a stress gradient on the plane of cracking. Furthermore, it is also necessary to accurately calculate the stress intensity factors due to the combined effects of the applied cyclic load and the welding residual stress fields.

Because of these difficulties, exact analytical solutions for fatigue cracks in welded joints are virtually nonexistent. Numerical methods, such as finite elements or the weight function method, have been used successfully to determine the stress intensity factor solutions for various surface and through-thickness crack configurations [46, 57 - 74]. In fact, routine use of fracture mechanics in design has been largely due to the availability of numerically

predicted stress intensity factors (primarily from finite element analyses) [51]. The accuracy of published stress intensity factor solutions, however, varies markedly depending on the techniques employed. This is particularly true for surface cracks with low aspect ratios. In 1979, Newman [69] assessed 14 different stress intensity factor solutions proposed for a surface crack in a finite plate subjected to uniform tension based on correlations to fracture data for a brittle material. A solution which has been widely accepted is that produced by Newman and Raju [71, 73].

Once the numerical solution for a particular finite element representation has been obtained, crack tip stress intensity factors may be estimated by the use of established crack tip relations. A number of different methods may be employed to determine the stress intensity factors from the field solution, including the displacement method, stress method, nodal force method, line integral (energy) method, and virtual crack extension method. In the remaining part of this section, a brief overview of each method will be given. For comprehensive discussion of a particular method and its implementation to numerically determine stress intensity factors, the reader is referred to the texts by Owen and Fawkes [75] and Parker [76].

The *displacement method* involves a correlation of the finite element nodal point displacements with the well known crack tip displacement equations. With a fine mesh of conventional elements, Chan *et al.* [74] used several points behind the crack front to determine the stress intensity factor as a function of the radial distance from the crack tip. Linear regression was then performed to determine the actual stress intensity factor at the point on the crack front. Tracey [46] used the same technique but with special crack tip elements and determined accurate stress intensity factors with much fewer degrees of freedom. Using a relatively coarse mesh of quarter point isoparametric elements, Barsoum [59] equated the finite element displacement of the node directly behind the crack front to the

asymptotic plane strain displacement field. He then solved for the stress intensity factors from the resulting set of linear algebraic equations.

The *stress method* for determining crack tip stress intensity factors is similar to the displacement method. In this case, however, the nodal point stresses are correlated with the well known crack tip stress equations. The stress intensity factor is again obtained as a function of the radial distance from the crack tip, and linear regression must be used to determine the actual value on the crack front.

Raju and Newman [71, 73] introduced an alternative technique that uses the nodal forces to determine the stress intensity factors. The *nodal force method* involves integrating the asymptotic stress fields (obtained for a three-dimensional crack front) and equating the resulting forces (as known functions of the stress intensity factors) to the nodal forces predicted by the finite element model. Once again, the results are then extrapolated back to the crack front using linear regression. In contrast to the crack-opening displacement method, this method employs the general stress solution and requires no prior assumption of either plane stress or plane strain.

Rice [77] developed a *line integral* for an arbitrary contour surrounding a two-dimensional crack that is proportional to the square of the crack tip stress intensity factor. The path independent integral, referred to as the *J*-integral, is expressed in terms of the strain energy density, the traction vector and the displacement vector and is simply equal to the strain energy release rate [78]. By numerically evaluating the line integral for the finite element solution over a path surrounding the crack tip, an estimate of the stress intensity factor may be obtained. This method has been extended to three dimensions using a surface integral and may be used in both LEFM and Elastic-Plastic Fracture Mechanics (EPFM) although some work indicates slight path-dependency of the J-integral in elastoplasticity.

Another approach to the calculation of stress intensity factors is the *virtual crack extension method*, originally proposed by Parks [79]. The stress intensity factor is related to the energy release rate calculated for two configurations with slightly different crack dimensions. This method is both computationally efficient and accurate but requires the assumption of plane stress or plane strain to relate the pointwise energy release rate to the stress intensity factors.

In selecting a particular method to determine the stress intensity factor, it must be emphasized that in finite element analysis the displacements, as the primary unknowns, are calculated more accurately than the stresses or strains, so that the displacement method is generally preferred. The direct use of stresses (or strains) is not recommended as the predicted values from finite element codes are not as accurate as nodal displacements, particularly near the crack front where the singularity exists. Fawkes *et al.* [70] found that the stress intensity values based on displacements were far more consistent than those based on stresses. Because of its proven accuracy and straightforward implementation relative to most other techniques, the displacement method will be utilized in the subsequent analyses. In addition, the accuracy of the solution is significantly increased if crack tip singularity elements (quarter point elements) are employed around the periphery of the crack tip.

The analytical expressions for the displacement variation along radial lines emanating from the crack tip are given by equation (4.3). By substituting the displacement values of u_x or u_y for nodal points along any radial line, as shown in *Figure 4.4*, a graph of the stress intensity factor, K, versus the radial distance from the crack tip, r, may be drawn. Then by discarding the results for nodal points near the crack tip, the K values may be extrapolated back to $r = 0$ [75]. In two-dimensions, many authors have shown that the $\theta = 180°$ line

displacements produce accurate results more consistently than other radial rays [46]. Fawkes *et al.* [70] found θ = 0° and θ = 180° to be the most suitable angles to use in the extrapolation procedure. For certain cases, however, extrapolation was difficult for θ = 0° due to erratic behavior of the calculated *K* values as the crack tip was approached. In three dimensions, similar studies are lacking; however, the two-dimensional results indicate that the mouth opening displacements should produce the most consistent results (i.e. along θ = 180°).
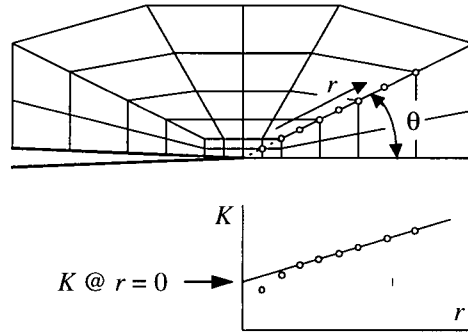
Figure 4.4 **Evaluating Stress Intensity Factors by Displacement Extrapolation [75]**

Substituting for $G = E/2(1+\nu)$ and κ in the second part of equation (4.3) and replacing u_y with the nodal displacement, v_c, in the y-direction along the crack surface (i.e. θ = ± π), the following equations are obtained for the mode I stress intensity factor:

$$K = \frac{E\sqrt{2\pi}}{4(1-\nu^2)} \cdot \frac{v_c}{\sqrt{r_c}} \qquad \text{for plane strain} \qquad (4.6)$$

$$K = \frac{E\sqrt{2\pi}}{4} \cdot \frac{v_c}{\sqrt{r_c}} \qquad \text{for plane stress} \qquad (4.7)$$

where *E* is Young's modulus and r_c is the radial distance along the crack surface from the nodal point to the crack front. This approach may be employed using either conventional finite elements or when crack tip singularity elements are included in the crack tip zone.

Numerical Examples

Before proceeding with the numerical determination of the stress intensity factors for a crack in an actual component, it will be prudent to first evaluate the accuracy of the chosen procedure (i.e. the displacement extrapolation technique employing singularity elements). This will be accomplished by computing the stress intensity factors for two practical yet simplified example problems for which there exists approximate closed form solutions for the stress intensity factors. The first example will demonstrate the general procedure by determining the stress intensity factor for a finite width plate with a central through-thickness crack, as shown in *Figure 4.5 (a)*. The K value will be determined at two locations along the crack front, namely: (1) the mid-thickness location, and (2) the point where the crack front meets the free surface. In the second example, the stress intensity factor will be computed for the same finite width plate but with a semi-elliptical surface crack configuration, as illustrated in *Figure 4.5 (b)*. Again, the stress intensity factor will be determined at two different locations, namely: (1) the deepest point on the crack front, and (2) the point where the crack front meets the free surface.
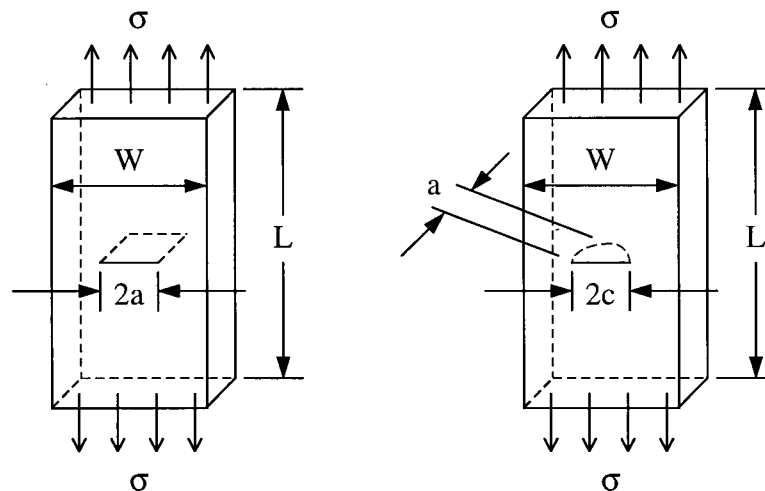
(a) **Through-Thickness Crack**   *(b)* **Semi-Elliptical Surface Crack**

Figure 4.5 **Numerical Example Geometries**

The mechanical properties, geometric dimensions and applied loading condition that were used in both example problems are listed in *Table 4.1*. Two finite element models were constructed using EMRC's DISPLAY III finite element pre- and post-processing program [18]. Due to the symmetry of these problems, only one quarter of the plate geometry was modeled. The finite element mesh, shown in *Figure 4.6*, consists of 672 20-noded isoparametric hexahedral (brick) elements and 3408 nodes. The overall dimensions of the model are 4.0" long x 1.6" wide x 0.5" thick. The finite element mesh has been refined on the crack end of the model, and the elements in this region are approximately 1/8" x 1/16" x 1/16" in the x-, y- and z-directions, respectively.

Table 4.1 **Parameters Used for the Numerical Examples**

Parameter	Example 1	Example 2
Young's modulus, E (psi)	28×10^6	28×10^6
Poisson's ratio, ν	0.3	0.3
Plate width, W (in.)	3.2	3.2
Plate length, L (in.)	8.0	8.0
Plate thickness, T (in.)	0.5	0.5
Crack length (in.)	$2a = 1.07$	$2c = 1.07$
Crack depth (in.)	0.5	$a = 0.25$
Applied normal stress, σ_y (ksi)	21.0	21.0
Material yield strength, σ_{ys} (ksi)	42.0	42.0

The nodes and elements which are situated on the same plane as the crack are illustrated in *Figure 4.7 (a)* and *(b)* for examples 1 and 2, respectively. The nodes that have been colored red are located on the crack front which is represented in each figure by a red line. In the first example, the crack front is a straight line running in the z-direction which simulates a through-thickness crack configuration. For the second example, the crack front corresponds to a semi-elliptical shape with aspect ratio $a/2c \approx 1/4$.
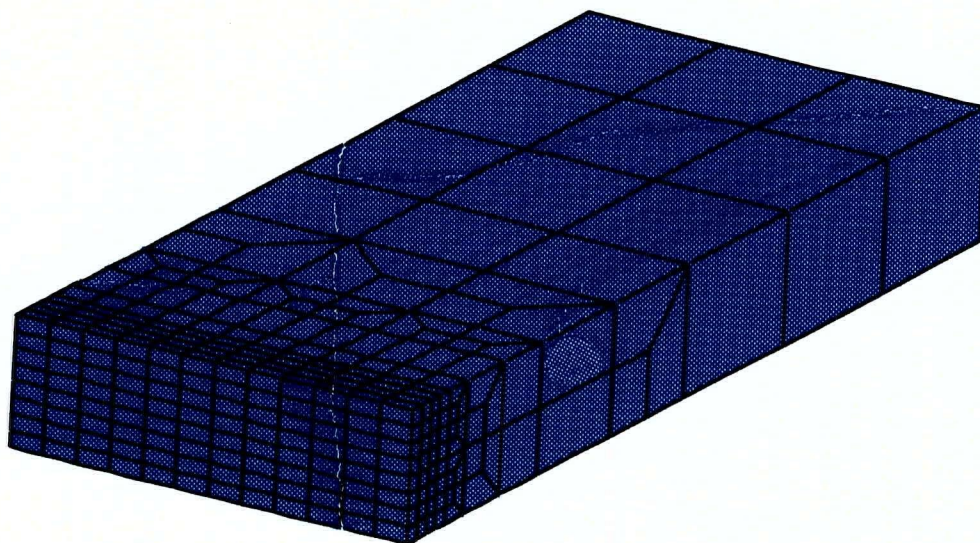
Figure 4.6 **Finite Element Mesh Used for Both Examples**
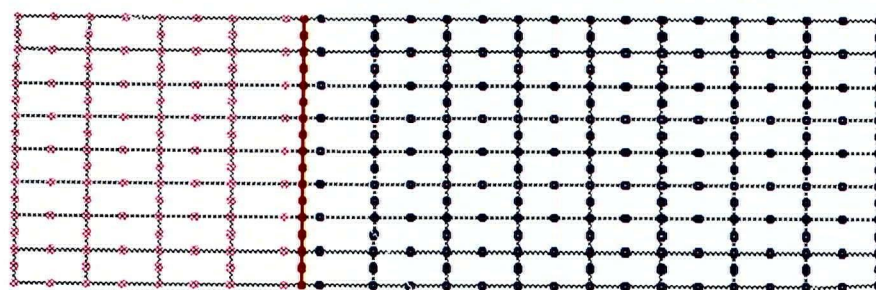
(a) **Through-Thickness Crack**
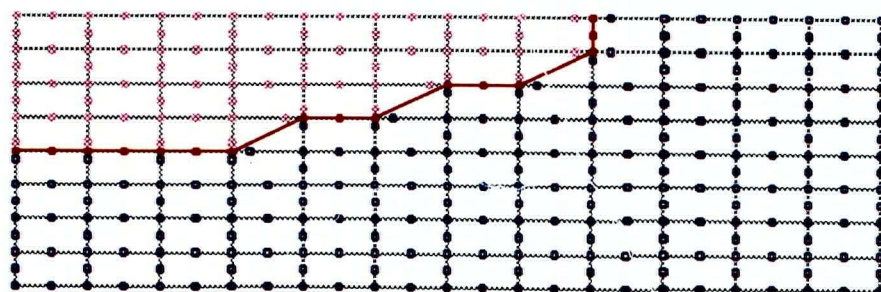
(b) **Semi-Elliptical Surface Crack**

Figure 4.7 **Nodal Configurations on the Crack Plane**

In both cases, the nodes surrounding the crack front were moved to the quarter-point position, as seen in the figures, to produce the appropriate $1/\sqrt{r}$ strain field singularity. Displacement constraints were imposed on the blue nodes to fix them in the y-direction (i.e. $u_y = 0$) which simulates a symmetry boundary condition with respect to the x-z plane (also the crack plane). The nodes located on the left side of the model (i.e. the y-z plane that is not visible in *Figure 4.6*) were also fixed in the x-direction (i.e. $u_x = 0$) to simulate the other half of the plate. The magenta nodes are located on the free surface of each crack and were not restricted from movement in any direction. A uniform load was then applied in the y-direction at the opposite end of each model.

Once the field solution had been obtained for both example problems, the displacement extrapolation procedure was used to evaluate the stress intensity factors. The results are presented in graphical form in *Figure 4.8* for the through-thickness crack configuration and in *Figure 4.9* for the case of a semi-elliptical surface crack. The analytical stress intensity values were calculated from the following closed form solutions taken from Broek [48]:

$$K = \sigma \sqrt{a\pi} \left(sec\frac{a\pi}{W} \right)^{\frac{1}{2}} \qquad \text{for example 1} \qquad (4.8)$$

$$K = \frac{\sigma \sqrt{a\pi}}{\Phi} \left(sin^2 \varphi + \frac{a^2}{c^2} cos^2 \varphi \right)^{\frac{1}{4}} \qquad \text{for example 2} \qquad (4.9)$$

where $\Phi \approx \frac{3\pi}{8} + \frac{\pi}{8}\frac{a^2}{c^2}$ and $\varphi = 0$ at the free surface (at the end of the major axis) and $\varphi = \pi/2$ at the deepest point on the crack front (at the end of the minor axis). Strictly speaking, equation (4.9) is intended for an embedded elliptical flaw; however, it may also be applied to a semi-elliptical surface flaw with only slight modifications. Usually a number of correction factors are applied to this equation.
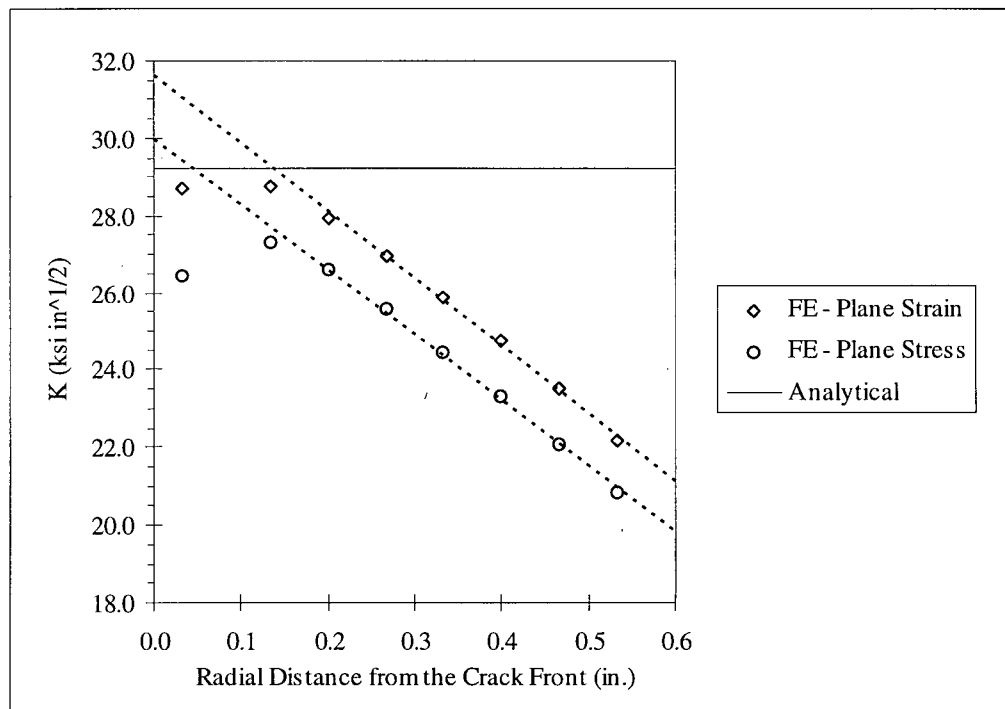
Figure 4.8 **Stress Intensity Factors for a Through-Thickness Crack**
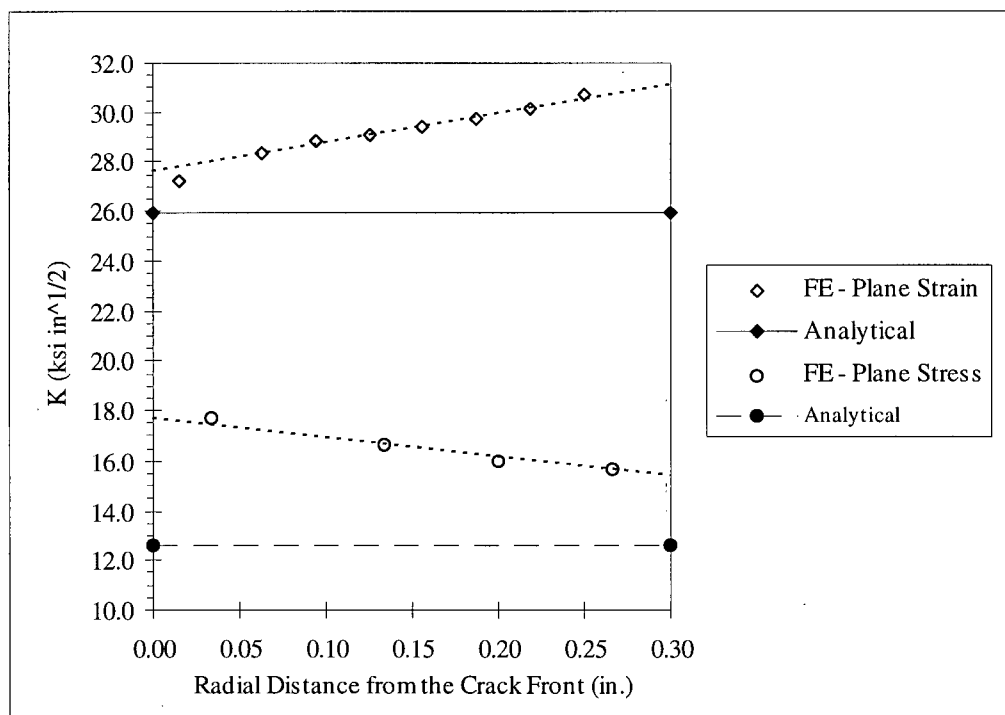
Figure 4.9 **Stress Intensity Factors for a Semi-Elliptical Surface Crack**

Since a surface flaw is comparable to an edge crack, it was argued that this requires a correction of about 12 per cent to K. This is called the back free-surface correction. A correction is also necessary to account for the proximity of the free surface in front of the crack, which is given by Broek in graphical form. Also, for the case where a semi-elliptical flaw extends deep into the material, the back free-surface correction should be decreased from 1.12 to unity. In example 2, therefore, the back free-surface correction term was reduced to 1.06 because the crack had propagated halfway through the thickness of the plate.

The numerically predicted stress intensity factors are compared to the corresponding analytical values in *Table 4.2*. For the first example, the numerical results are accurate to within 10 per cent of the analytical value, and the surface location appears to provide marginally better results than the mid-thickness location. In the second example, the numerical results are also quite accurate at the deepest location on the crack front, but the stress intensity value obtained at the surface location is much higher than the corresponding analytical value. This occurred because the relatively coarse mesh does not accommodate a smooth, elliptical curve as the crack front approaches the free surface. The irregular shape effectively produces undesirable stress raisers near the free surface. This exaggerates the stress concentration from the crack which, in turn, distorts the local displacement solution.

Table 4.2 **Comparison of Numerical and Analytical Stress Intensity Values**

Description	Numerical (ksi√in)	Analytical (ksi√in)	Difference (%)
Example 1:			
Mid-thickness location (plane strain)	31.6	29.2	+ 8.2
Surface location (plane stress)	30.0	29.2	+ 2.7
Example 2:			
Deepest location (plane strain)	27.6	26.0	+ 6.2
Surface location (plane stress)	17.6	12.6	+ 39.7

In view of these findings, the numerical procedure to evaluate the stress intensity factors will not be used at the surface location of the semi-elliptical crack configuration. This is not to imply that the numerical procedure is not accurate, but that the present finite element mesh is not suitable for an accurate evaluation of the stress intensity factor at this particular location along the crack front. The numerical procedure will therefore be limited to the evaluation of the stress intensity factors at the other three locations. In the forthcoming numerical study, the stress intensity factor is only required at the deepest location along the crack front; consequently, further mesh refinement would serve no practical purpose. It is also noteworthy to mention that the predicted values were all slightly greater than the corresponding analytical values which should lead to a conservative estimate of the fatigue crack propagation life.

4.1.4 LEFM and Fatigue Crack Propagation

Understanding fatigue crack growth is essential in predicting the service lives of many structures subjected to fatigue loading. This is particularly true for welded structures wherein sub-critical flaws may be introduced during fabrication. It is widely accepted that weldments are more susceptible to fatigue failure than the base material because of problems related to the presence of inclusions, lack of penetration, incomplete fusion, changes in microstructure and the introduction of residual stresses [80]. Except for relatively rare instances of brittle fractures from flame-cut or sheared edges, dents or gouges, most brittle fractures in fabricated steel structures over the last fifty years appear to have been associated with welded joints, and weld related pre-existing cracks or crack-like flaws [21]. Due to the presence of such defects, cracks may develop at a welded joint at an early stage in the life of the structure, so the

initiation process of fatigue cracks normally covers only a small portion (< 10%) of the total life [22]. Thus, the crack growth life estimation is more important for a welded structure, and it is a common practice to neglect the crack initiation period completely [33, 38].

The prediction of fatigue life using linear elastic fracture mechanics concepts and a crack growth law is well known. The first significant breakthrough was made when Paris *et al.* [81] advanced the idea that crack growth might be proportional to the applied stress intensity factor; this was later refined by Paris *et al.* [82] to a dependency on the range of stress intensity factor. This work was significant because it permitted a treatment of crack growth that was quantifiable in terms of material properties and stress analysis. It consists of defining the stress intensity range, ΔK, as:

$$\Delta K = K_{max} - K_{min} \qquad\qquad K_{min} > 0 \qquad\qquad (4.10)$$

$$\Delta K = K_{max} \qquad\qquad K_{min} \leq 0 \qquad\qquad (4.11)$$

where K_{max} and K_{min} are the effective maximum and minimum stress intensity values, respectively, during a given load cycle. Equation (4.11) implies that the part of the fatigue cycle during which the crack tip is closed makes no contribution to crack growth. This result is based on the premise that when a crack is closed, the crack tip singularity is removed and no fatigue damage will occur. For much of a component's lifetime, the fatigue crack growth rate, *da/dN*, under the small scale yielding condition may be related to the stress intensity range according to Paris' law [82]:

$$\frac{da}{dN} = C \, (\Delta K)^m \qquad\qquad (4.12)$$

where N represents the number of cycles, and C and m are experimentally determined material constants, with a cut-off at $\Delta K = \Delta K_{th}$, called the threshold stress intensity factor range. This concept works remarkably well for the majority of the propagation life of a

crack, that is, after it initiates and before it reaches the stage of impending failure. This intermediate region of power-law behavior described by the Paris equation is generally referred to as *Stage Two* crack growth. To illustrate this concept, *Figure 4.10* shows a logarithmic plot of the crack growth per cycle, *da/dN*, versus the stress intensity factor range, *ΔK*, corresponding to the load cycle applied to a sample. The fatigue crack propagation data were experimentally determined from five specimens of ASTM A533 B-1 steel tested at 24°C [83]. A plot of similar shape is expected for most structural alloys; the absolute values of *da/dN* and *ΔK* are dependent on the material. The fracture mechanics description of fatigue crack growth, as summarized in *Figure 4.10*, is broadly applied to calculate the growth rate and fatigue life of components and structures. It may be seen that extrapolation of the linear portion of the curve (i.e. power-law behavior) to lower stress intensities is definitely safe, in that it predicts a faster rate of crack propagation than is really applicable. Only at very high stress intensities, where final failure is imminent, does the extrapolation become unsafe and the actual rate of propagation for a given *ΔK* become higher than that given by the extrapolated line. However, in that region the crack will be propagating very rapidly so that only a small part of the total life will be affected and the resulting error in life will be small.

In welded joints, fatigue cracks may propagate in weld metal of varying dilution, heat-affected zone (HAZ) and base or parent material. However, it is generally found that *da/dN* is not sensitive to microstructure, so the same crack growth constants are applicable to all three regions of a weldment [33]. In addition to the stress intensity range, it is well known that fatigue crack propagation also depends on the mean stress. The parameter commonly associated with the level of mean stress is known as the stress ratio or *R*-ratio, where:
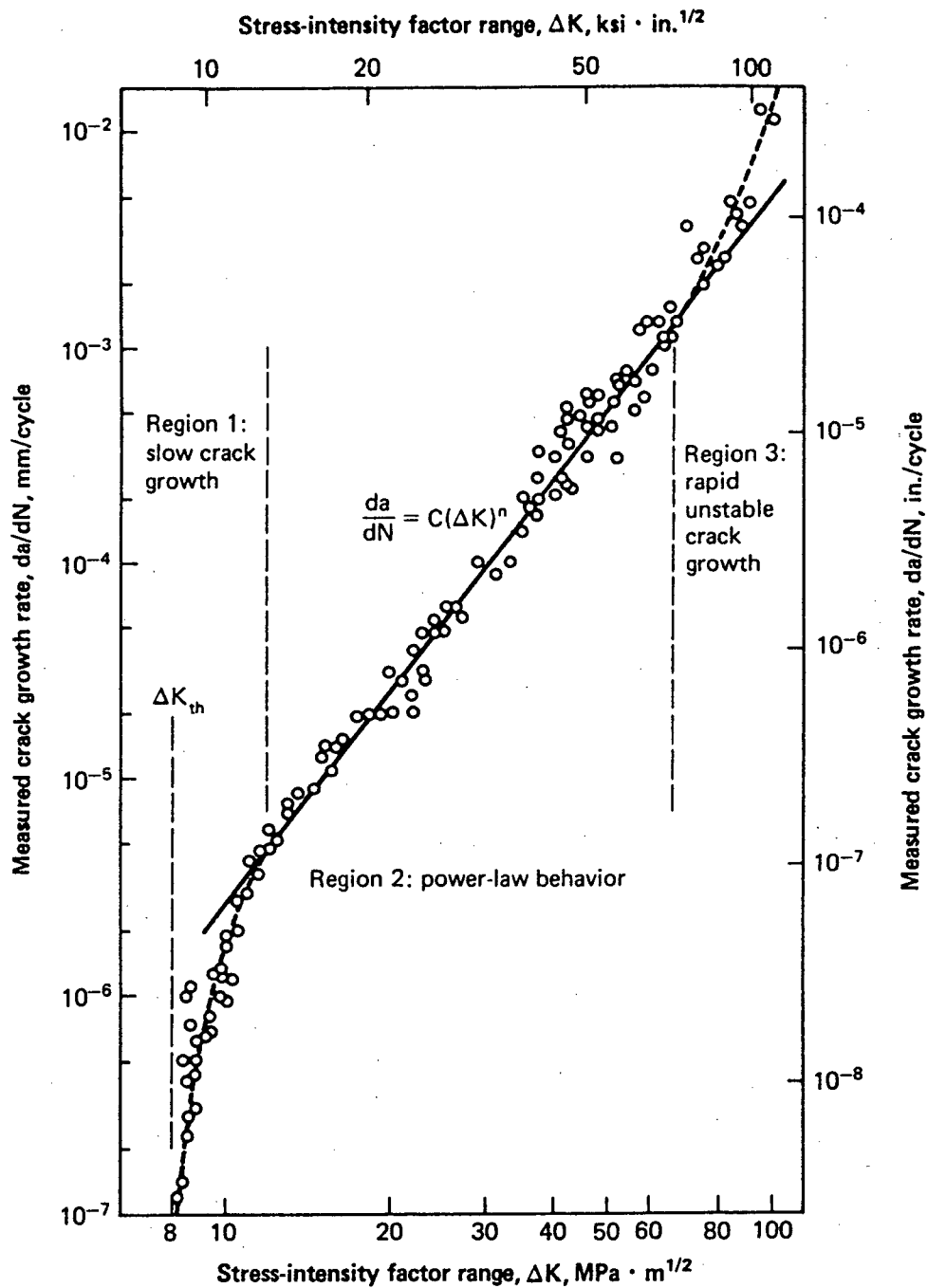
The material was ASTM A533 B-1 steel, with a yield strength of 470 MPa (70 ksi).

Test Conditions: R = 0.10; ambient air; 24 °C (75 °F)

Figure 4.10 **Fatigue Crack Growth Behavior of A533 Steel [83]**

$$R = \frac{K_{min}}{K_{max}} \qquad\qquad K_{min} > 0 \qquad\qquad (4.13)$$

$$R = 0 \qquad\qquad K_{min} \leq 0 \qquad\qquad (4.14)$$

For the same stress intensity range, a higher stress ratio will generally result in a higher crack growth rate. Since equation (4.12) does not take into account the effects of mean stress, a family of curves relating stress intensity range to crack growth rate will be obtained for different values of R. Irving *et al.* [84] and Schijve [41] have critically reviewed a number of alternative crack growth laws which are able to predict the crack growth rates more completely than Paris' law. Uncertainties inherent in the fatigue process, however, frequently eliminate any advantage of using a more complicated growth law. Consequently, equation (4.12) has been adopted as the most useful crack growth relation because it is unique in its simplicity and wide-ranging applicability [22, 26, 38, 65, 85].

When a cracked component also contains residual stresses, it has a residual stress intensity factor, K_r, in addition to the maximum and minimum values of stress intensity produced by the remote cyclic loading. Given that the stress intensity factors are derived from a linear static analysis, the approach employed most frequently to account for the effect of residual stress on the crack growth rate involves superposition of the respective stress intensity factors [36, 37, 39]. The residual stress intensity factor, K_r, is normally obtained by loading the crack faces with the residual stresses which exist normal to the plane of potential crack growth in the uncracked body. When residual stresses are present, the above equations for ΔK and R may be rewritten as:

$$\Delta K = K_{max} - K_{min}$$

$$R_r = \frac{K_{min} + K_r}{K_{max} + K_r} \qquad\qquad K_{min} + K_r > 0 \qquad\qquad (4.15)$$

$$\Delta K = K_{max} + K_r$$

$$R_r = 0 \qquad\qquad K_{min} + K_r \leq 0 \qquad\qquad (4.16)$$

where R_r is the effective stress ratio when residual stresses are considered. Parker [36] provides a thorough discussion of equations (4.15) and (4.16) for the cases of an edge-cracked plate with: (i) compressive residual stress subjected to cyclic tensile loading; (ii) tensile residual stress subjected to cyclic compression; and (iii) tensile residual stress subjected to cyclic tension. When the applied cyclic loading is fully tensile, tensile residual stresses raise the effective R-ratio above R for the applied loading. Glinka [39] investigated the growth rate in center-cracked sheet specimens through regions of tensile and accompanying compressive residual stress produced by transverse and longitudinal butt welds. Constant amplitude loading was applied at R-ratios between 0.35 and 0.5. He obtained reasonably good predictions of crack growth in terms of ΔK and R_r using equation (4.15), as long as the cracks were within the regions of tensile residual stress. In his analysis, Glinka used Forman's equation [86] to predict the influence of the effective stress ratio on the crack growth rate.

As mentioned in the earlier discussion on residual stresses, a growing fatigue crack will also generate its own residual stress field. The significance of crack-generated residual stress was first discussed by Elber [42], who observed that the residual tensile displacements left in the wake of a crack would cause it to close before the tensile load was removed (under $R \geq 0$ loading). Thus compressive residual stresses were generated normal to the fracture surface when the tensile load was completely removed. Upon reapplying the load, the crack would not open until a certain level of tensile loading was applied to overcome the crack opening stress resulting from the compressive residual stresses. In the literature, this phenomenon is referred to as *crack closure*, and the wake of compressive residual stress is sometimes called

the Elber mechanism [41]. By correlating the crack growth rate with only that portion of the loading cycle in which the crack is fully open at the crack tip, and by noting how the crack opening stress varied with applied mean stress and loading sequence, Elber was able to provide a plausible physical explanation for R-ratio effects and crack growth retardation caused by tensile overloads.

Elber proposed an expression for the crack propagation rate in terms of the effective stress amplitude for an aluminum alloy [42]. During a stress cycle, a fatigue crack will be partly or fully closed as long as $S < S_{op}$, as illustrated in *Figure 4.11*. Elber then suggested that the applied stress variation will contribute to crack extension only if $S > S_{op}$, which leads to the definition of an effective stress range, ΔS_{eff}:

$$\Delta S_{eff} = S_{max} - S_{op} \tag{4.17}$$

where S_{max} is the maximum applied cyclic stress and S_{op} is the crack opening stress. An effective stress range ratio, U, was then defined as:

$$U = \frac{(S_{max} - S_{op})}{(S_{max} - S_{min})} = \frac{\Delta S_{eff}}{\Delta S} \tag{4.18}$$

where ΔS is the applied stress range. The effective stress range ratio is also commonly referred to as the crack opening ratio. Accordingly, Elber then defined the effective stress intensity range, ΔK_{eff}, as:

$$\Delta K_{eff} = U \, \Delta K \tag{4.19}$$

and postulated that a better analysis of crack propagation rates might utilize the effective stress intensity range concept. This prompted Elber to test the following functional form of the crack propagation equation:

$$\frac{da}{dN} = C \, (\Delta K_{eff})^m = C \, (U \Delta K)^m \tag{4.20}$$
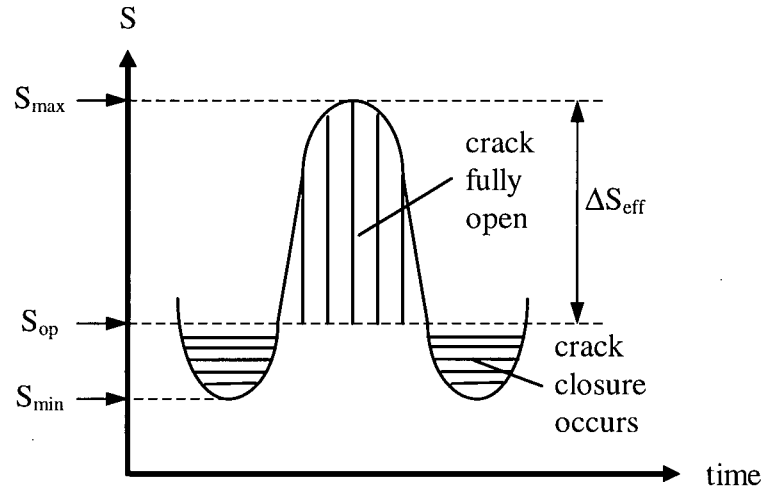
Figure 4.11 **Illustration of Fatigue Crack Closure [41]**

Elber conducted a series of constant amplitude tests on an aluminum alloy to establish the relationship between the crack opening ratio and the three variables which were anticipated to have a significant effect on U, namely, stress intensity range, crack length and stress ratio. The stress intensity was varied over the range $13 < \Delta K < 40$ MN/m$^{3/2}$, and the stress ratio was varied over the range $-0.1 < R < 0.7$. His test results indicated that U was a linear function of the stress ratio only and could be expressed as:

$$U = 0.5 + 0.4R \qquad\qquad -0.1 < R < 0.7 \qquad\qquad (4.21)$$

for 2024-T3 aluminum alloy. Elber concluded by demonstrating that his approach using the crack closure equation correlated to existing data better than equations developed by Forman and Erdogan, and many researchers presently consider that ΔK_{eff} is the most reasonable parameter to evaluate the crack propagation rate under small scale yielding conditions [27].

Itoh *et al.* [31] investigated the effects of residual stresses on fatigue crack growth by conducting experiments using a low-alloy carbon steel (JIS SS41) and an austenitic stainless steel (JIS SUS304). Welded and unwelded specimens were tested under constant and

variable amplitudes with stress ratios $R > 0$. When he plotted the fatigue crack propagation data using the effective stress intensity range, based on measurements of the crack opening ratio, the experimental crack growth rates in welds were found to be in excellent agreement with the results of base metal specimens. In addition, the growth rates for different stress ratios appeared equivalent. He therefore concluded that residual stresses produce the same effect on the crack growth rate as the stress ratio. This finding was important for the study of fatigue cracking in welded joints because the results make it possible to predict the fatigue crack growth rates on the basis of data obtained from base materials.

More recently, Lu [25, 26] developed an engineering procedure for estimating the crack growth behavior and fatigue lives of semi-elliptical surface cracks at weld toes which takes into account the influence of residual stress. In his analysis, Lu used experimental data published by Itoh *et al.* [31] to yield the following estimation formula for the crack opening ratio:

$$U = \frac{0.53}{(\frac{1}{n} - R)^{0.65}} \qquad (n = 1 - 2)$$

$$U \leq 1 \qquad\qquad\qquad (4.22)$$

where a suitable value between 1 and 2 may be chosen for the variable n. The relationship between U and R is shown in *Figure 4.12* for the permissible boundary values of n. According to equation (4.22), when $n = 1$, the effect of crack closure is taken into account when $R < 0.62$; for larger effective R-ratios the crack closure is considered not to have occurred. For $n = 2$, the effect of crack closure is taken into account only for $R < 0.12$; the effect of crack closure is neglected when $R > 0.12$. When n increases, the R range in which the effect of crack closure is taken into account is decreased, and the crack opening ratio increases. Thus the effective stress intensity range, ΔK_{eff}, increases, and the estimated fatigue

life will decrease. Setting $n = 2$ in equation (4.22) provides the most conservative values for the crack opening ratio and tends to be safe in terms of the estimated fatigue life. Values of n closer to unity, however, correlate better with the published experimental data. It should also be noted that when residual stresses are present, the effective stress ratio, R_r, should be substituted for the applied stress ratio, R, in equation (4.22).
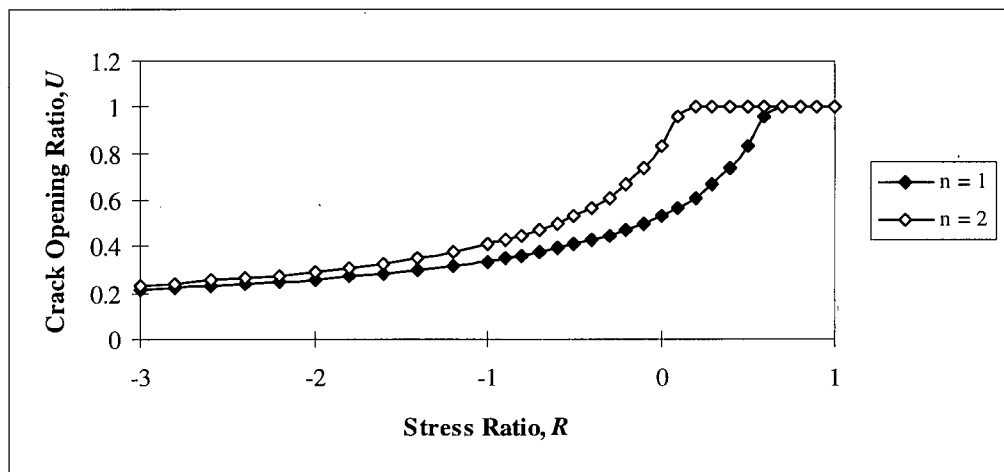
Figure 4.12 **U versus R Relation [26]**

4.2 Method for Predicting the Fatigue Crack Growth Rate

In view of the foregoing preliminaries, a practical method for estimating the propagation rate of crack-like defects in weldments may now be presented. The following approach for predicting the fatigue crack growth rates in residual stress fields was proposed by Ohji *et al.* [87] and subsequently investigated by Itoh *et al.* [31] using the concept of effective stress intensity range. The procedure may be separated into five distinct steps as shown in the flow chart in *Figure 4.13*. Experimental data and/or empirical relations are required at two stages in the procedure to relate various parameters to the appropriate material property information.
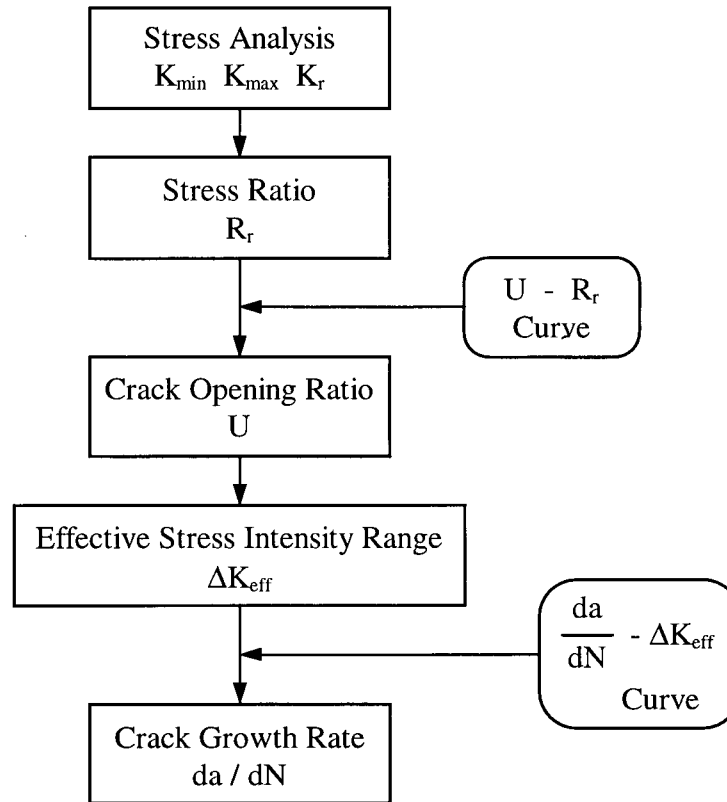
Figure 4.13 **Flow Chart for Predicting the Fatigue Crack Growth Rate [87]**

The first step in the procedure is to perform stress analyses on the cracked component to determine the maximum and minimum cyclic stress intensity factors, K_{max} and K_{min}, as a function of crack depth. The stress intensity factors attributed to the welding induced residual stress, K_r, are also necessary for the crack growth rate prediction. In its present form, this procedure may be used to accurately predict the crack growth rate for a given crack path. When the actual crack path is not known and a reasonable estimate can not be made with confidence, the procedure may be modified to include a prediction for the crack growth path by comparing the stress intensity factors at different points along the crack front [26]. Accordingly, the method for evaluating the stress intensity factors must be sufficiently accurate over the entire length of the crack. In the present investigation, the stress intensity

factors were computed at the deepest point on the crack front using finite element analysis and the displacement extrapolation technique that was demonstrated in Section 4.1.3. Details of a numerical study pertaining to disc filter core pipes will be presented in the next chapter.

Having determined the stress intensity factors due to the residual stresses and applied cyclic loading, the effective stress ratio, R_r, may then be calculated as a function of crack depth. Using Lu's [26] relationship between the crack opening ratio, U, and the effective stress ratio, R_r, the effective stress intensity range, ΔK_{eff}, may then be obtained. In his analysis, Lu selected $n = 1.14$ based on experimental data for low-alloy carbon steels and austenitic stainless steels. In the present investigation, the disc filter core pipe is also manufactured from an austenitic stainless steel (i.e. AISI 316L) so the same n-value was used in the subsequent analysis.

The crack growth rate, da/dN, may finally be determined as a function of crack depth using the relationship between da/dN and ΔK_{eff}. Unfortunately, published fatigue crack propagation rates (i.e. da/dN curves) for a particular material and loading condition are normally presented in terms of the applied stress intensity range, ΔK, and the applied stress ratio, R, for base metal specimens. Consequently, it is usually necessary to convert the available data into crack growth rates corresponding to the effective stress intensity range. This may be accomplished using Lu's expression for the crack opening ratio, U, together with the R-ratio that was used during the fatigue crack propagation testing [31]. The ΔK values from the experimental data or published da/dN - ΔK relation may be converted to ΔK_{eff} values by multiplying by the resulting U value.

For a given increment of crack depth, Δa_i, the corresponding number of load cycles, ΔN_i, is then determined from the following equation:

$$\Delta N_i = \frac{\Delta a_i}{(da/dN)_i} \tag{4.23}$$

where $(da/dN)_i$ is usually taken as the average value of the crack propagation rate over the increment. Knowing the frequency of applied loading, f_a, the total fatigue crack propagation life, L_T, may then be estimated from total number of load cycles, N_T:

$$L_T = \frac{N_T}{f_a} = \frac{1}{f_a} \sum_{i=1}^{m} \Delta N_i \tag{4.24}$$

where m is the number of crack depth increments used in the analysis.

CHAPTER 5

NUMERICAL STUDY: DISC FILTER CORE PIPE PROJECT

5.1 Introduction

In the introductory chapter, the industrial function, construction, and operation of rotary vacuum disc filters were discussed. The weld cracking problem experienced in Ingersoll-Rand's disc filter core pipe was then investigated through a complete failure analysis where it was concluded that corrosion fatigue cracking emanating from lack of penetration root defects was the likely failure mechanism. To substantiate this conclusion, a numerical study is now presented which employs the finite element and fracture mechanics concepts demonstrated in the previous two chapters. The primary objective of this investigation is to determine the fatigue crack propagation life resulting from the growth of a given crack-like defect located at the weld root. In the following analysis, life estimates will be determined in both air and simulated white-water environments for the original Ingersoll-Rand core pipe design and for a new design that was recently developed through a cooperative project undertaken by Tristar Industries Ltd. and UBC's Finite Element Analysis and Research Lab.

The finite element model geometries corresponding to a small region of the outer shell for the original and new core pipe designs are illustrated in *Figure 5.1 (a)* and *(b)*, respectively. Each disc filter segment (a total of 18 are located around the circumference) is held to the core pipe by two captive bolts and joined to the two adjacent segments at the periphery. In the original Ingersoll-Rand design of the core pipe, the outer shell consists of 8″ wide annular rings of alternating material thickness. The support rings under each disc filter are 3/4″ thick
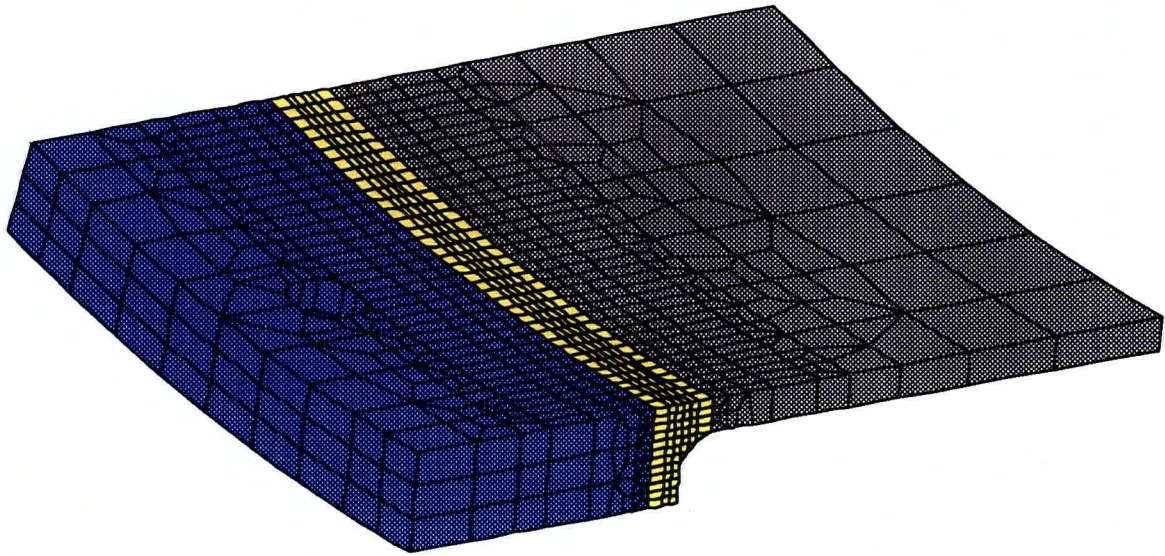
(a) **Original Design**
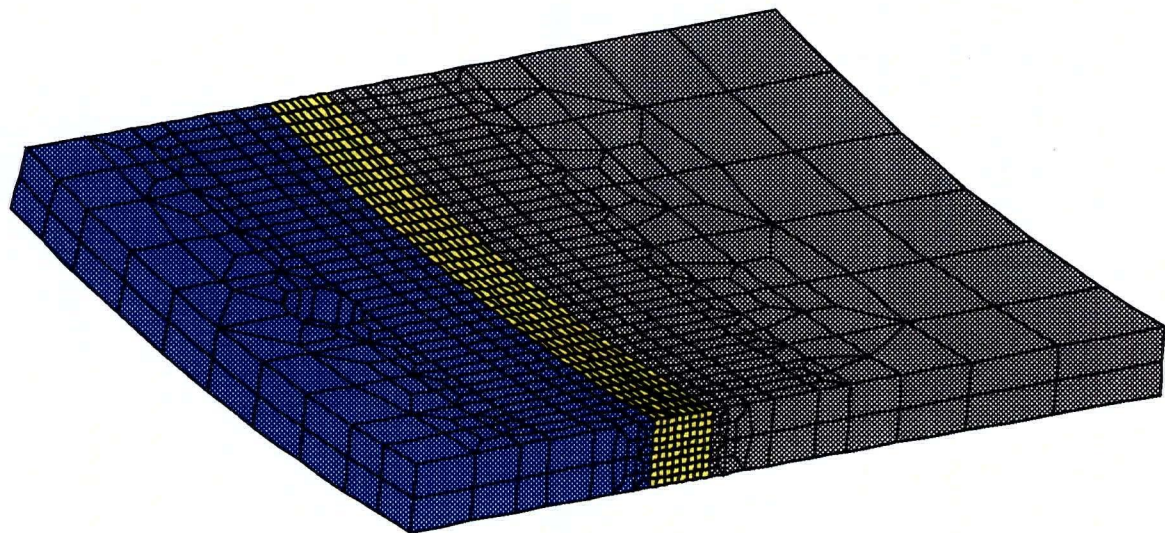
(b) **New Design**

Figure 5.1 **Finite Element Model Geometries of the Core Pipe Weldment**

while the spacer rings between consecutive disc filters are only 1/4″ thick; consequently, a circumferential weld is required every 8″ down the full length of the core pipe (over 30′) to join the annular rings together. The process of welding each annular ring to the inner part of the core pipe is arduous, time consuming and thus expensive. In the new design, however, the outer shell is manufactured with a uniform material thickness of 1/2″. The outer shell can therefore be installed in longer sections (up to 6′ in length) which facilitates the assembly process and significantly decreases the required number of circumferential welds.

Both finite element models consist of approximately 4,000 quadratic, 15-noded (wedge) or 20-noded (brick) solid isoparametric elements with over 18,500 nodes. The boundary conditions from a coarse, three-dimensional solid model of a larger region of the core pipe [88] were transferred to the present models using the sub-modeling technique that was demonstrated in Chapter 3. The boundary conditions were taken from the lower or tensile region at the mid-span location of the core pipe, corresponding to the position of the maximum bending moment and highest cyclic stresses, which produce the most severe operating conditions for the joint under consideration.

To begin the fatigue crack propagation analysis, a lack of penetration defect was assumed to exist at the root of the weld, oriented parallel to the weld line and normal to the inner surface of the shell. In the earlier metallurgical analysis, the striations from several different cracks revealed relatively flat, semi-elliptical crack front profiles with small aspect ratios. To accurately model these crack shapes, the finite element mesh was refined considerably in the immediate region of the weld. It was not practical, however, to construct a mesh that corresponds exactly to the semi-elliptical shape because the stress intensity factor is only required at the deepest point along each crack front. In the previous chapter, the second

numerical example demonstrated that the stress intensity factor could be evaluated accurately at the deepest point along a semi-elliptical crack front without precisely modeling the ends of the crack. Accordingly, a series of crack growth profiles was assumed for the original and new design configurations, as illustrated in *Figure 5.2 (a)* and *(b)*, respectively. The initial defect, referred to as *crack front number 1*, is approximately 5/8″ long (2c) at the surface by 1/16″ deep (a) at the center of the crack which results in an aspect ratio (a/2c) of 0.1. Subsequent crack fronts (i.e. 2, 3, etc.) progressively advance by 1/16″ at the deepest location while maintaining the same aspect ratio until the crack propagates completely through the thickness of the weldment when it becomes a straight-fronted, through-thickness crack.
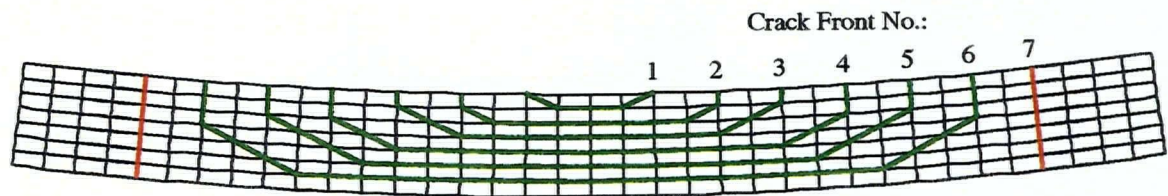
(a) **Original Design**
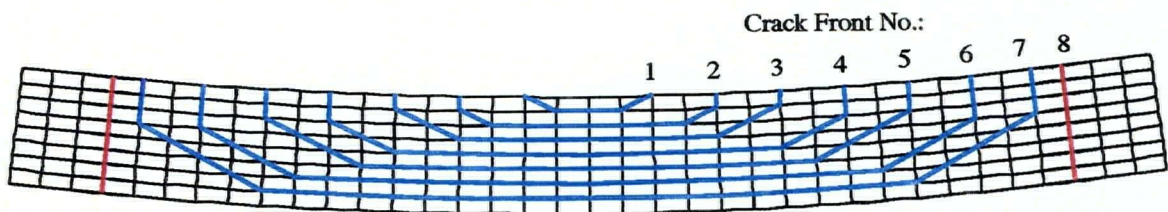
(b) **New Design**

Figure 5.2 **Assumed Crack Growth Profiles Along the Center of the Weld**

The disc filter core pipe is presently constructed from AISI 316L austenitic stainless steel which is a common material selected for a wide range of corrosion conditions encountered in pulp and paper mills [3, 4]. The chemical compositions and typical mechanical properties of 316L plate material (solution annealed) are given in *Table 5.1*. For applications in industrial processes requiring a substantial level of corrosion resistance, this grade has added molybdenum (compared to basic type 304) to increase its resistance to pitting caused by chlorides. For severe environments in which chloride stress-corrosion cracking is the primary concern, superaustenitics, duplex stainless steels, or superferritics should be considered. In the forthcoming analysis, however, the discussion is limited to 316L with the numerical study focusing on the calculation of the fatigue crack propagation life for the new design and comparing it to the result obtained for the original Ingersoll-Rand design.

Table 5.1 **Chemical Compositions and Mechanical Properties for AISI 316L [89, 90]**

Chemical Compositions	wt %
C	0.014
Mn	1.45
Si	0.53
P	0.022
S	0.0003
Cr	17.17
Ni	12.60
Mo	2.58
N	0.069
Fe	Balance
Mechanical Properties	
Elastic modulus, E	28×10^6 psi
Poisson's ratio, ν	0.3
Yield strength, σ_{ys}	42 ksi
Ultimate tensile strength, σ_{uts}	81 ksi

5.2 Stress Analysis Results

5.2.1 Applied Loading

Rotary vacuum disc filters are designed for applications where large flows or difficult to dewater slurries require slow filter rotating speeds, typically in the range of 1 to 2 rpm. Each time the disc filter completes a single revolution, every point on the periphery of the central core pipe structure experiences one complete stress cycle attributable to the applied service loading. During normal operation, the service load consists of the distributed weight of the entire rotating assembly (between the main bearings) including the core pipe, disc filter segments, fiber mat formed on the discs, as well as the forces exerted by the knock-off and face cleaning showers. In an earlier numerical investigation [88], the cyclic stresses on the outer shell of the core pipe were found to be almost fully reversing with the maximum values located approximately midway between the two main bearings. As expected, the maximum tensile stress occurs on the bottom (lower) surface of the core pipe while the maximum compressive stress occurs on the top (upper) surface. If a small crack-like defect (i.e. lack of penetration) is located anywhere along a circumferential weld, it will experience the same cyclic stress conditions causing the crack to open and close once during each revolution of the equipment.

The service loading conditions existing on the lower surface of the outer shell of the core pipe, located at the midway position between the main bearings, were imposed as boundary conditions on the finite element 'crack' models presented in the previous section. The resulting normal stress (S_{zz}) contours for the original (Ingersoll-Rand) and new designs are illustrated in *Figure 5.3 (a)* and *(b)*, respectively, for one of the surface crack configurations (i.e. *crack front number 5*). In this figure and in the subsequent stress contour plots, a section

(KSI)
40.41
36.22
32.02
27.83
23.63
19.43
15.24
11.04
6.848
2.652
-1.544
-5.740
-9.936
-14.13
-18.33

(a) **Original Design**

(KSI)
15.36
14.04
12.71
11.39
10.06
8.736
7.411
6.086
4.760
3.435
2.110
.7850
-.5401
-1.865
-3.190
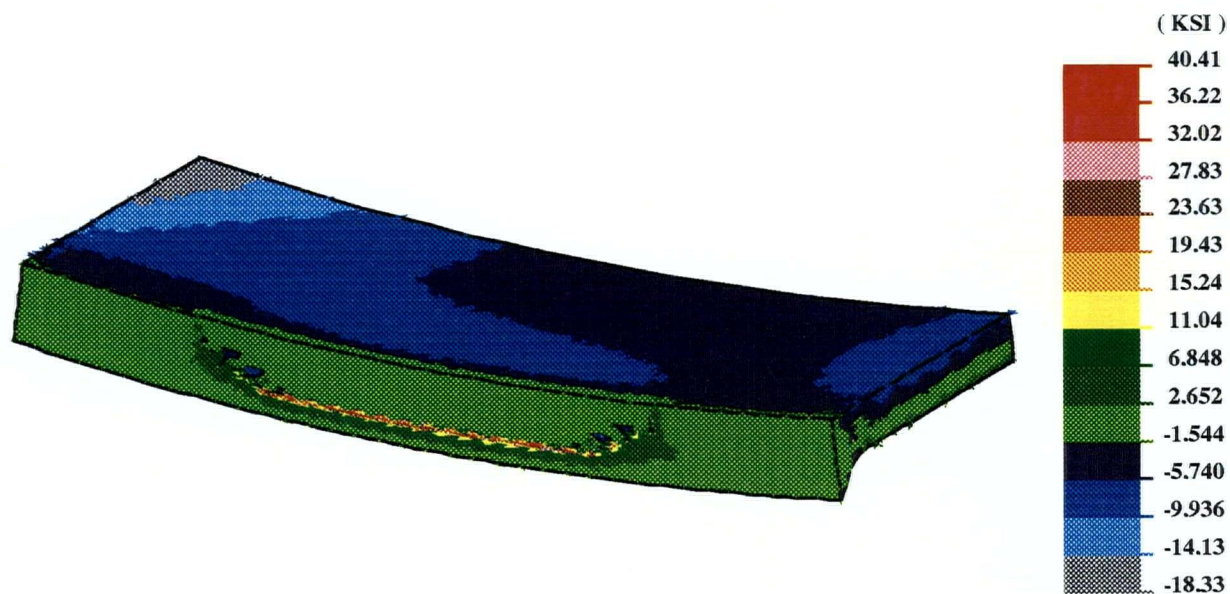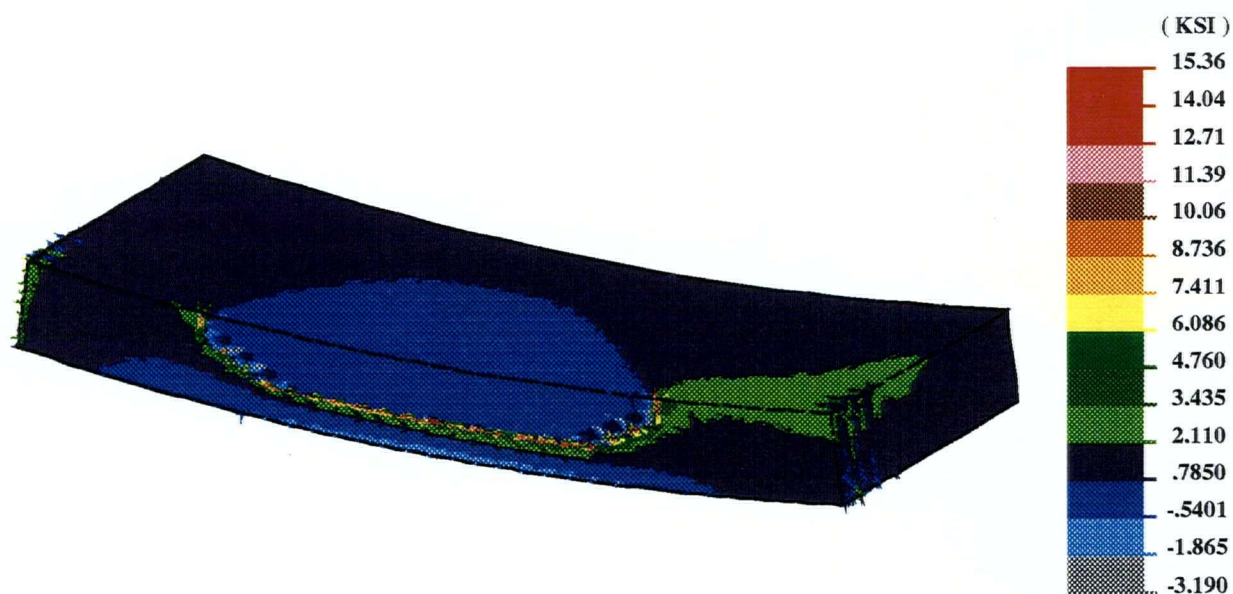
(b) **New Design**

Figure 5.3 S_{zz} **Stress Contours due to the Applied Loading - Crack Front No. 5**

(KSI)
154.9
141.5
128.2
114.8
101.4
88.01
74.63
61.25
47.87
34.49
21.11
7.730
-5.651
-19.03
-32.41

(a) **Original Design**

(KSI)
55.07
50.71
46.34
41.97
37.61
33.24
28.87
24.51
20.14
15.77
11.41
7.040
2.673
-1.694
-6.060
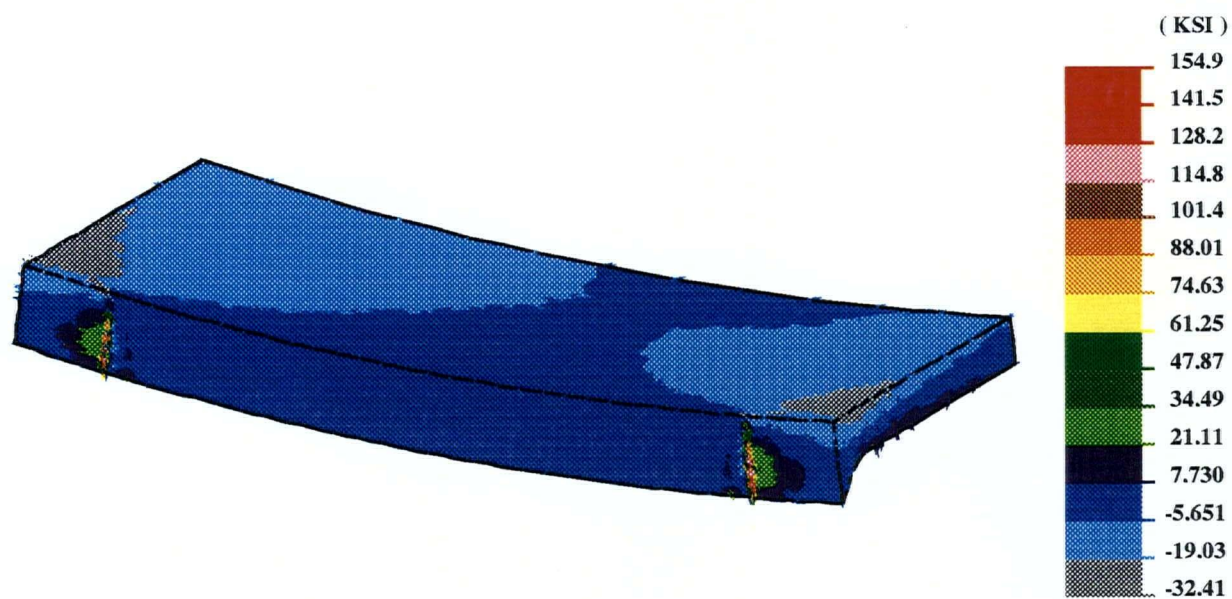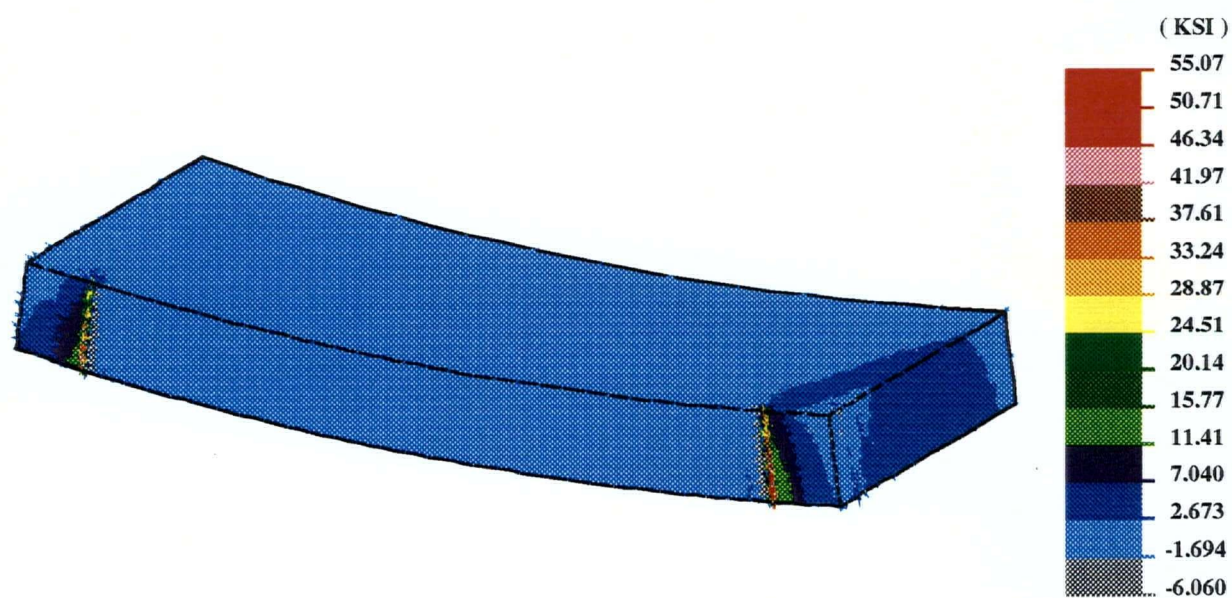
(b) **New Design**

Figure 5.4 S_{zz} **Stress Contours due to the Applied Loading - Through-Thickness Crack**

was taken through the center of the crack plane to illustrate the normal stress distribution surrounding the crack front and in the remaining ligament. The S_{zz} stress contours corresponding to the through-thickness crack configuration for both designs are presented in *Figure 5.4 (a)* and *(b)*, respectively. For the surface crack configuration, the net section normal stress is generally quite low for both designs, certainly less than 3 ksi over much of the remaining ligament. Approaching the crack front, however, the normal stress increases sharply to much larger tensile values. The same trends are evident for the through-thickness crack configuration, the most apparent difference being that the maximum S_{zz} values along the crack front are nearly four times higher than the corresponding surface crack stresses. Large tensile normal stresses in the vicinity of the crack fronts are also indicative of the crack opening fracture mode. This is significant because the nodal displacement solutions along the crack faces will be used to evaluate the mode I stress intensity factors in a subsequent section.

5.2.2 Residual Stress Loading

For practical purposes, it is usually necessary to assume that high tensile residual stresses may be present at any position in and around a welded joint. The transverse residual stress component is the most detrimental when lack of penetration root defects might be present, since it acts normal to the weld root and thus tends to promote opening of any crack-like discontinuities in this location. As mentioned in the previous chapter, welding-induced transverse residual stresses may be as high as 50% of the yield strength of the material for highly restrained weldments. In a previous analysis of crack growth and fatigue life prediction in welded joints, Itoh *et al.* [31] assumed that the residual stresses do not diminish

under cyclic loading. This assumption simplifies the numerical analysis considerably but tends to overestimate the residual stress effect. It is important to recognize that welding-induced residual stresses are self-equilibrating and therefore redistribute as the crack propagates through the material. Moreover, when a given crack is fully open, the crack faces are stress free which, in order to maintain equilibrium, leads to the complete local relaxation of the transverse residual stress component adjacent to the crack faces. Using the same rationalization, through-thickness cracks are unable to support any tensile transverse residual stress in the material neighboring the crack faces. On the opposite side of the crack front (i.e. the remaining ligament), however, the transverse residual stresses may still be significant and hence must be considered when determining the fatigue crack growth rate.

In the present numerical investigation, the transverse residual stress component was assumed to be uniform through the thickness of the welded joint and equal to 50% of the yield strength of the material. For 20% cold worked AISI 316L austenitic stainless steel, the magnitude of the transverse residual stress component was taken to be 21.0 ksi. To evaluate the residual stress intensity factor, K_r, a small meshed region surrounding the crack plane (i.e. the yellow region in Figure 5.1) was used to model the geometry of the weldment. Uniform pressures acting along the edges of the models and directed away from the crack plane were employed to simulate the transverse residual stress component. Bearing in mind the earlier discussion regarding the relaxation of residual stress adjacent to the crack faces, pressures were only applied to the elements corresponding to the remaining ligament. Accordingly, the number of applied pressures decreases as the crack propagates through the material. For the initial crack front, pressures were applied over most of the cross-section since the remaining ligament-to-crack surface ratio is very high. For the through-thickness crack configuration,

however, pressures were applied only to those elements corresponding to the remaining ligament which, in this case, is only about one fifth the area of the crack surface.

A typical normal stress (S_{zz}) contour plot corresponding to one of the surface crack configurations (i.e. *crack front number 5*) for the new design is presented in *Figure 5.5 (a)*. As seen in the figure, the average normal stress over much of the remaining ligament is between 19 and 25 ksi (dark green contour band). This result was expected considering a uniform pressure of 21.0 ksi was applied to this region to simulate the welding-induced transverse residual stress. Approaching the crack, the normal stress increases rapidly to a maximum tensile value along the crack front while, at the same time, the crack surface remains stress free.

The S_{zz} stress contour plot corresponding to the through-thickness crack configuration for the new design is shown in *Figure 5.5 (b)*. Once again, the average normal stress over much of the remaining ligament is between 20 and 23 ksi (magenta contour band) as expected. The normal stress also increases upon nearing the crack front, but the maximum tensile stress is considerably lower ($\approx 40\%$) than that obtained for the previously illustrated surface crack configuration. Just as the former case, the material corresponding to the surface of the crack satisfies the stress free boundary condition.

In the following section, the stress intensity factors corresponding to each crack front are evaluated for the applied and residual stress loadings from the respective finite element displacement solutions. These values are then used to determine the effective stress intensity factor ranges, ΔK_{eff}, using the procedure outlined in Chapter 4. Once obtained, these results are used to determine the fatigue crack propagation rates and consequent life estimates for the original and new disc filter core pipe designs.
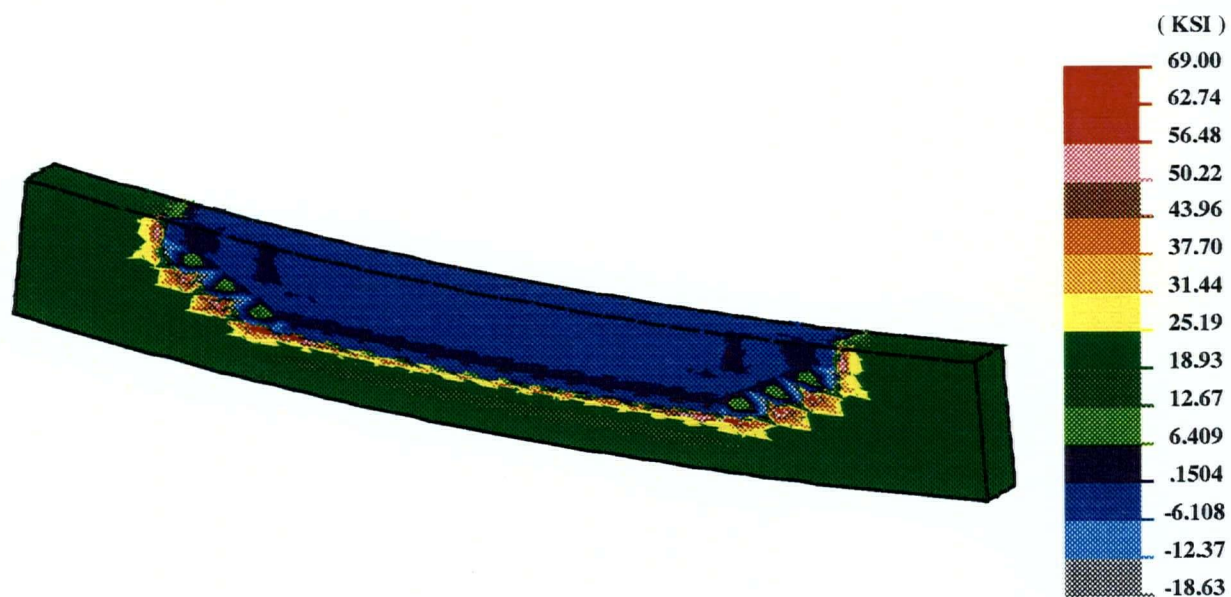
(a) **Crack Front No. 5**

(b) **Through-Thickness Crack**

Figure 5.5 S_{zz} **Stress Contours due to Residual Stresses - New Design**

5.3 Stress Intensity Factor Results

5.3.1 Applied Loading

Once the field solution had been obtained for both designs, the displacement extrapolation procedure was employed to evaluate the stress intensity factors at the crack front. The stress intensity factors, K_I, due to the applied loading for the original design are shown in *Figure 5.6 (a)* and *(b)*, corresponding to the surface and through-thickness crack configurations, respectively. The resulting stress intensity factors for the surface crack configurations increase as the crack propagates deeper into the material. This occurs primarily because the net section stress increases with the advancement of the crack. Furthermore, the average value determined for the through-thickness crack configuration is also more than double that obtained for the final surface crack configuration.

For the new core pipe design, analogous stress intensity factors corresponding to the surface and through-thickness crack configurations are illustrated in *Figure 5.7 (a)* and *(b)*, respectively. The resulting stress intensity factors exhibit the same general trends that were noted for the original design; however, the values determined for the new design are considerably lower than the previous results obtained for the original design.

As previously mentioned, the cyclic stresses on the outer shell of the core pipe are almost fully reversing. Therefore, the minimum stress intensity factors, occurring 180° around the circumference of the core pipe, can safely be assumed to be equal in magnitude to the maximum tensile values obtained in the present analysis. The resulting stress intensity factor ranges associated with both designs are summarized in *Figure 5.8*. The superiority of the new design is obvious with respect to the stress intensity factors due to the applied loading.
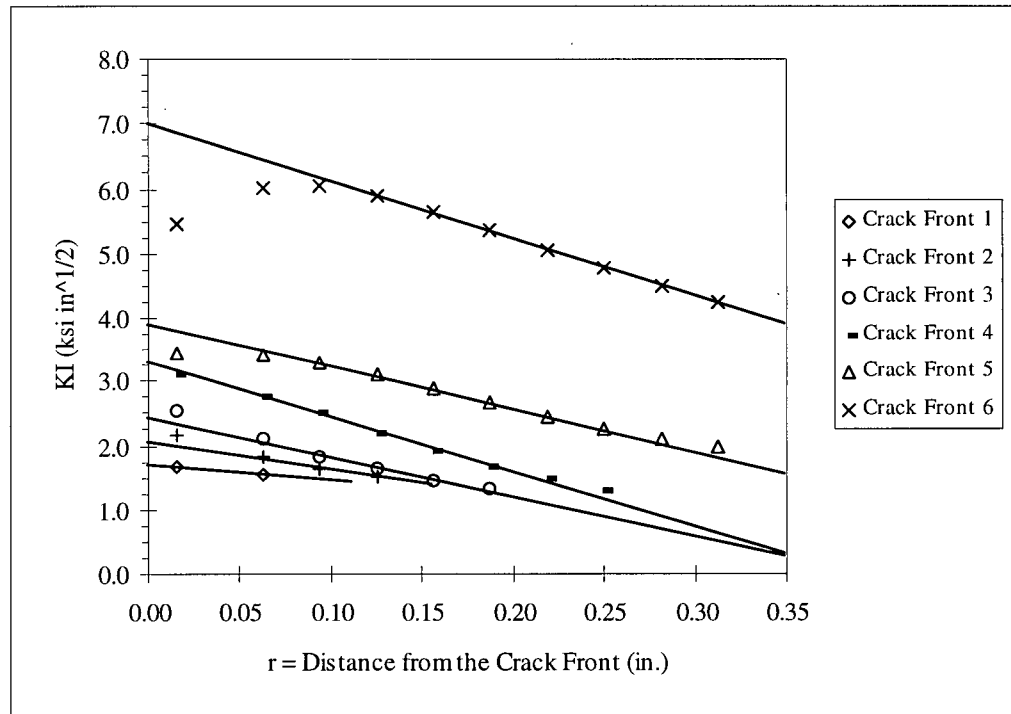
Figure 5.6 (a) K_I **due to the Applied Loading - Original Design (Surface Cracks)**

Figure 5.6 (b) K_I **due to Applied Loading - Original Design (Through-Thickness Crack)**
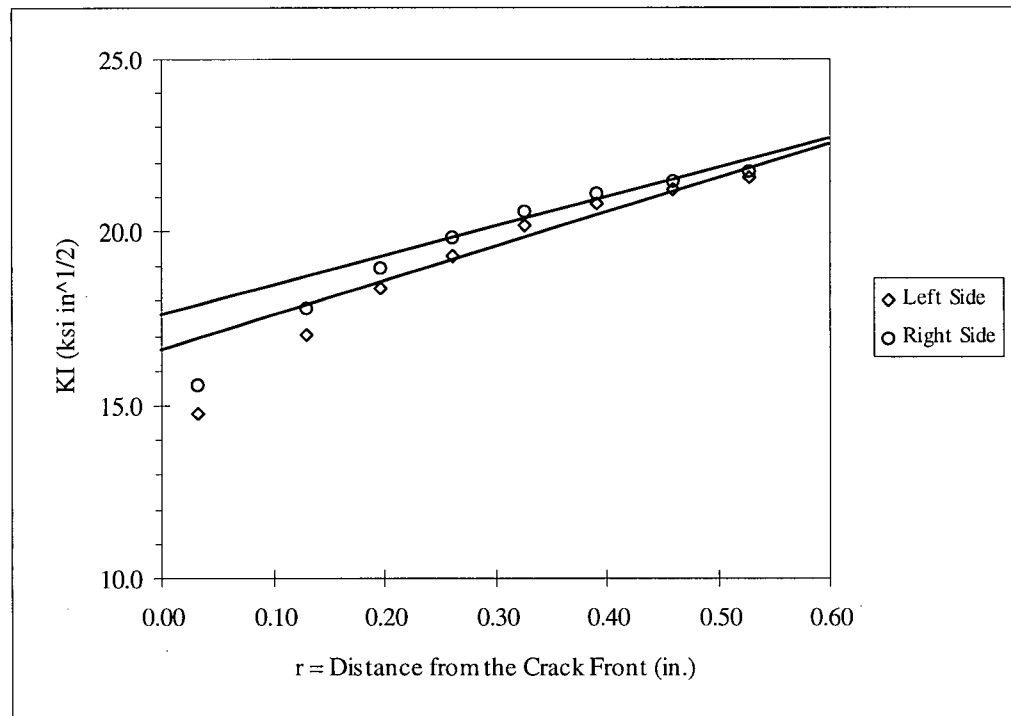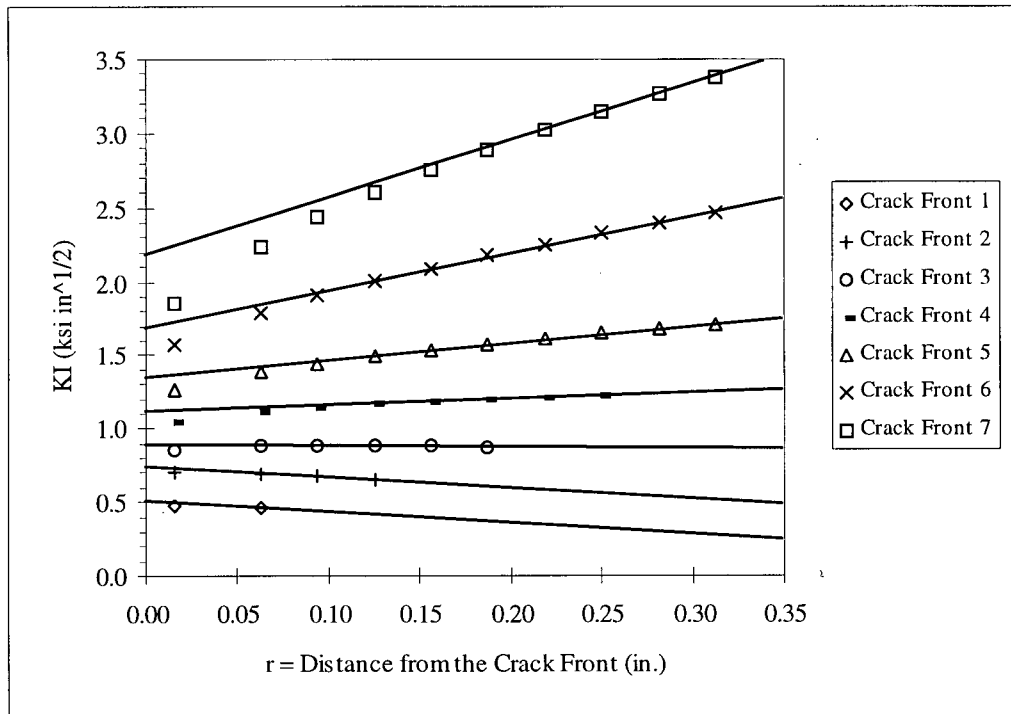
Figure 5.7 (a) K_I **due to the Applied Loading - New Design (Surface Cracks)**
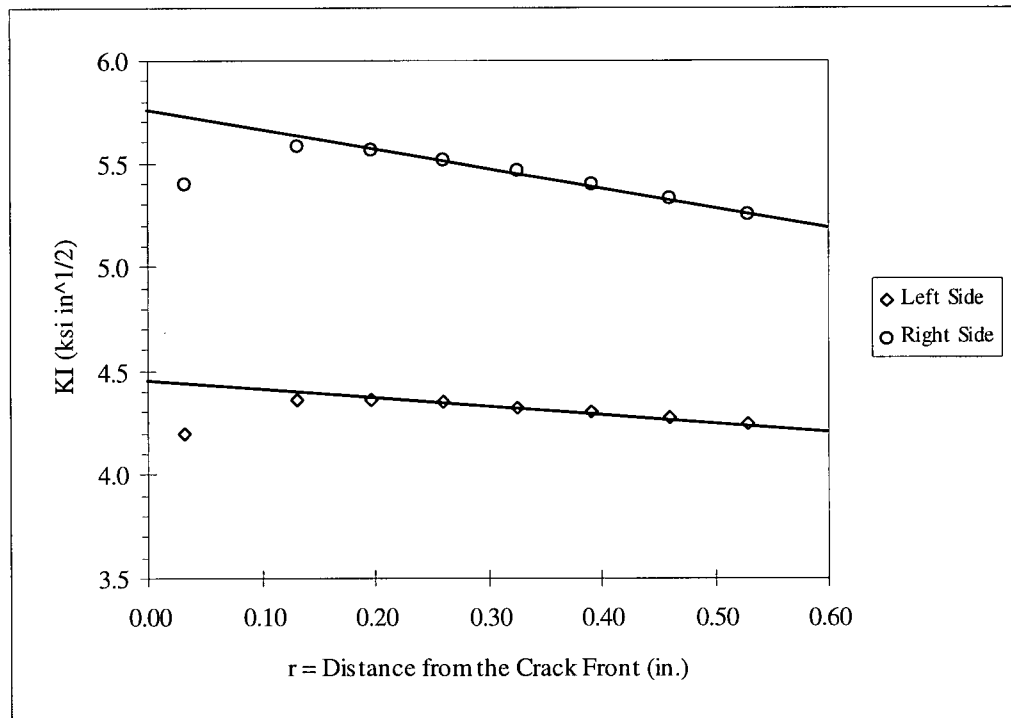
Figure 5.7 (b) K_I **due to the Applied Loading - New Design (Through-Thickness Crack)**
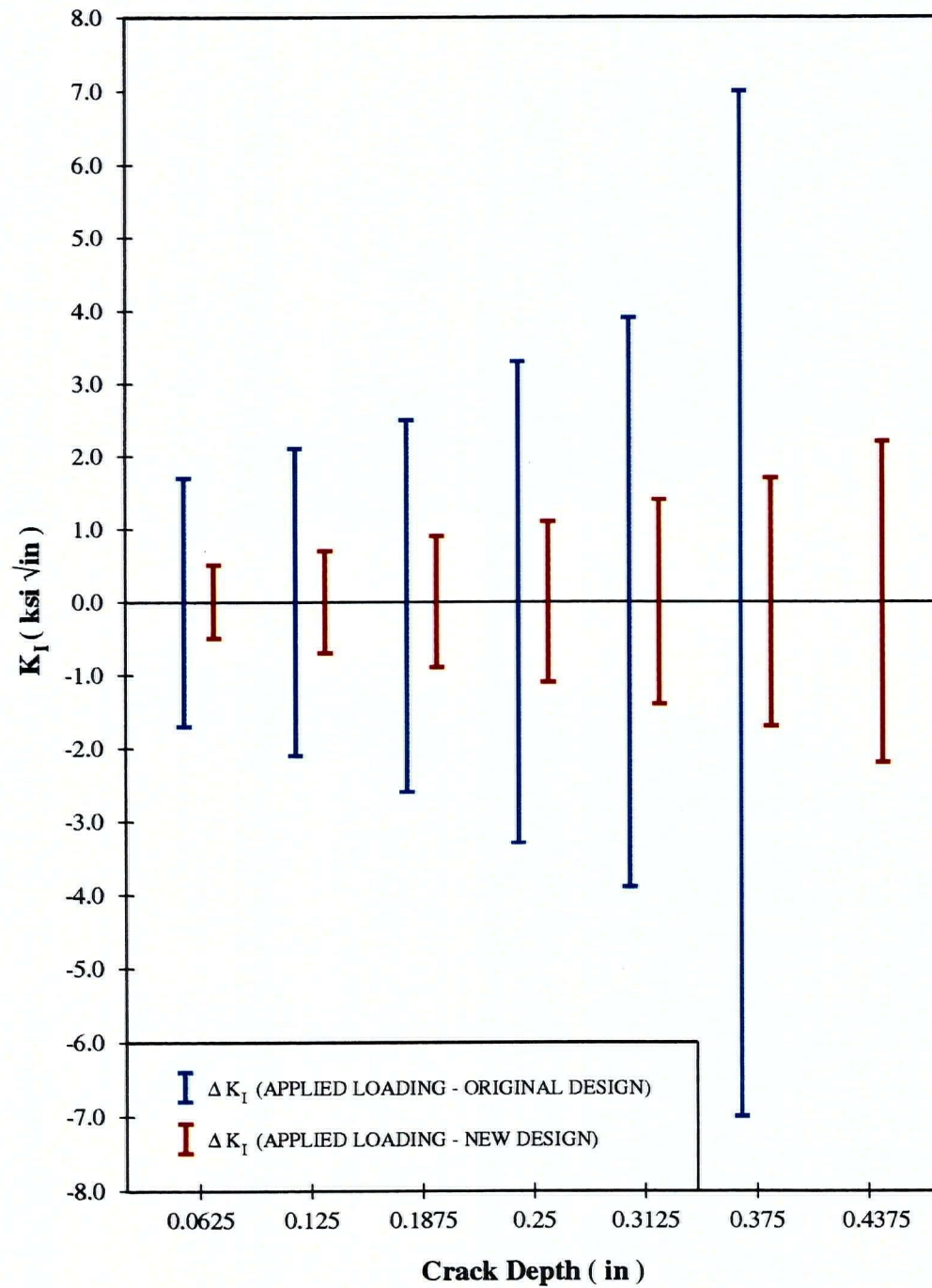
Figure 5.8 ΔK_I **vs. Crack Depth for the Original and New Design Configurations**

5.3.2 Residual Stress Loading

The stress intensity factors attributed to the assumed transverse residual stress loading for the new design are shown in *Figure 5.9 (a)* and *(b)*, corresponding to the surface and through-thickness crack configurations, respectively. The residual stress intensity factors, K_r, always remain positive due to the tensile residual stress, and there is a trend toward a decrease in the stress intensity factor as the crack propagates deeper into the material. The decreasing trend of crack tip stresses is caused by re-equilibration of the residual stresses as the crack grows [31]. At such time when the crack penetrates the outer surface of the shell, the crack assumes a through-thickness configuration which is influenced only by the transverse residual stresses remaining in the uncracked portion of the weld. The corresponding stress intensity factor is slightly lower than the value obtained for the final surface crack configuration.

Before proceeding to the next section, it should be mentioned that the foregoing residual stress intensity factors, calculated for the new design, were assumed to be equivalent for the original design. This assumption can be justified by noting that the state of residual stress around the crack front is primarily a function of the metallurgy, welding process, cooling rate and degree of local restraint; it depends to a much lesser extent on the actual geometry of the weldment. Furthermore, the considerable saving in computational cost was regarded to be more advantageous than a slight change in the final stress intensity factors.

5.3.3 Combined Loading

The actual loading condition imposed on the lack of penetration defect consists of the combined effects of both the applied loading and the loading caused by the welding induced transverse residual stresses.   Using the stress intensity factors evaluated in the previous two
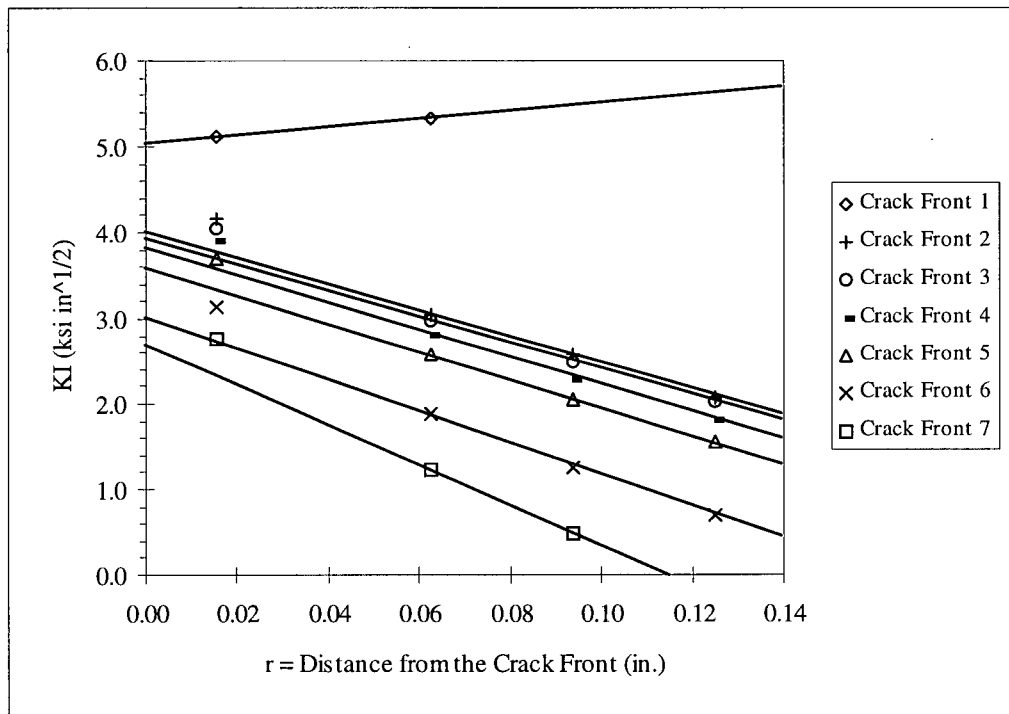
Figure 5.9 (a) K_I **due to Residual Stresses - New Design (Surface Cracks)**
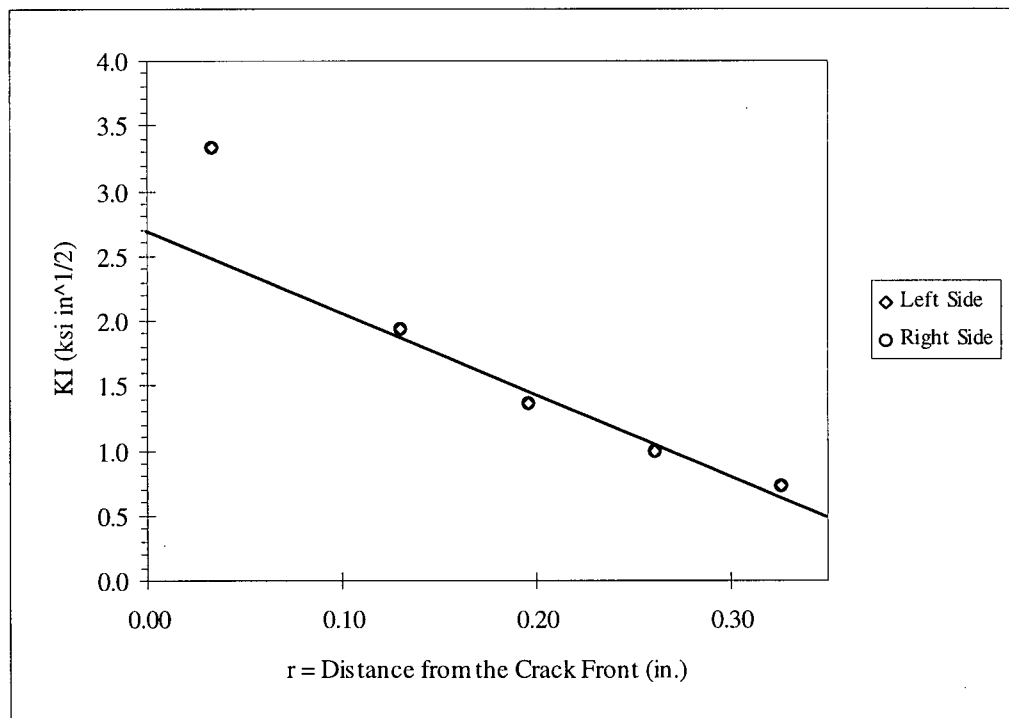
Figure 5.9 (b) K_I **due to Residual Stresses - New Design (Through-thickness Crack)**

sections, together with equations (4.15) and (4.16), the applied stress intensity factor range, ΔK, and the total stress ratio, R_r, were evaluated for each surface and through-thickness crack configuration. The resulting values are summarized in *Table 5.2 (a)* and *(b)*, for the original and new core pipe designs, respectively. Then, using equation (4.22) with an n-value equal to 1.14, the respective crack opening ratio, U, was calculated for each surface and through-thickness crack configuration. The final step in determining the effective stress intensity factor range, ΔK_{eff}, is accomplished by multiplying the stress intensity factor range by the corresponding crack opening ratio, in accordance with equation (4.19). The final results for each design are tabulated in *Table 5.2 (a)* and *(b)*.

Since the crack opening ratio is always less than or equal to unity, the *effective* stress intensity factor range shall always be a fraction of the stress intensity factor range. This may be illustrated by superimposing the effective stress intensity factor range (solid lines) over the corresponding stress intensity factor range (solid and dotted lines) for each of the surface crack configurations, as presented in *Figure 5.10*. It is also interesting to note that during the early stages of crack growth, when the residual stress intensity factor is comparable to the stress intensity factor range, the crack is assumed to be open for most of the load cycle. On the other hand, the effects of crack closure become more pronounced during the final stages of crack growth when the crack is assumed to be closed for a significant portion of the load cycle. These findings concur with the research done by Fukuda′ and Sugino [38], who found that welding residual stresses have a remarkable effect on the initial stages of fatigue crack growth. They also found that residual stresses in the neighborhood of the crack tip decrease with extension of a fatigue crack, resulting in a decrease from unity of the crack opening ratio.

Table 5.2 (a) Summary of Stress Intensity Factor Results

— Original Design —

Crack Front	$K_{min,app}$ (ksi√in)	$K_{max,app}$ (ksi√in)	ΔK^1 (ksi√in)	K_{res}^2 (ksi√in)	K_{min} (ksi√in)	K_{max} (ksi√in)	R_r^3	U	ΔK_{eff} (ksi√in)
1	-1.70	**1.70**[4]	3.40	**5.05**	3.35	6.75	0.50	0.99	3.37
2	-2.10	**2.10**	4.20	**4.00**	1.90	6.10	0.31	0.77	3.22
3	-2.45	**2.45**	4.90	**3.90**	1.45	6.35	0.23	0.70	3.44
4	-3.30	**3.30**	6.60	**3.79**	0.49	7.09	0.07	0.61	4.02
5	-3.87	**3.87**	7.47	**3.60**	-0.27	7.47	0	0.58	4.31
6	-7.00	**7.00**	10.02	**3.02**	-3.98	10.02	0	0.58	5.78
7[5]	-17.20	**17.20**	19.90	**2.70**	-14.50	19.90	0	0.58	11.48

Note 1: $\Delta K = K_{max,app} - K_{min,app}$ when $K_{res} + K_{min,app} \geq 0$
$\Delta K = K_{max,app} + K_{res}$ when $K_{res} + K_{min,app} < 0$
Note 2: K_{res} values were assumed to be equal to the corresponding values obtained for the new design configuration.
Note 3: $R_r = 0$ when $K_{min} \leq 0$; otherwise $R_r = K_{min} / K_{max}$.
Note 4: Bold face numbers were evaluated from the appropriate finite element solution.
Note 5: Crack Front 7 corresponds to the final through-thickness crack configuration.

Table 5.2 (b) Summary of Stress Intensity Factor Results

— New Design —

Crack Front	$K_{min,app}$ (ksi√in)	$K_{max,app}$ (ksi√in)	ΔK^1 (ksi√in)	K_{res} (ksi√in)	K_{min} (ksi√in)	K_{max} (ksi√in)	R_r^2	U	ΔK_{eff} (ksi√in)
1	-0.51	**0.51**[3]	1.02	**5.05**	4.54	5.56	0.82	1	1.02
2	-0.74	**0.74**	1.48	**4.00**	3.26	4.74	0.69	1	1.48
3	-0.90	**0.90**	1.80	**3.90**	3.00	4.80	0.63	1	1.80
4	-1.12	**1.12**	2.24	**3.79**	2.67	4.91	0.54	1	2.24
5	-1.36	**1.36**	2.72	**3.60**	2.24	4.96	0.45	0.92	2.51
6	-1.70	**1.70**	3.40	**3.02**	1.32	4.72	0.28	0.74	2.52
7	-2.17	**2.17**	4.34	**2.75**	0.58	4.92	0.12	0.63	2.75
8[4]	-5.12	**5.12**	7.82	**2.70**	-2.42	7.82	0[4]	0.58	4.51

Note 1: $\Delta K = K_{max,app} - K_{min,app}$ when $K_{res} + K_{min,app} \geq 0$
$\Delta K = K_{max,app} + K_{res}$ when $K_{res} + K_{min,app} < 0$
Note 2: $R_r = 0$ when $K_{min} \leq 0$; otherwise $R_r = K_{min} / K_{max}$.
Note 3: Bold face numbers were evaluated from the appropriate finite element solution.
Note 4: Crack Front 8 corresponds to the final through-thickness crack configuration.
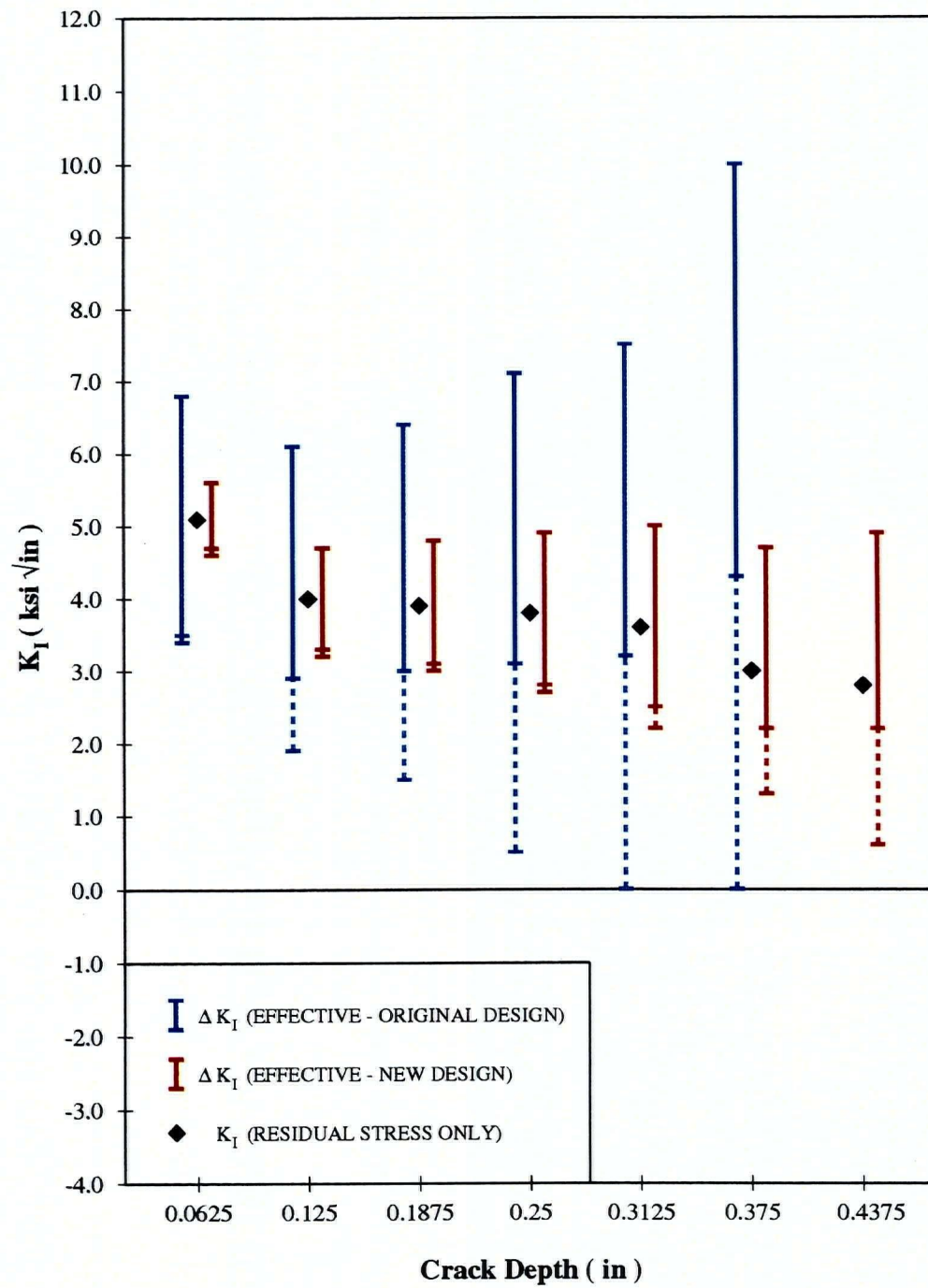
Figure 5.10 ΔK_{eff} **vs. Crack Depth for the Original and New Designs**

5.4 Fatigue Crack Propagation Analysis and Results

In the final section of this chapter, the effective stress intensity factor ranges are used to determine the fatigue crack propagation rates and ultimately the fatigue life of the two core pipe designs. This information will serve as a means of comparing the two designs so that an assessment may be made as to whether or not the proposed design changes will be effective.

It is a well-recognized fact that fatigue properties are altered by the presence of a corrosive environment. When calculating fatigue crack propagation rates in aggressive environments, it is therefore necessary to obtain data (i.e. *da/dN* vs. ΔK curves) for the particular material-environment combination under consideration. Unfortunately, the lack of fatigue data for stainless steels in simulated paper machine white-water solutions represents a genuine problem. Since corrosion processes are usually strongly time-dependent, testing frequencies lower than 1 Hz must be used in order to see an effect of a corrosive environment on fatigue [90]. This tends to severely prolong the corrosion fatigue testing period which makes such tests so expensive that information of this nature typically remains proprietary. In many cases, it may be necessary to assume fatigue crack propagation rates based on the best available information for a particular set of conditions. For practical purposes, it is also necessary to assume that high tensile residual stresses will be present at any position in and around a welded joint, so data obtained under high tensile mean stress conditions or under tensile loading from stress relieved joints are of most relevance.

In the present analysis, corrosion fatigue data available for 316L stainless steel [90] in air (at room temperature) and in 3% NaCl (at 80°C), as shown in *Figure 5.11*, was used to determine the fatigue crack propagation rates for the core pipe circumferential weldment. These fatigue crack propagation results for commercial plate, solution annealed 316L were

performed at 0.2 Hz in 3% NaCl and at 0.8 Hz in air, with mean stress ratio $R = 0.5$ in both cases. The crack propagation results may be represented by the following two equations:

$$da/dN = 8.357 \times 10^{-11} (\Delta K)^{3.516} \qquad \text{in air @ room temperature} \qquad (5.1)$$

$$da/dN = 1.491 \times 10^{-9} (\Delta K)^{2.709} \qquad \text{in 3\% NaCl @ 80°C} \qquad (5.2)$$

which are represented by the best-fit lines in *Figure 5.11*. These equations may not be applied directly to the effective stress intensity factor ranges, ΔK_{eff}, as determined in the previous section because the equations are functions of the stress intensity factor range, ΔK. Consequently, it is necessary to convert the available data into crack growth rates corresponding to the effective stress intensity factor range. As discussed in the previous chapter, this may be accomplished using equation (4.22) for the crack opening ratio, U, together with the R-ratio that was used during the fatigue crack propagation testing. The ΔK values from the experimental data may then be converted to ΔK_{eff} values by multiplying by the resulting U value. Using $R = 0.5$ in equation (4.22), the resulting crack opening ratio for the test conditions is $U = 1.0$. In other words, the mean stress was sufficiently high to prevent any crack closure during the fatigue crack propagation testing, and ΔK_{eff} may simply be substituted for ΔK in equations (5.1) and (5.2).

The fatigue crack propagation rates corresponding to each crack configuration for the original and new core pipe designs are shown in *Figure 5.12* where the new design appears to perform considerably better than the original design. The difference between the crack propagation rates in air and in 3% NaCl are more pronounced at the lower effective stress intensity factor ranges. For example, at $\Delta K_{eff} = 1.0$ ksi√in, the fatigue crack propagation rate in 3% NaCl is more than 10 times greater than the corresponding rate in air; this will have a significant impact on the early stages of crack growth.
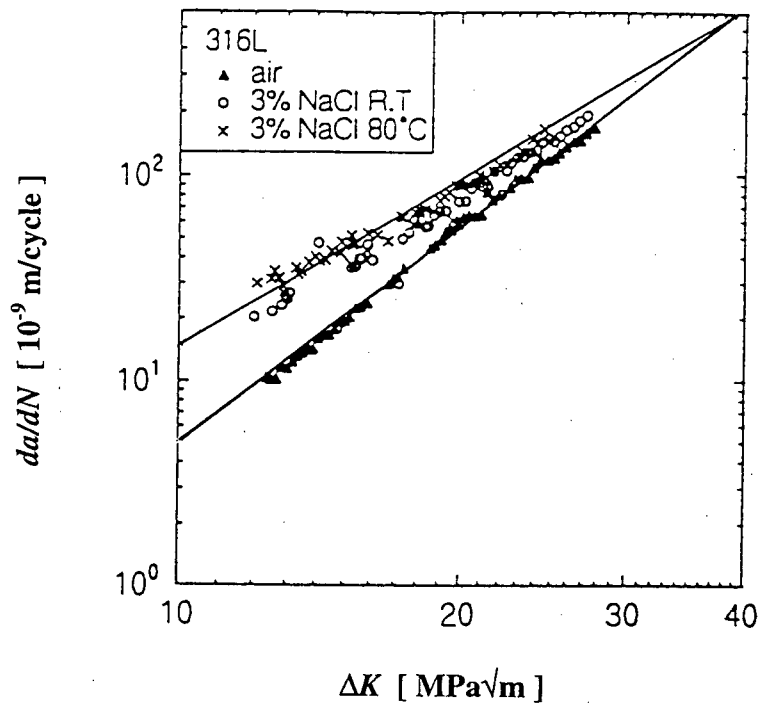
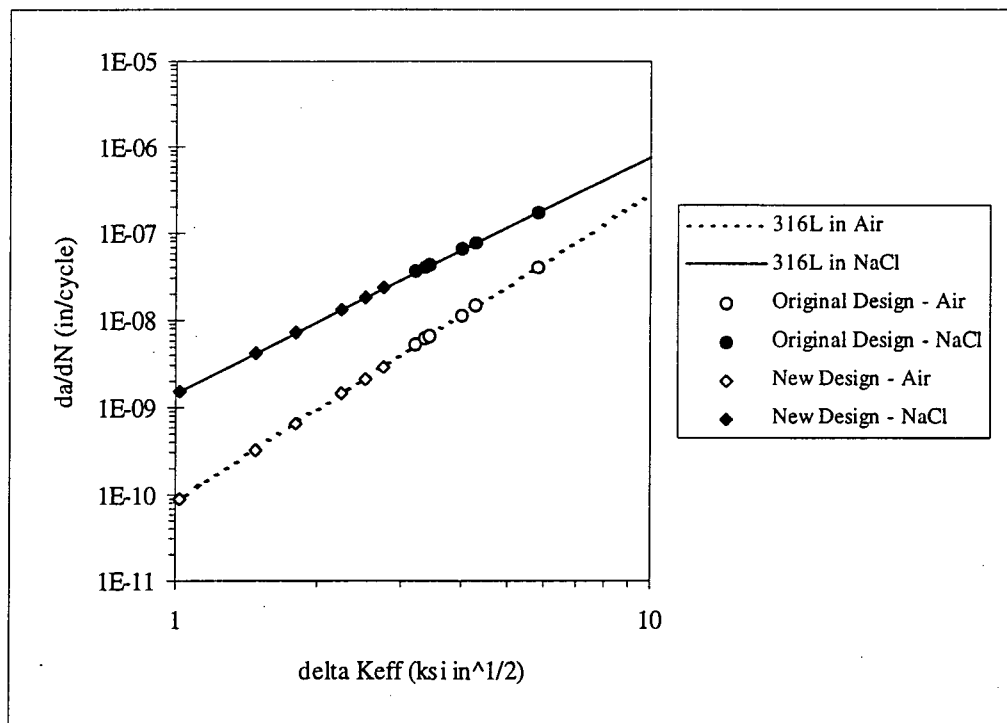*Figure 5.11* Fatigue Crack Propagation Test Data for 316L Stainless Steel [90]

Figure 5.12 Fatigue Crack Propagation Rates for Both Designs in Air and NaCl

The final step in the present numerical study is to predict the fatigue crack propagation life of the disc filter core pipe. For this purpose, failure is defined at such time when the lack of penetration defect has propagated completely through the material thickness and assumed a through-thickness crack configuration. This is not likely to coincide with catastrophic equipment failure; in fact, a unit may continue to operate for a considerable length of the time with numerous cracks visible on the outer surface of the shell.

The number of load cycles for a given increment of crack depth was calculated using equation (4.23) together with the average value of the crack propagation rate over the increment. The results are presented in *Table 5.3 (a)* and *(b)*, for the original and new designs, respectively. The total number of cycles corresponding to the fatigue crack propagation life, as defined above, is determined by summing the number of cycles for each increment of crack growth. The fatigue crack propagation life is then determined by dividing the total number of cycles by the operating frequency, which is taken to be 1.5 rpm. The final results are given in *Table 5.3*.

The superiority of the new core pipe design over the original Ingersoll-Rand design is now clearly obvious. Comparing the fatigue crack propagation life in air of the original design to the actual life of the equipment (approximately 5 years), it may safely be concluded that pure mechanical fatigue would not accurately describe the failure mechanism. Furthermore, the fatigue crack propagation life determined from corrosion-fatigue data is remarkably close to the actual equipment life. It may also be concluded that the proposed design changes have resolved the concerns associated with the circumferential weld.

Although the through-thickness crack configuration occurs, by definition, after failure, it may still be useful to know the predicted crack growth rates from an operations point of view.

Table 5.3 (a) **Fatigue Crack Propagation Results - Original Design**

Crack Front	ΔK_{eff} (ksi√ in)	Air		NaCl @ 80°C	
		da/dN (in/cycle)	N_i (10^6 cycles)	*da/dN* (in/cycle)	N_i (10^6 cycles)
1	3.37	6.02E-09	11.22	4.02E-08	1.65
2	3.22	5.12E-09	10.82	3.55E-08	1.60
3	3.44	6.44E-09	7.12	4.24E-08	1.17
4	4.02	1.11E-08	4.93	6.45E-08	0.88
5	4.31	1.42E-08	2.31	7.81E-08	0.50
6	5.78	4.00E-08	1.56	1.73E-07	0.36
Total Cycles (10^6)			37.97		6.16
Rpm			1.5		1.5
Cycles/day			2,160		2,160
FCP Life (days)			17,579		2,852
FCP Life (years)			48		8

Table 5.3 (b) **Fatigue Crack Propagation Results - New Design**

Crack Front	ΔK_{eff} (ksi√ in)	Air		NaCl @ 80°C	
		da/dN (in/cycle)	N_i (10^6 cycles)	*da/dN* (in/cycle)	N_i (10^6 cycles)
1	1.02	8.69E-11	296.73	1.57E-09	21.24
2	1.48	3.32E-10	126.04	4.31E-09	10.74
3	1.80	6.60E-10	59.98	7.33E-09	6.07
4	2.24	1.42E-08	35.17	1.33E-08	3.99
5	2.51	2.13E-09	29.20	1.81E-08	3.45
6	2.52	2.15E-09	24.59	1.82E-08	3.02
7	2.75	2.93E-09	21.31	2.31E-08	2.70
Total Cycles (10^6)			593.03		51.21
Rpm			1.5		1.5
Cycles/day			2,160		2,160
FCP Life (days)			274,551		23,708
FCP Life (years)			752		65

Using the effective stress intensity factor ranges given in *Table 5.2*, fatigue crack growth rates based on an operating speed of 1.5 rpm were determined for both designs. The results are shown in *Table 5.4*. Again, the rates for the new design are significantly lower than those determined for the original design.

Table 5.4 **Through-Thickness Fatigue Crack Propagation Results**

Design	ΔK_{eff} (ksi√ in)	Air		NaCl @ 80°C	
		da/dN (in/cycle)	*da/dN* (in/year)	*da/dN* (in/cycle)	*da/dN* (in/year)
Original	11.48	4.45E-07	0.35	1.11E-06	0.88
New	4.51	1.67E-08	0.01	8.82E-08	0.07

CHAPTER 6

CONCLUSIONS

The operation of rotary vacuum disc filters to remove fibers from pulp and paper machine white waters for thickening or save-all applications was summarized in the introductory chapter. Concerns regarding corrosion associated with ongoing programs to close-up mill white water systems by way of increased recycle were also discussed. The severe weld cracking problem experienced by one of Ingersoll-Rand's type 316L stainless steel disc filters was then introduced.

In the second chapter, the subjects of environmentally induced cracking and problematic weld discontinuities were reviewed. The main characteristics of several environmentally induced cracking mechanisms (i.e. stress corrosion cracking, corrosion fatigue cracking and hydrogen embrittlement) were outlined. A basic overview of welding flaws or defects such as incomplete fusion, incomplete joint penetration, cracks, undercut and porosity was also given. A thorough analysis (including visual and metallographic examination, photo microscopy and scanning electron microscopy) was then performed on the core pipe weld failures. Specimens were removed from three different circumferential weld seams which exhibited hairline cracks of varying degrees of severity. Based on the brittle mode of fracture, macroscopic beach marks, ratchet marks and striations on the fracture surfaces, combined with substantial crevice corrosion at the weld root, the circumferential weld failures which occurred in Ingersoll-Rand's disc filter core pipe were caused by corrosion fatigue emanating from lack of penetration defects at the weld root.

The application of finite element analysis to the static design of mechanical equipment and associated boundary condition incompatibilities were the focus of the third chapter. A new finite element sub-modeling technique was developed which facilitates the transfer of appropriate boundary conditions from a full (shell element) model to a refined (shell or solid element) sub-model. The proposed technique places very few demands on the final sub-model leaving the user with complete flexibility with respect to the number and location of boundary nodes. Shell and solid element sub-modeling examples were then presented which clearly demonstrated the successful implementation of this sub-modeling technique. In both cases, the numerical stress results obtained for the final sub-models were less than 10 percent different from the corresponding results obtained in the full (shell element) model analysis.

The discussion in the fourth chapter was concerned with various aspects related to fracture and fatigue of welded joints. The progressive development of residual stress during welding was illustrated, and its detrimental effect on the fatigue life of welded joints was discussed. The application of linear elastic fracture mechanics concepts to determine the fatigue life of welded joints was then introduced. A brief overview was given for a number of different techniques which may be employed to numerically evaluate the stress intensity factors from the field solutions for mode I (opening) cracks. In particular, the displacement method, stress method, nodal force method, line integral (energy) method and the virtual crack extension method were all considered. Numerical examples were presented for both through-thickness and semi-elliptical crack configurations to demonstrate the displacement method. The concept of fatigue crack closure was also thoroughly investigated. This phenomenon is particularly important for cyclic service loads which are fully reversing, as in the case of the disc filter core pipe, and must be considered to obtain accurate predictions of

fatigue crack propagation rates. A step-by-step method for predicting the fatigue crack propagation rate of crack-like defects in welded joints was then given.

In the fifth chapter, the disc filter core pipe was the subject of a numerical study to determine life estimates for the equipment in both air and simulated white water environments. An exhaustive search for the fatigue crack propagation rates of austenitic stainless steels in white water environments revealed that such information is not available in the literature. A considerable amount of experimental research is therefore still required to develop a broad database of this type of material property information. Consequently, crack propagation rates for 316L in 3% NaCl at 80°C were used as an alternative.

Using singularity elements (i.e. isoparametric elements with nodes shifted to the quarter point position) around the crack front, the displacement extrapolation technique was then applied to accurately evaluate the stress intensity factors for a number of semi-elliptical and through-thickness cracks corresponding to both applied and residual stress loads in the core pipe. A crack closure model was used to determine the effective stress intensity factor ranges for a series of crack-advance fronts, and Paris' law was employed to determine the crack propagation rates and resulting fatigue lives for two different core pipe designs.

The new design, developed through a cooperative project undertaken by Tristar Industries Ltd. and UBC's Finite Element Analysis and Research Lab, was found to be clearly superior to the original Ingersoll-Rand design requiring more than eight times more cycles to failure. In the NaCl environment, the fatigue crack propagation life for the new design was predicted to be 65 years compared to an 8 year estimate for the original design.

In the new design, the outer shell of the core pipe is constructed from cylinders of uniform thickness compared to rings of alternating material thickness used to fabricate the

original Ingersoll-Rand core pipes. This design change eliminated the stress concentration in the circumferential weld seams and is largely responsible for the significant improvement in the service life of the equipment. In the new design, the uniform thickness outer shell may also be fabricated in sections up to 2 meters in length thus reducing the total number of circumferential weld seams. This results in considerable savings in both time and cost to manufacture the disc filter core pipe.

BIBLIOGRAPHY

[1]   **G.A. Smook**, *Handbook for Pulp and Paper Technologists*, Vancouver: Angus Wilde Publications, 1992.

[2]   **R.A. Yeske**, "Corrosion in the Pulp and Paper Industry," IPC Technical Paper Series, Number 192, 1986.

[3]   **J.R. Davis (Davis and Associates)**, *ASM Specialty Handbook: Stainless Steels*, Metals Park, Ohio, American Society for Metals, 1994.

[4]   **D.A. Wensley**, "Localized Corrosion Resistance of Stainless Steels in White Water," *Materials Performance*, Vol. 28, No. 11, pp. 68-71, 1989.

[5]   **Ingersoll-Rand, Impco Division**, *Technical Bulletin Disc Filter 2-2-52/1B*, November, 1983.

[6]   **Ingersoll-Rand, Impco Division**, *Instruction Manual for the 12 Foot Diameter Impco Disc Filter*, November, 1983.

[7]   **R.S. Charlton, D.W. Christie and D.C. Reid**, "Stress Corrosion Cracking or Corrosion Fatigue," in *TAPPI Engineering Conference*, 1993.

[8]   **D.R.H. Jones**, Engineering Materials 3, Materials Failure Analysis, Pergamon Press, 1993.

[9]   **M.G. Dawes**, "Application of Fracture Mechanics to Ductile and Brittle Fracture in Welded Structures," in *The Assessment of Cracked Components by Fracture Mechanics*, EGF Publication 4 (Ed: L.H. Larsson), Mechanical Engineering Publications Limited, London, 1989, pp. 211-232.

[10]   **ANSI/AWS A3.0**, "Standard Welding Terms and Definitions," American Welding Society, Miami, Florida.

[11]   **J.C. Meyers**, "Problematic Weld Discontinuities and Their Prevention," *Welding Journal*, June, pp. 45-47, 1995.

[12]   **G.F. Carey**, "A Mesh-Refinement Scheme for Finite Element Computations," *Computer Methods in Applied Mechanics and Engineering*, Vol. 7, pp. 93-105, 1976.

[13]   **D.J. Schwartz**, "Practical Analysis of Stress Raisers in Solid Structures," in *4th International Conference on Vehicle Structural Mechanics*, SAE (Warrendale, PA), November, 1981.

[14]   **I. Hirai, B.P. Wang, and W.D. Pilkey**, "An Efficient Zooming Method for Finite
       Element Analysis," *International Journal for Numerical Methods in Engineering*,
       Vol. 20, pp. 1671-1683, 1984.

[15]   **C.C. Jara-Almonte and C.E. Knight**, "The Specified Boundary Stiffness/Force,
       SBSF, Method for Finite Element Subregion Analysis," *International Journal for
       Numerical Methods in Engineering*, Vol. 26, pp. 1567-1578, 1988.

[16]   ANSYS User's Manual, Swanson Analysis Systems Inc., Version 93.0, 1993.

[17]   NISA II User's Manual, Engineering Mechanics Research Corporation, Troy,
       Michigan, Version 92.0, 1992.

[18]   DISPLAY III User's Manual, Engineering Mechanics Research Corporation, Troy,
       Michigan, Version 92.0, 1992.

[19]   **K. Masubuchi**, "Models of Stresses and Deformations Due to Welding - A Review,"
       in *Modeling of Casting and Welding Processes*, Metallurgy Society of AIME, 1981,
       pp. 223.

[20]   **K. Easterling**, *Introduction to the Physical Metallurgy of Welding*, Oxford:
       Butterworth-Heinemann Ltd., 1992.

[21]   **M.G. Dawes**, "Application of Fracture Mechanics to Ductile and Brittle Fracture in
       Welded Structures," in *The Assessment of Cracked Components by Fracture
       Mechanics*, EGF Publication 4 (Ed: L.H. Larsson), Mechanical Engineering
       Publications Limited, London, 1989, pp. 211-232.

[22]   **Y.W. Shi, B.Y. Chen and J.X. Zhang**, "Effects of Welding Residual Stresses on
       Fatigue Crack Growth Behavior in Butt Welds of a Pipeline Steel," *Engineering
       Fracture Mechanics*, Vol. 36, No. 6, pp. 893-902, 1990.

[23]   **S.J. Maddox**, "Fatigue Crack Propagation Data Obtained from Parent Plate, Weld
       Metal and HAZ in Structural Steel," Research Report E/48/72, The Welding Institute,
       September, 1972.

[24]   **T.N. Nguyen and M.A. Wahab**, "The Effect of Residual Stresses on Fatigue of Butt
       Joints," *Welding Journal (Research Supplement)*, February, pp. 55s-61s, 1996.

[25]   **Y.-L. Lu**, "A Practical Procedure for Evaluating SIFs Along Fronts of Semi-Elliptical
       Surface Cracks at Weld Toes in Complex Stress Fields," *International Journal of
       Fatigue*, Vol. 18, No. 2, pp. 127-135, 1996.

[26]   **Y.-L. Lu**, "Crack Aspect Development Curves and Fatigue Life Prediction for
       Surface Cracks at Weld Toes in the Presence of Residual Stress," *International
       Journal of Fatigue*, Vol. 17 No. 8, pp. 551-557, 1995.

[27]   **C. Makabe, H. Kaneshiro, S. Nishida and H. Sakihama**, "A Consideration of Evaluation of Fatigue Crack Propagation Rate From Stress Intensity Factor Range," *Journal of Testing and Evaluation*, JTEVA, Vol. 23, No. 3, May, pp. 153-159, 1995.

[28]   **Y. Sumi**, "Computational Crack Path Prediction for Brittle Fracture in Welding Residual Stress Fields," *International Journal of Fracture*, Vol. 44, pp. 189-207, 1990.

[29]   **M. Beghini and L. Bertini**, "Fatigue Crack Propagation Through Residual Stress Fields with Closure Phenomena," *Engineering Fracture Mechanics*, Vol. 36, No. 3, pp. 379-387, 1990.

[30]   **J.F. Flavenot and N. Skalli**, "A Comparison of Multiaxial Fatigue Criteria Incorporating Residual Stress Effects," in *Biaxial and Multiaxial Fatigue*, EGF Publication 3 (Eds: M.W. Brown and K.J. Miller), Mechanical Engineering Publications Limited, London, 1989, pp. 437-457.

[31]   **Y.Z. Itoh, S. Suruga and H. Kashiwaya**, "Prediction of Fatigue Crack Growth Rate in Welding Residual Stress Field," *Engineering Fracture Mechanics*, Vol. 33, No. 3, pp. 397-407, 1989.

[32]   **J.G. Wylde**, "The Influence of Residual Stresses on the Fatigue Design of Welded Steel Structures," in *Residual Stress in Design, Process and Materials Selection: Proceedings of ASM's Conference on Residual Stress* (Cincinnati, Ohio, USA), April 27-29, 1987, pp. 85-95.

[33]   **S.J. Maddox**, "Fatigue Analysis of Welded Joints using Fracture Mechanics," in *Fatigue Life: Analysis and Prediction, Proceedings of the Fatigue Program and Related Papers presented at the International Conference and Exposition on Fatigue, Corrosion Cracking, Fracture Mechanics and Failure Analysis* (Salt Lake City, Utah, USA), December 2-6, 1985, pp. 155-166.

[34]   **R. Boler**, "Influence of Residual Stress on Fracture of Weldments," in *The Mechanism of Fracture, Proceedings of the Fracture-Mechanics Program and Related Papers presented at the International Conference and Exposition on Fatigue, Corrosion Cracking, Fracture Mechanics and Failure Analysis* (Salt Lake City, Utah, USA), December 2-6, 1985, pp. 239-244.

[35]   **Y. Verreman, Jacques Masounave and J.-P. Bailon**, "Fatigue Life Prediction of Welded Joints Using the Effective Stress Intensity Factor Range," in *The Mechanism of Fracture, Proceedings of the Fracture-Mechanics Program and Related Papers presented at the International Conference and Exposition on Fatigue, Corrosion Cracking, Fracture Mechanics and Failure Analysis* (Salt Lake City, Utah, USA), December 2-6, 1985, pp. 245-253.

[36] **A.P. Parker**, "Stress Intensity Factors, Crack Profiles, and Fatigue Crack Growth Rates in Residual Stress Fields," in *Residual Stress Effects in Fatigue, ASTM STP 776*, American Society for Testing and Materials, 1982, pp. 13-31.

[37] **D.V. Nelson**, "Effects of Residual Stress on Fatigue Crack Propagation," in *Residual Stress Effects in Fatigue, ASTM STP 776*, American Society for Testing and Materials, 1982, pp. 172-194.

[38] **S. Fukuda and M. Sugino**, "A Numerical Study of the Effect of Welding Residual Stress Upon Fatigue Crack Propagation with Attention Paid to the Phenomenon of Crack Opening and Closure," in *Numerical Methods in Fracture Mechanics: Proceedings of the Second International Conference* (Swansea, U.K.), July 7-11, 1980, pp. 615-629.

[39] **G. Glinka**, "Effect of Residual Stresses on Fatigue Crack Growth in Steel Weldments Under Constant and Variable Amplitude Loads," in *Fracture Mechanics, ASTM STP 677*, American Society for Testing and Materials, 1979, pp. 198-214.

[40] **T.R. Gurney**, *Fatigue of Welded Structures*, Cambridge: Cambridge University Press, 1980.

[41] **J. Schijve**, "Four Lectures on Fatigue Crack Growth," *Engineering Fracture Mechanics*, Vol. 11, pp. 167-221, 1979.

[42] **W. Elber**, "The Significance of Fatigue Crack Closure," in *Damage Tolerance in Aircraft Structures, ASTM STP 486*, American Society for Testing and Materials, 1971, pp. 230-242.

[43] **K. Hellan**, *Introduction to Fracture Mechanics*, New York: McGraw-Hill Publishing Company, 1984.

[44] **H.M. Westergaard**, "Bearing Pressures and Cracks," *Journal of Applied Mechanics*, Vol. 6, pp. 49-53, 1939.

[45] **G.R. Irwin**, "Analysis of Stresses and Strains Near the End of a Crack Traversing a Plate," *Journal of Applied Mechanics*, Vol. 24, pp. 361-364, 1957.

[46] **D.M. Tracey**, "Finite Element for Determination of Crack Tip Elastic Stress Intensity Factors," *Engineering Fracture Mechanics*, Vol. 3, pp. 255-265, 1971.

[47] **F.A. McClintoch and G.R. Irwin**, "Plasticity Aspects of Fracture Mechanics," in *Fracture Toughness Testing and Its Applications, ASTM STP 381*, American Society for Testing and Materials, 1971, pp. 84-113.

[48] **D. Broek**, *Elementary Engineering Fracture Mechanics*, Dordrecht: Martinus Nijhoff Publishers, 1987.

[49]   W.G. Clark, Jr., "Applicability of the K_{ISCC} Concept to Very Small Defects," in *Cracks and Fracture, ASTM STP 601*, American Society for Testing and Materials, 1976, pp. 138-153.

[50]   F.J. Heyman, "A Review of the Use of Isoparametric Finite Elements for Fracture Mechanics," in *Proceedings of the First National Conference on Fracture* (Johannesburg, South Africa), November 7-9, 1979, pp. 371-387.

[51]   H. Liebowitz and E.T. Moyer, Jr., "Finite Element Methods in Fracture Mechanics," *Computers and Structures*, Vol. 31, pp. 1-9, 1989.

[52]   G.P. Anderson, V.C. Ruggles and G.S. Stibor, "Use of Finite Element Computer Programs in Fracture Mechanics," *International Journal of Fracture Mechanics*, Vol. 7, pp. 63-75, 1971.

[53]   D.F. Mowbray, "A Note On the Finite Element Method in Linear Fracture Mechanics," *Engineering Fracture Mechanics*, Vol. 3, pp. 173-176, 1970.

[54]   S.E. Benzley, "Representation of Singularities with Isoparametric Finite Elements," *International Journal for Numerical Methods in Engineering*, Vol. 8, pp. 537-545, 1974.

[55]   K.Y. Lin, P. Tong and O. Orringer, "Effect of Shape and Size on Hybrid Crack-Containing Elements in Computational Fracture Mechanics," E. Rybicki and S. Benzley, Eds., ASME Special Publication, 1975.

[56]   T.H.H. Pian, P. Tong and C. Luk, "Elastic Crack Analysis by a Finite Element Hybrid Method," in *Proceedings of the Third Air Force Conference on Matrix Methods in Structural Mechanics* (Dayton, Ohio), October, 1971.

[57]   R.D. Henshell and K.G. Shaw, "Crack Tip Finite Elements are Unnecessary," *International Journal for Numerical Methods in Engineering*, Vol. 9, pp. 495-507, 1975.

[58]   R.S. Barsoum, "On The Use of Isoparametric Finite Elements In Linear Fracture Mechanics," *International Journal for Numerical Methods in Engineering*, Vol. 10, pp. 25-37, 1976.

[59]   R.S. Barsoum, "Triangular Quarter-Point Elements as Elastic and Perfectly-Plastic Crack Tip Elements," *International Journal for Numerical Methods in Engineering*, Vol. 11, pp. 85-98, 1977.

[60]   A.R. Ingraffea and C. Manu, " Stress-Intensity Factor Computation in Three Dimensions with Quarter-Point Elements," *International Journal for Numerical Methods in Engineering*, Vol. 15, pp. 1427-1445, 1980.

[61] C. Manu, "Quarter-Point Elements for Curved Crack Fronts," *Computers & Structures*, Vol. 17, No. 2, pp. 227-231, 1983.

[62] W.O. Soboyejo, J.F. Knott, M.J. Walsh and K.R. Cropper, "Fatigue Crack Propagation of Coplanar Semi-Elliptical Cracks in Pure Bending," *Engineering Fracture Mechanics*, Vol. 37, No. 2, pp. 323-340, 1990.

[63] W. Schmitt and H. Kordisch, "Determination of Stresses, Strains, and Crack Characterizing Parameters," in *The Assessment of Cracked Components by Fracture Mechanics*, EGF Publication 4 (Ed: L.H. Larsson), Mechanical Engineering Publications Limited, London, 1989, pp. 27-60.

[64] I.S. Raju and J.C. Newman, "Stress Intensity Factors for Circumferential Surface Cracks in Pipes and Rods under Tension and Bending Loads," in *Fracture Mechanics: Seventeenth Volume, ASTM STP 905*, American Society for Testing and Materials (Philadelphia, USA), 1986, pp. 789-805.

[65] A. Hosseini and M.A. Mahmoud, "Evaluation of Stress Intensity Factor and Fatigue Growth of Surface Cracks in Tension Plates," *Engineering Fracture Mechanics*, Vol. 22, No. 6, pp. 957-974, 1985.

[66] J.C. Newman, Jr. and I.S. Raju, "Stress-Intensity Factor Equations for Cracks in Three-Dimensional Finite Bodies," in *Fracture Mechanics: Fourteenth Symposium - Volume I: Theory and Analysis, ASTM STP 791*, American Society for Testing and Materials, 1983, pp. I-238-I-265.

[67] X. Zheng and M.A. Hirt, "Fatigue Cracks Propagation in Steels," *Engineering Fracture Mechanics*, Vol. 18, No. 5, pp. 965-973, 1983.

[68] J.C. Newman, Jr. and I.S. Raju, "An Empirical Stress-Intensity Factor Equation for the Surface Crack," *Engineering Fracture Mechanics*, Vol. 15, No. 1-2, pp. 185-192, 1981.

[69] J.C. Newman, Jr., "A Review and Assessment of the Stress-Intensity Factors for Surface Cracks," in *Part-Through Crack Fatigue Life Prediction, ASTM STP 687*, American Society for Testing and Materials, 1979, pp. 16-46.

[70] A.J. Fawkes, D.R.J. Owen and A.R. Luxmoore, "An Assessment of Crack Tip Singularity Models for Use with Isoparametric Elements," *Engineering Fracture Mechanics*, Vol. 11, pp. 143-159, 1979.

[71] I.S. Raju and J.C. Newman, Jr., "Stress-Intensity Factors for a Wide Range of Semi-Elliptical Surface Cracks in Finite-Thickness Plates," *Engineering Fracture Mechanics*, Vol. 11, pp. 817-829, 1979.

[72]   **J.C. Newman and I.S. Raju,** "Analysis of Surface Cracks in Finite Plates Under Tension or Bending Loads," NASA Technical Paper, 1978.

[73]   **I.S. Raju and J.C. Newman, Jr.,** NASA TMX-72825, 1977.

[74]   **S.K. Chan, I.S. Tuba and W.K. Wilson,** "On the Finite Element Method in Linear Fracture Mechanics," *Engineering Fracture Mechanics*, Vol. 2, pp. 1-17, 1970.

[75]   **D.R.J. Owen and A.J. Fawes,** *Engineering Fracture Mechanics: Numerical Methods and Applications*, Pineridge Press Ltd., Swansea, U.K., 1983.

[76]   **A.P. Parker,** *The Mechanics of Fracture and Fatigue: An Introduction*, London: E. & F.N. Spon Ltd., 1981.

[77]   **J.R. Rice,** "A Path Independent Integral and the Approximate Analysis of Strain Concentration by Notches and Cracks," *Journal of Applied Mechanics*, Vol. 35, pp. 379, 1968.

[78]   **D. Broek,** *The Practical Use of Fracture Mechanics*, Dordrecht: Kluwer Academic Publishers, 1989.

[79]   **D.M. Parks,** "," *Internation Journal of Fracture*, Vol. 10, pp. 487, 1974.

[80]   **S.J. Maddox,** "Assessing the Significance of Flaws in Welds Subject to Fatigue," *Welding Journal (Research Supplement)*, September, pp. 401-s-409-s, 1974.

[81]   **P.C Paris, M.P. Gomez and W.E. Anderson,** *The Trend in Engineering*, Vol. 13, No. 1, pp. 9-14, 1961.

[82]   **P. Paris and F. Erdogan,** "A Critical Analysis of Crack Propagation Laws," *Journal of Basic Engineering: Transactions of the ASME*, December, pp. 528-534, 1963.

[83]   **J.H. Underwood and W.W. Gerberich,** "Chapter 2: Concepts of Fracture Mechanics," in *Application of Fracture Mechanics for Selection of Metallic Structural Materials* (Eds: J.E. Campbell, W.W. Gerberich and J.H. Underwood), American Society for Metals, Metals Park, Ohio, 1982, pp. 5-21.

[84]   **P.E. Irving and L.N. McCartney,** "Prediction of Fatigue Crack Growth Rates: Theory, Mechanisms, and Experimental Results," *Metal Science*, August/September, pp. 351-361, 1977.

[85]   **S.J. Maddox,** "Recent Advances in the Fatigue Assessment of Weld Imperfections," *Welding Journal*, July, pp. 42-51, 1993.

[86]   **R.G. Forman, V.E. Kearney and R.M. Engle,** *Journal of Basic Engineering: Transactions of the ASME*, Vol. 89, No. 3, pp. 459-464, 1967.

[87] **K. Ohji, S. Kubo, M. Tsuji, H. Ogawa and K. Sakurada**, "Methods of Predicting Fatigue Crack Growth Lives in Residual Stress Fields," *Transactions of the Japan Society of Mechanical Engineers*, Vol. 53, pp. 1516-1523, 1987.

[88] **M. Mohtasham**, "Disc Filter Design Optimization," unpublished Technical Report, 1997.

[89] **W.F. Smith**, *Structure and Properties of Engineering Alloys*, Second Editiion, McGraw-Hill, 1993.

[90] **J. Linder**, "Corrosion Fatigue of Duplex and Austenitic Stainless Steels in 3% NaCl at 80°C and Room Temperature," in *Duplex Stainless Steels: The Welding Institute - Paper 47* (Glasgow, Scotland), November 13-16, 1994, pp. 1-12.

APPENDIX A

NODAL FORCE BOUNDARY CONDITION ALGORITHM

1 Read the data file (sm.dat)

2 Determine the minimum and maximum x-, y- and z-coordinates for face I-a

xmin, xmax, ymin, ymax, zmin, zmax

3 Determine the geometric center of face I-a

$$xcentr = \frac{(xmin + xmax)}{2} \qquad ycentr = \frac{(ymin + ymax)}{2} \qquad zcentr = \frac{(zmin + zmax)}{2}$$

4 Determine the global forces and moments from face I-a that must be generated on face I-b

$$F_x = \sum_{i=1}^{m} \{ fxm(i) \} \qquad F_y = \sum_{i=1}^{m} \{ fym(i) \} \qquad F_z = \sum_{i=1}^{m} \{ fzm(i) \}$$

$$M_x = \sum_{i=1}^{m} \{ mxm(i) + (ym(i) - ycentr) * fzm(i) - (zm(i) - zcentr) * fym(i) \}$$

$$M_y = \sum_{i=1}^{m} \{ mym(i) + (zm(i) - zcentr) * fxm(i) - (xm(i) - xcentr) * fzm(i) \}$$

$$M_z = \sum_{i=1}^{m} \{ mzm(i) + (xm(i) - xcentr) * fym(i) - (ym(i) - ycentr) * fxm(i) \}$$

5 Determine the minimum and maximum x-, y- and z-coordinates for face I-b

xmin, xmax, ymin, ymax, zmin, zmax

6 Determine the geometric center of face I-b

$$xcentr = \frac{(xmin + xmax)}{2} \qquad ycentr = \frac{(ymin + ymax)}{2} \qquad zcentr = \frac{(zmin + zmax)}{2}$$

7 Determine the dimensions of the force determination cubes for face I-b

$$\Delta x = xmax - xcentr \qquad \Delta y = ymax - ycentr \qquad \Delta z = zmax - zcentr$$

8 Determine the diagonals of the force determination cubes for face I-b

$$r\_xy = \sqrt{\Delta x^2 + \Delta y^2} \qquad r\_xz = \sqrt{\Delta x^2 + \Delta z^2} \qquad r\_yz = \sqrt{\Delta y^2 + \Delta z^2}$$

9 Place uniform nodal forces on face I-b which generate the appropriate global forces

$$fxn(i) = \frac{Fx}{n} \qquad fyn(i) = \frac{Fy}{n} \qquad fzn(i) = \frac{Fz}{n}$$

10 Determine the moments generated by the addition of the uniform nodal forces on face I-b

$$TempM_x = \sum_{i=1}^{n} \left\{ (\ yn(i) - ycentr\ ) * fzn(i) - (\ zn(i) - zcentr\ ) * fyn(i) \right\}$$

$$TempM_y = \sum_{i=1}^{n} \left\{ (\ zn(i) - zcentr\ ) * fxn(i) - (\ xn(i) - xcentr\ ) * fzn(i) \right\}$$

$$TempM_z = \sum_{i=1}^{n} \left\{ (\ xn(i) - xcentr\ ) * fyn(i) - (\ yn(i) - ycentr\ ) * fxn(i) \right\}$$

11 Determine the nodal moment arms and the xy-, xz-, and yz-factors on face I-b

$$rxy(i) = \sqrt{(\ xn(i) - xcentr\ )^2 + (\ yn(i) - ycentr\ )^2} \qquad xyfact(i) = \frac{rxy(i)}{r\_xy}$$

$$rxz(i) = \sqrt{(\ xn(i) - xcentr\ )^2 + (\ zn(i) - zcentr\ )^2} \qquad xzfact(i) = \frac{rxz(i)}{r\_xz}$$

$$ryz(i) = \sqrt{(\ yn(i) - ycentr\ )^2 + (\ zn(i) - zcentr\ )^2} \qquad yzfact(i) = \frac{ryz(i)}{r\_yz}$$

12 Determine the sum of the xy-, xz-, and yz-factors for the nodes in each box on face I-b

$$sumaxz = \sum_{i=1}^{n^A} \left\{ xzfact(i) \right\} \qquad \text{where } n^A = \text{the number of nodes in box A}$$

$$sumax = \sum_{i=1}^{n^A} \left\{ xzfact(i) * ABS(\ xn(i) - xcentr) \right\}$$

$$sumaz = \sum_{i=1}^{n^A} \left\{ xzfact(i) * ABS(\ zn(i) - zcentr) \right\}$$

Note: Similarly for boxes B, C, and D.

$$sumexy = \sum_{i=1}^{n^E} \left\{ xyfact(i) \right\} \qquad \text{where } n^E = \text{the number of nodes in box E}$$

$$sumex = \sum_{i=1}^{n^E} \left\{ xyfact(i) * ABS(\ xn(i) - xcentr) \right\}$$

$$sumey = \sum_{i=1}^{n^E} \left\{ xyfact(i) * ABS(\ yn(i) - ycentr) \right\}$$

Note: Similarly for boxes F, G, and H.

$$sumiyz = \sum_{i=1}^{n^I} \{yzfact(i)\} \qquad \text{where } n^I = \text{the number of nodes in box I}$$

$$sumiy = \sum_{i=1}^{n^I} \{yzfact(i) * ABS(yn(i) - ycentr)\}$$

$$sumiz = \sum_{i=1}^{n^I} \{yzfact(i) * ABS(zn(i) - zcentr)\}$$

Note: Similarly for boxes J, K, and L.

13 Determine the moment ratio coefficients for the boxes on face I-b

$Cx1 = sumaz + sumbz + sumcz + sumdz$ $Couplx = Mx - TempMx$

$Cx2 = sumey + sumfy + sumgy + sumhy$

$Cy1 = sumex + sumfx + sumgx + sumhx$ $Couply = My - TempMy$

$Cy2 = sumiz + sumjz + sumkz + sumlz$

$Cz1 = sumiy + sumjy + sumky + sumly$ $Couplz = Mz - TempMz$

$Cz2 = sumax + sumbx + sumcx + sumdx$

14 Use the CSD Algorithm

Unknown Forces: $F(i) = \{F_{1X}, F_{1Y}, F_{1Z}, F_{2X}, F_{2Y}, F_{3Z}, F_{4Y}, F_{5X}, F_{5Z}, F_{7X}, F_{7Y}, F_{7Z}; i = 1,12\}$

Equality Constraints:

Moment Equations

$$h1 = -sumaz * F_{1Y} + sumbz * F_{2Y} + sumcz * F_{7Y} - sumdz * F_{4Y} - \left(\frac{Cx1}{Cx1 + Cx2}\right) * Couplx$$

$$h2 = sumey * F_{1Z} + sumfy * F_{3Z} - sumgy * F_{7Z} - sumhy * F_{5Z} - \left(\frac{Cx2}{Cx1 + Cx2}\right) * Couplx$$

$$h3 = -sumex * F_{1Z} + sumfx * F_{3Z} + sumgx * F_{7Z} - sumhx * F_{5Z} - \left(\frac{Cy1}{Cy1 + Cy2}\right) * Couply$$

$$h4 = sumiz * F_{1X} - sumjz * F_{2X} - sumkz * F_{7X} + sumlz * F_{5X} - \left(\frac{Cy2}{Cy1 + Cy2}\right) * Couply$$

$$h5 = -sumiy * F_{1X} - sumjy * F_{2X} + sumky * F_{7X} + sumly * F_{5X} - \left(\frac{Cz1}{Cz1 + Cz2}\right) * Couplz$$

$$h6 = sumax * F_{1Y} + sumbx * F_{2Y} - sumcx * F_{7Y} - sumdx * F_{4Y} - \left(\frac{Cz2}{Cz1 + Cz2}\right) * Couplz$$

Force Equations

$$h7 = sumiyz * F_{1X} + sumjyz * F_{2X} + sumkyz * F_{7X} + sumlyz * F_{5X}$$

$$h8 = sumaxz * F_{1Y} + sumbxz * F_{2Y} + sumcxz * F_{7Y} + sumdxz * F_{4Y}$$

$$h9 = sumexy * F_{1Z} + sumfxy * F_{3Z} + sumgxy * F_{7Z} + sumhxy * F_{5Z}$$

Additional Terms Required for the Objective Function:

$$sumave = (\ sumaxz + sumbxz + sumcxz + sumdxz$$
$$+ sumexy + sumfxy + sumgxy + sumhxy$$
$$+ sumiyz + sumjyz + sumkyz + sumlyz\ ) / 12$$

$$mave = \frac{ABS(\ Couplx\ ) + ABS(\ Couply\ ) + ABS(\ Couplz\ )}{3}$$

$$term(1) = sumiyz * \frac{ABS(\ Couply\ ) + ABS(\ Couplz\ )}{2 * sumave * mave}$$

$$term(2) = sumaxz * \frac{ABS(\ Couplx\ ) + ABS(\ Couplz\ )}{2 * sumave * mave}$$

$$term(3) = sumexy * \frac{ABS(\ Couplx\ ) + ABS(\ Couply\ )}{2 * sumave * mave}$$

$$term(4) = sumjyz * \frac{ABS(\ Couply\ ) + ABS(\ Couplz\ )}{2 * sumave * mave}$$

$$term(5) = sumbxz * \frac{ABS(\ Couplx\ ) + ABS(\ Couplz\ )}{2 * sumave * mave}$$

$$term(6) = sumfxy * \frac{ABS(\ Couplx\ ) + ABS(\ Couply\ )}{2 * sumave * mave}$$

$$term(7) = sumdxz * \frac{ABS(\ Couplx\ ) + ABS(\ Couplz\ )}{2 * sumave * mave}$$

$$term(8) = sumlyz * \frac{ABS(\ Couply\ ) + ABS(\ Couplz\ )}{2 * sumave * mave}$$

$$term(9) = sumhxy * \frac{ABS(\ Couplx\ ) + ABS(\ Couply\ )}{2 * sumave * mave}$$

$$term(10) = sumkyz * \frac{ABS(\ Couply\ ) + ABS(\ Couplz\ )}{2 * sumave * mave}$$

$$term(11) = sumcxz * \frac{ABS(\ Couplx\ ) + ABS(\ Couplz\ )}{2 * sumave * mave}$$

$$term(12) = sumgxy * \frac{ABS(\ Couplx\ ) + ABS(\ Couply\ )}{2 * sumave * mave}$$

Objective Function:

$$fave = \sum_{i=1}^{12} \left\{ ABS(\ F(i)\ ) \right\}$$

$$f = \sum_{i=1}^{12} \left\{ (\ ABS(\ F(i)\ ) - term(i) * fave\ )^2 \right\}$$

15 Superimpose the forces determined by the CSD Algorithm with the forces on face I-b

If the node is in box   A: $fyn(i) = fyn(i) + xzfact(i) * F_{1Y}$

       B: $fyn(i) = fyn(i) + xzfact(i) * F_{2Y}$

       C: $fyn(i) = fyn(i) + xzfact(i) * F_{4Y}$

       D: $fyn(i) = fyn(i) + xzfact(i) * F_{7Y}$

       E: $fzn(i) = fzn(i) + xyfact(i) * F_{1Z}$

       F: $fzn(i) = fzn(i) + xyfact(i) * F_{3Z}$

       G: $fzn(i) = fzn(i) + xyfact(i) * F_{5Z}$

       H: $fzn(i) = fzn(i) + xyfact(i) * F_{7Z}$

       I: $fxn(i) = fxn(i) + yzfact(i) * F_{1X}$

       J: $fxn(i) = fxn(i) + yzfact(i) * F_{2X}$

       K: $fxn(i) = fxn(i) + yzfact(i) * F_{5X}$

       L: $fxn(i) = fxn(i) + yzfact(i) * F_{7X}$

16 Determine the global forces and moments generated on the face I-b nodes

$$TempF_x = \sum_{i=1}^{n} \{ fxn(i) \} \quad TempF_y = \sum_{i=1}^{n} \{ fyn(i) \} \quad TempF_z = \sum_{i=1}^{n} \{ fzn(i) \}$$

$$TempM_x = \sum_{i=1}^{n} \{ (yn(i) - ycentr) * fzn(i) - (zn(i) - zcentr) * fyn(i) \}$$

$$TempM_y = \sum_{i=1}^{n} \{ (zn(i) - zcentr) * fxn(i) - (xn(i) - xcentr) * fzn(i) \}$$

$$TempM_z = \sum_{i=1}^{n} \{ (xn(i) - xcentr) * fyn(i) - (yn(i) - ycentr) * fxn(i) \}$$

17 Determine the global force and moment residuals

$ResFx = ABS(Fx - TempFx)$

$ResFy = ABS(Fy - TempFy)$

$ResFz = ABS(Fz - TempFz)$

$ResMx = ABS(Mx - TempMx)$

$ResMy = ABS(My - TempMy)$

$ResMz = ABS(Mz - TempMz)$

18 Write the nodal force values to the output file (sm.out) in session file format